Preliminary Report on Geotechnical Aspects of the May 15th 2020 Magnitude 6.5 Monte Cristo Range Earthquake in Nevada

A report of the NSF-Sponsored Geotechnical Extreme Event Reconnaissance Association

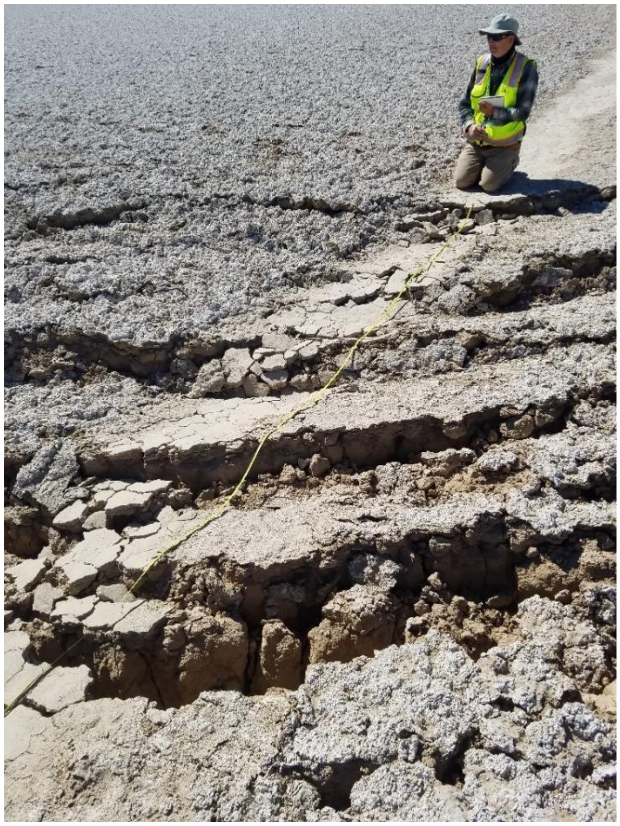

GEER Team Members

Ramin Motamed: University of Nevada, Reno
Marc Ryan: Slate Geotechnical Consultants, Inc.
Gregory Lambeth: Wood
Joseph Toth: Wood
Maggie Parks: ENGEO
F. Estéfan T. Garcia: University of Michigan, Ann Arbor
Patrick C. Bassal: University of California, Davis
Jonathan Pease: Reno Tahoe Geo Associates

Contributing Author

Richard Koehler: University of Nevada, Reno and Nevada Bureau of Mine and Geology

GEER Team Leader and Report Editor: Ramin Motamed (University of Nevada, Reno)
Team Co-Lead: Marc Ryan (Slate Geotechnical Consultants, Inc.)

Report GEER-71: https://doi:10.18118/G67H4F
March 10, 2021 (version 1)

Acknowledgments

The work of the GEER Association is based in part on work supported by the National Science Foundation through the Engineering for Civil Infrastructure Program under Grant No. CMMI-1826118. Any opinions, findings, and conclusions or recommendations expressed in this material are those of the authors and do not necessarily reflect the views of the NSF. The authors would like to acknowledge several individuals who supported the reconnaissance team by providing information including:

- Michael Taylor and Tonya Santos (NDOT) who provided initial information about the infrastructure in the affected area and access to US 95 during repair work
- Richard Koehler and Conni De Masi (UNR) for several discussions on the initial findings of the UNR/NBMG reconnaissance team, aerial photos, and a review of the report.
- John Anderson and John Louie (UNR) for sharing useful information about the recorded ground motions and the recording stations.
- Erol Kalkan (QuakeLogic) for providing access to the instrumented Galena Creek bridge data
- Nima Mojtahedzadeh (UNR) for running laboratory tests on soil samples.

Insights provided by Jonathan Stewart (UCLA) who was the GEER liaison for this reconnaissance are acknowledged.

Contents

List of Figures

List of Tables

1.0 Introduction

The moment magnitude (M_W) 6.5 Monte Cristo Range earthquake occurred 56 km west of Tonopah, Nevada on May 15th, 2020, at about 4AM PDT. The Monte Cristo Range, where the earthquake epicenter was situated, is located in western Nevada and lies along the east of Highway US 95, an important highway connecting northern and southern Nevada. The earthquake epicenter was located in the Walker Lane, a seismically active zone along the California-Nevada border. The reported faulting mechanism was strike-slip in shallow crust.

This report summarizes the preliminary findings by the NSF-sponsored Geotechnical Extreme Events Reconnaissance (GEER) team which visited the Monte Cristo Range area. The GEER team was mobilized to the epicentral region 3 weeks after the main event, and the area of interest was decided based on findings by other advance teams from United States Geological Survey (USGS), Nevada Bureau of Mines and Geology and the University of Nevada – Reno (NBMG/UNR) and California Geological Survey (CGS) which had pointed out some interesting ground failure patterns in the Columbus Marsh area west of US 95.

The report first reviews the geological setting of the Monte Cristo Range area including a discussion on the fault rupture mechanism and the observed surface evidence. Then, it discusses the seismological features of the event. The GEER team spent two days in the field collecting and documenting the observed ground failure patterns, mainly caused by widespread liquefaction-induced lateral spreads and associated settlements as well as surface manifestations (sand ejecta) in the area. These observations are presented in detail in this report.

The main shock was recorded by over 222 strong motion recording stations, belonging to 9 different networks some of which are discussed and presented in the report. Select ground motions of nearby stations were processed and their key characteristics are included in this report in Appendix A. The report further documents one of the observed rockfalls in the epicenter area.

The field and laboratory tests that were conducted are described next. The in-situ tests consisted of Refraction Microtremor (ReMi) measurements which provided shear wave velocity profiles in the upper 100ft of the subsurface soil. The ReMi results were used to perform site classification as well as an assessment of the spatial variability of the subsurface soil profiles. In addition, several soil samples were taken in the observed ground failure area and tested in the laboratory for basic index properties and soil classifications. The laboratory test results are summarized in the report and the details are presented in Appendix B.

The report provides an assessment of the transportation systems in the area such as highway US 95 and culverts located in the inspected area. The GEER team also conducted a high-level evaluation of industrial facilities located in the area including some mining sites. The report concludes with presenting a preliminary assessment of liquefaction triggering based on the shear wave velocity profiles and the index soil testing results.

2.0 Geology

The Monte Cristo Range Earthquake occurred within the Walker Lane, a north-northwest trending zone of deformation and seismicity along the western margin of the Basin and Range Physiographic Province. The Basin and Range Physiographic Province acts as a transitional zone between the dextral strike-slip motion of the San Andreas Fault system and the extensional Basin and Range province. It is estimated that up to one-fourth of the approximately 50 millimeters per year of strike-slip motion between the Pacific and North American plates is taken up along faults east of the San Andreas fault system within the eastern California Shear Zone and Walker Lane (Wesnousky, 2005). The earthquake occurred in the Mina Deflection, a structural right-step in the Walker Lane comprised of a series of east-west striking left-lateral strike-slip faults that connect sets of northwest-striking right-lateral faults to the northeast and southwest (NBMG, 2020). As with the majority of Nevada and the Basin and Range, the physiography of the region where the Monte Cristo Range Earthquake occurred is comprised of fault bounded mountain ranges and intervening closed basins which are products of late Cenozoic trans-tensional and extensional tectonics.

Rocks exposed in the mountain ranges in the region surrounding the Monte Cristo Range Earthquake include sedimentary, igneous, and metamorphic rocks ranging in age from late Precambrian to Quaternary (Figure 2-1). Pre-Tertiary marine sedimentary, intrusive and volcanic rocks are commonly cut by low angle (less than 45-degree dip) thrust faults (Alpers and Stewart, 1972), and the distribution and structure of the pre-Tertiary rocks in the region is largely attributed to the displacement of four Paleozoic and Mesozoic thrust sheets including; the Roberts Mountains allochthon, the Golconda allochthon, the Luning allochthon, and the Palmico allochthon (Moeller, 1986). Tertiary rocks unconformably overlie the pre-Tertiary and are mainly comprised of andesitic and rhyolitic volcanics. Pliocene to Pleistocene basalt flows are also common in the region. The Monte Cristo Range, where the earthquake occurred, is mainly comprised of Tertiary andesitic and rhyolitic rocks and Pliocene to Pleistocene basalt flows.

The basins between mountain ranges are underlain by several thousand feet of Tertiary to Quaternary sedimentary and volcanic fill. The Columbus Salt Marsh, located southeast of the epicenter, is a closed topographic basin that covers an area of approximately 370 square miles. Deposits in the Columbus Salt Marsh are predominantly Tertiary lacustrine and basin fill sediments. The basin has been the site of intermittent mineral resource exploration and small scale production dating as far back as the 1860's including, borax production, extraction of potash rich brines, and more recently, geothermal and lithium exploration (Westwater Resources, 2020).

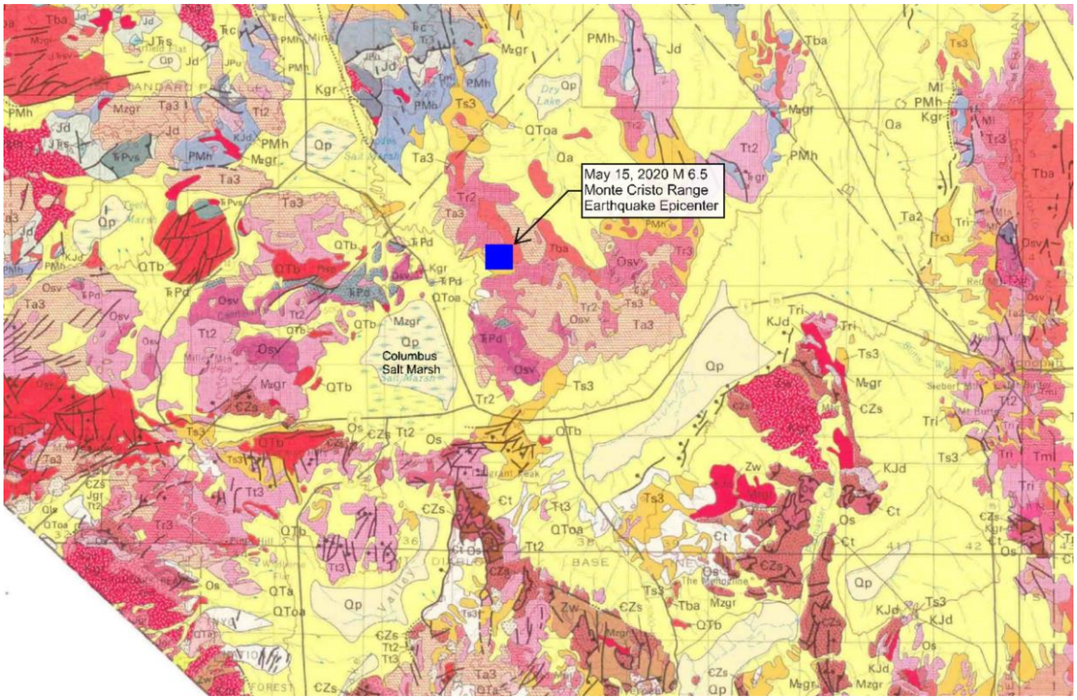

Figure 2-1: Geologic map showing approximate location of epicenter (Stewart and Carlson, 1978).

Figure 2-2: Location of wells drilled in the vicinity of the Columbus Salt Marsh (NDWR, 2020).

The first mineral discoveries in the region date back to the 1850's, and commercial mining of metals such as silver, gold, copper, antimony, iron, lead, mercury, tungsten, and zinc has been conducted since as early as the 1860's. Nonmetallic minerals such as alum, sulfur, barite, borates, and diatomite have also been mined in the region (Alpers and Stewart, 1972). Coaldale Junction takes its name from a group of low-tonnage coal mines south of the Columbus Salt Marsh. Lithium is also extracted from brines pumped from the basin fill aquifers in Clayton Valley approximately 30 miles south of the epicenter. Geothermal activity has also been identified in the area, and multiple geothermal exploration boreholes have been drilled (Oldow, et. al, 2016).

As shown in Figure 2-2, the Nevada Division of Water Resources database contains records for multiple wells which have been drilled in the vicinity of the Columbus Salt Marsh. Table 2-1 contains some of the details for the wells shown in Figure 2-2.

Table 2-1: Details for wells shown in Figure 2 (NDWR, 2020)

Location No.	**Well Completion Date**	**Drilled Depth (ft)**	**Static Water Level (ft)**
1	12/3/2001	50	6
2	2/12/1951	85	8
3	8/9/1958	103	40
4	NR *	187	43.5
5	10/13/1981	76	48
6	11/7/1981	110	65
7	NR *	246	80
8	11/11/1963	292	110
9	5/5/1980	920	310
10	8/5/1978	1000	350
11	3/21/2012	796	375

* NR – Not Recorded

2.1 Surface Fault Rupture

The surface fault rupture reconnaissance began on the day of the earthquake and was a multi-agency effort coordinated by the NBMG with assistance from scientists from the USGS, CGS, and several university and industry representatives. Photographs of fractures extending across US 95 that were circulated on social media the morning of the event provided the first possible evidence of surface rupture. These features were later determined to be related to settlement of lacustrine sediments (not surface rupture) but provided a general meeting location for science teams as the search for surface rupture began. Initial reconnaissance efforts focused on the epicentral area east of US 95. In the subsequent days, individual teams expanded the search to areas west and northwest of US 95, partially guided by InSAR interferogram data provided by the USGS in near real time. The initial reconnaissance effort was conducted over approximately one week. The locations of surface ruptures and fractures were marked by GPS and observations on the style, orientation, and patterns of ruptures and amount of displacement were recorded. Several short follow up investigations to record additional field observations and collect aerial drone imagery were conducted in the zones with the most continuous surface ruptures with measurable offset. The surface rupture observations are currently being compiled by NBMG including additional mapping based on the aerial drone imagery and an Open-File map is anticipated to be released in the fall of 2020. Data supplements associated with this map will provide details on the fault rupture parameters, including individual measured displacements. Initial observations obtained during the reconnaissance are summarized below.

Distributed surface ruptures were observed across a 24 km generally east-northeast trending zone, predominantly west of the epicenter. Two distinct zones of surface rupture in terms of style and orientation of displacements were observed, roughly separated by US 95, and herein referred to as the eastern and western rupture zones. Within the eastern rupture zone, four distinct zones of generally north trending ruptures that exhibit predominantly extensional deformation were observed. Approximately 700 m east of US 95 (lat. 38.14867°, long. -117.93757°), a 30-40 m wide zone of sinuous overlapping ruptures extends 015° for about 1.5 km across relatively young alluvial fans and active washes (Figure 2-3A). There, individual ruptures are 20-45 m long and characterized by left and right steps, open fractures (0.5-3 cm), and occasional vertical separations of 2-3 cm. A similar set of ruptures occurs about 1 mile farther east (lat. 38.15897°, long. -117.91976°), has a N-S orientation, and is continuous for about a kilometer. Immediately west of the Monte Cristo Range, about 6 km east of HWY 95 (lat. 38.15732°, long. -117.88081°), a 600 m wide zone of parallel ruptures ranging in orientation from 355° to 30° extends across a relatively old alluvial fan surface with moderately- to well-developed desert pavement. Fractures in this area are typically open 1-2 cm. Finally, the easternmost observed rupture occurred within the Monte Cristo Range, approximately 12 km east of HWY 95 (lat. 38.16566°, long. -117.80527°). In this area, a 40 m wide zone of sinuous, anastomosing, extensional fractures (open 1-2 cm, occasionally up on the east 3 cm) extends for about 2 km and coincides with a fault mapped in bedrock (Figure 2-3B).

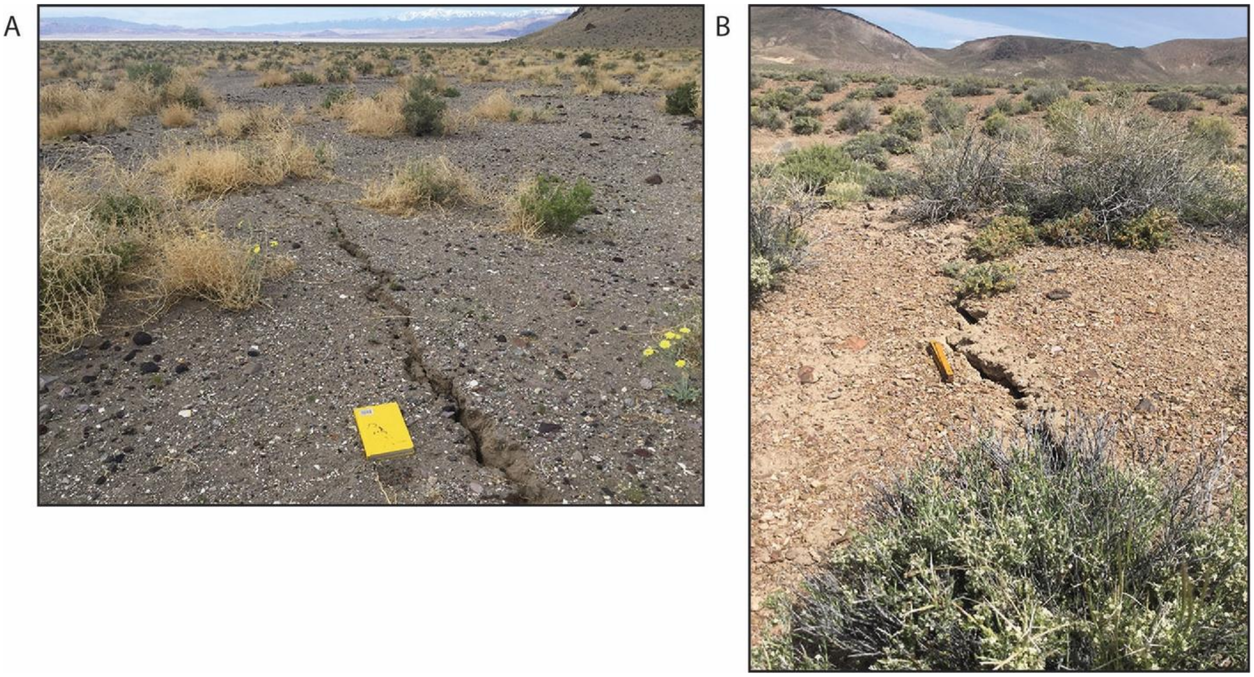

Figure 2-3: Photographs of surface rupture in the eastern surface rupture zone. (A) lat. 38.15229°, long. -117.93675°. (B) lat. 38.16693°, long. -117.80469°.

The western rupture zone extends east-northeast from the eastern end of the mapped trace of the Candaleria fault in the Candaleria Hills to US 95 for a total distance of about 10 km. There, ruptures extend across low bedrock hills, pediments, alluvial fans, and active washes. The zone is characterized by two subparallel main traces striking 050°-070° that exhibit a sinuous pattern in map view. Ruptures along these traces have right stepping en echelon surface breaks connected by small push up mounds and moletracks (Figure 2-4A), a text-book geomorphic expression of left lateral displacement analogous to the 2019 M6.4 Ridgecrest California earthquake. Left lateral displacements along these traces range from 5-15 cm, and possibly up to 20 cm, however subtle piercing points associated with wash margins precluded accurate measurement of displacement in many locations (Figure 2-4B). North-northeast striking ruptures (005°-020°) extend for lengths of 0.5 to 1 km, splay off both of the main northeast striking traces, and exhibit a right stepping pattern. Displacements along these traces are predominantly centimeter scale extensional separations with local vertical separations up to 7 cm. The majority of the ruptures in the western rupture zone are associated with broad zones of distributed extensional fracturing up to 500 m wide with 1-3 cm open surface cracks along individual fractures.

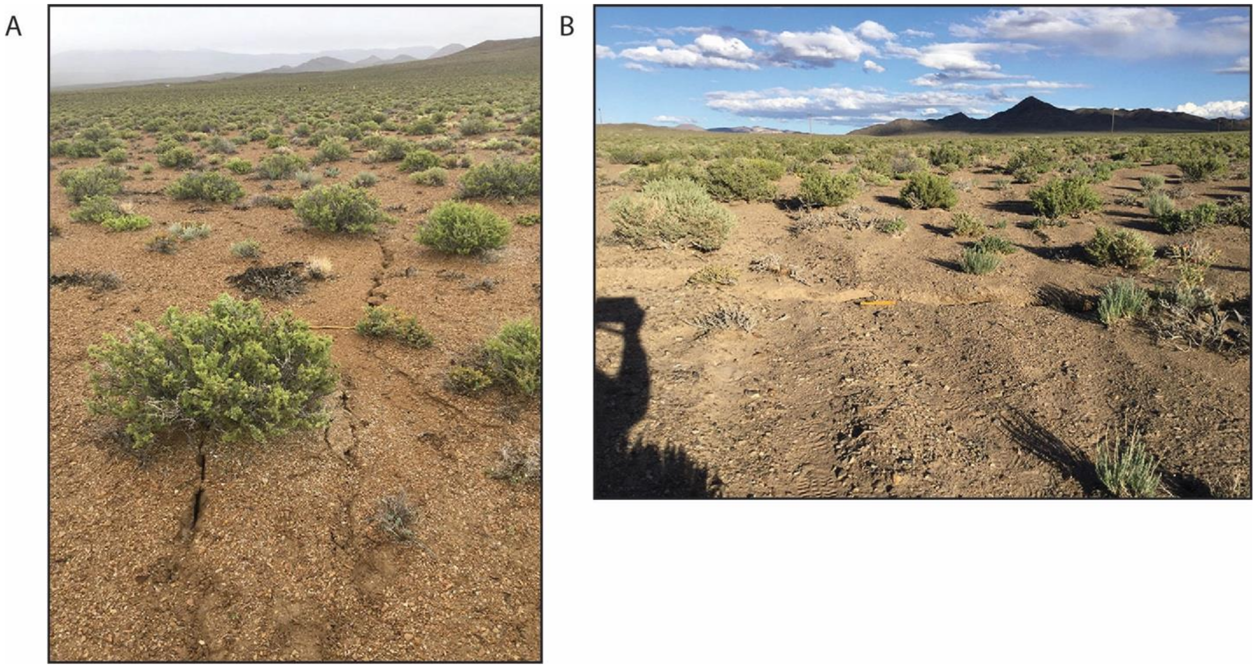

Figure 2-4: Photographs of surface rupture in the western surface rupture zone. (A) lat. 38.17316°, long. -118.02345°. (B) lat. 38.18315°, long. -118.00648°.

3.0 Seismological Aspects

The Monte Cristo Range Earthquake occurred on May 15, 2020 at 4:03AM (PDT). The event produced a magnitude **M**6.5 earthquake centered approximately 56 miles west of Tonopah, Nevada and 125 miles southeast of Carson City, Nevada (NBMG, 2020). The earthquake (epicenter location presented below in Figure 3-1) occurred in a seismically active zone known as the Walker Lane seismic belt as a result of left lateral strike-slip displacement along a steeply dipping, east-northeast striking fault plane at a depth of 2.7 kilometers (USGS, 2020). As reported in NBMG (2020), the following characteristics were noted:

- The earthquake occurred in an area known as the Mina Deflection, a series of east-west striking left-lateral strike-slip faults that act to connect sets of northwest-striking right-lateral faults to the northeast and southwest.
- The seismicity indicates that the rupture occurred on an east-west striking plane with a left-lateral sense of motion.
- The rupture extends across the Monte Cristo Range and is generally spatially coincident with faults previously mapped in bedrock and along strike of the projection of the Quaternary-active Candelaria fault.

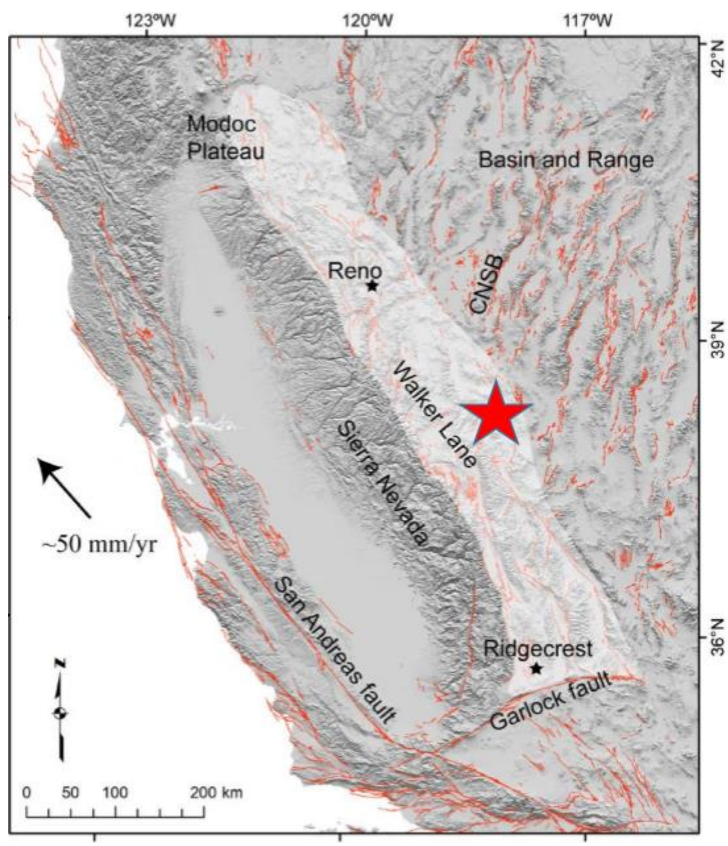

Figure 3-1: Location of Epicenter within the Walker Lane Seismic Belt (Koehler, 2020).

Two weeks after the May 15th event, as many as 6,500 aftershocks were recorded within the vicinity of the epicenter (UNR, 2020). As of June 6, 2020 there had been 321 aftershock events of magnitude 3 or higher and 3 events of magnitude 5 or higher (USGS, 2020). The trend of the earthquake sequence is coincident with the eastward projection of the Candelaria Fault toward the southern projection of the Bettles Well-Petrified Springs Fault. Figure 3-2 presents the locations of recorded seismic events for May 15th, 2020 in relation to Quaternary fault traces and the moment tensor for the M 6.5 Monte Cristo Range Earthquake.

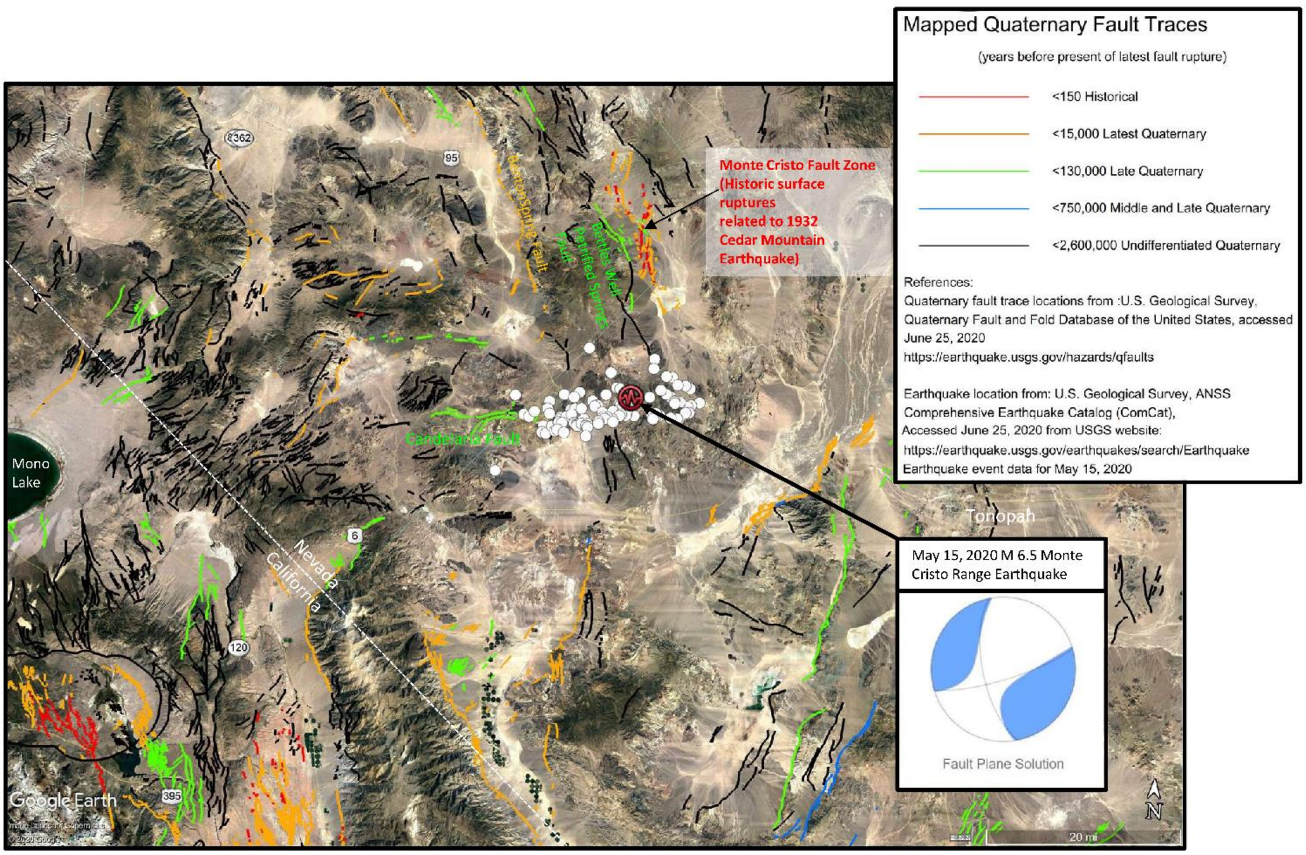

Figure 3-2: Map of location and moment tensor of May 15th, 2020 M 6.5 Monte Cristo Range Earthquake, also showing recorded earthquake events which occurred on May 15, 2020, and mapped Quaternary fault traces (USGS, 2020b, 2020c).

The Monte Cristo Range Earthquake sequence and the Mina Deflection are located in an area between two zones with significant historic seismicity, the Central Nevada Seismic Belt and the Southern Walker Lane. The largest recorded earthquakes in Nevada have occurred in the Central Nevada Seismic Belt, including; the 1915 (M 7.3) Pleasant Valley earthquake, the 1932 Cedar Mountain earthquake (M 7.1), the 1954 Rainbow Mountain-Stillwater sequence (M 6.1, M 6.2, M 6.8), and the 1954 Fairview Peak (M 7.1) and Dixie Valley (M 6.8) earthquakes (dePolo, 2014). The 1872 (estimated M 7.9) Owens Valley Earthquake, the 1980 Mammoth Lakes earthquake sequence, the 1986 (M 6.4) Chalfant Valley earthquake, and the 2019 (M 7.1) Ridgecrest earthquake occurred south and southwest of the Monte Cristo Range Earthquake in the Central and Southern Walker Lane. The Monte Cristo Range Earthquake sequence is shown in Figure 3-3 with the dates and locations of historic surface ruptures in the Central Nevada Seismic Belt and the Southern Walker Lane, along with seismicity associated with another recent earthquake event sequence which occurred on April 11, 2020 near Mono Lake, California.

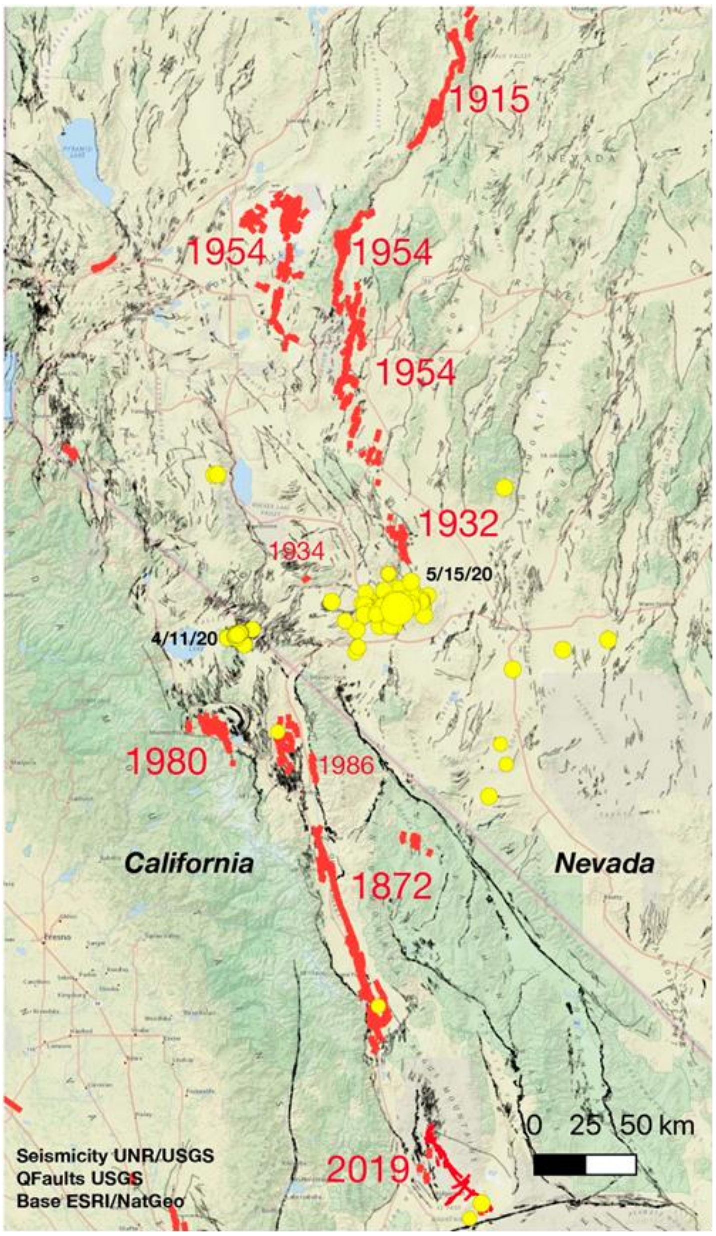

Figure 3-3: Location of May 15th, 2020 M 6.5 event with aftershocks (in yellow), dates and locations of historic surface ruptures (in red) in the southern Walker Lane and the Central Nevada Seismic Belt, and mapped faults with evidence of Quaternary offset in the region (in gray and black) (photo courtesy of @rangefront on Twitter).

3.1 Earthquake Intensity Observations (MMI)

Following the May 15th event, as many as 22,000 records of shaking were reported on the USGS website from locations as far away as San Francisco, California and Salt Lake City, Utah. A map of the reported shaking felt as a result of the event is presented below in Figure 3-4 (USGS, 2020). Reported Modified Mercalli Intensities (MMIs) within 50 kilometers of the site ranged from level III (light) to level VII (very strong).

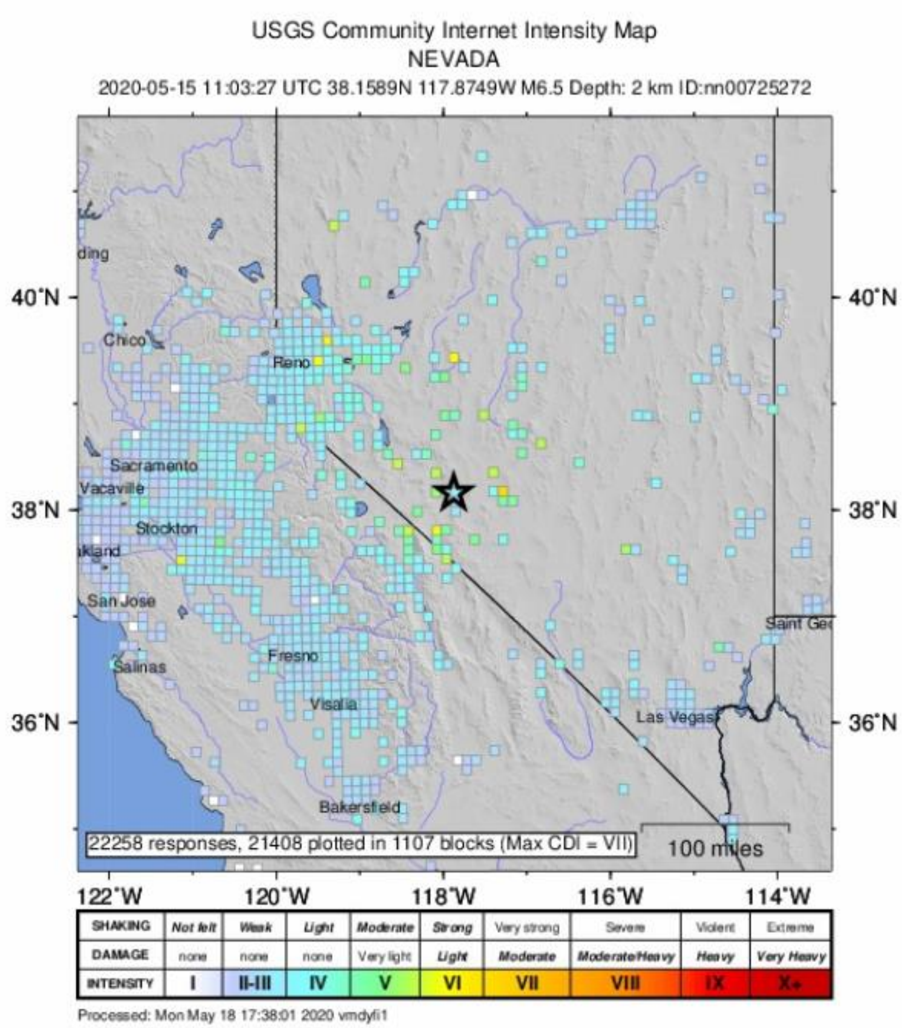

Figure 3-4: Distribution of Shaking Reports as of May 18, 2020 (USGS, 2020).

The Modified Mercalli Intensity of the region as modeled by the USGS using the ShakeMap (Worden, et. Al., 2020) computer program is presented in Figure 3-5.

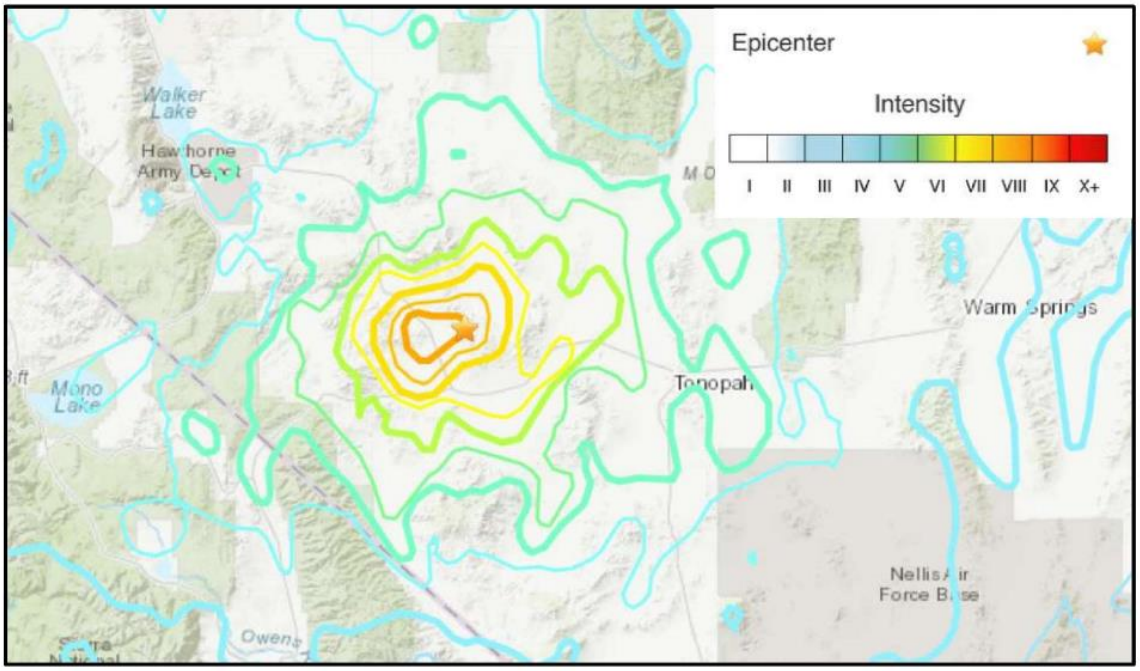

Figure 3-5: MMI modeled using ShakeMap Version 4.0 (Worden, et. al., 2020)

3.2 Seismograph Data and Projections of Ground Motions

Seismograph station coverage in Nevada is sparse and seismographs in the subject study area included by the CESMD and IRIS data sets for this event are primarily concentrated in California. For example, the data available through the Center for Engineering Strong Motion Data (CESMD) data set for the May 15th, 2020 event includes stations mainly concentrated in California. Within the CESMD seismograph network, a maximum peak horizontal ground acceleration (PGA) of 0.051 g was recorded 119 km from the Monte Cristo Range Earthquake epicenter. The locations of the seismographs and approximate measured PGAs for the May 15, 2020 Monte Cristo Range Earthquake are shown on Figure 3-6.

Section 5 provides additional discussions on the recorded ground motions by different seismic networks and some example acceleration time histories are presented.

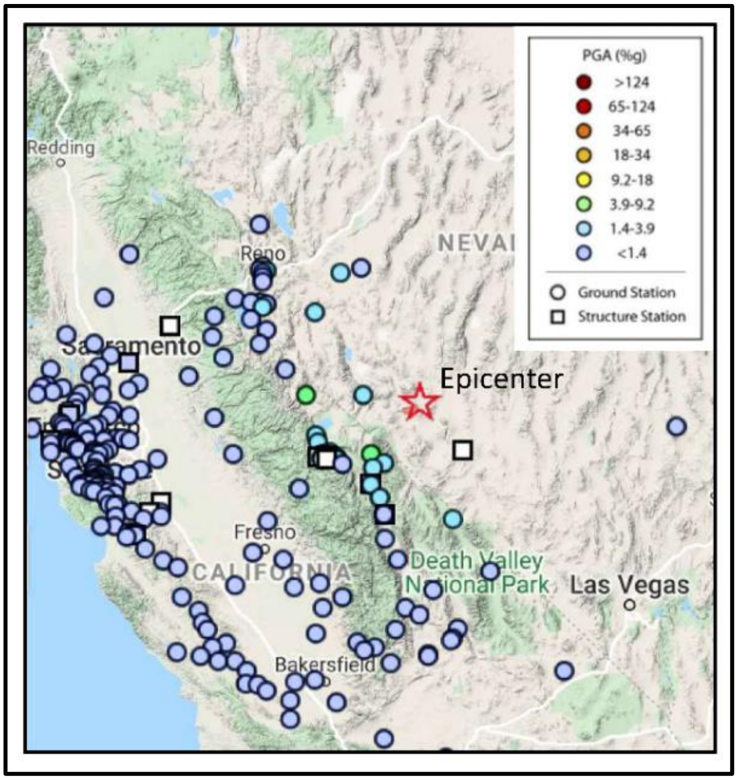

Figure 3-6: Seismographs included in the CESMD network showing approximate PGA recorded at each station for the May 15, 2020 Monte Cristo Range earthquake (CESMD, 2020).

4.0 Ground Surface Displacements

The GEER team was notified of and performed concentrated studies of surface cracking and other ground displacement features in the Columbus Salt Marsh region west of US95 on the dates of June 8-9, 2020. A concentrated region of ground displacements assumed to be liquefaction-induced lateral spread and ground oscillation was encountered on the east side of Columbus Salt Marsh approximately 9 km south of the earthquake epicenter. There is evidence throughout the Columbus Salt Marsh, including the areas of ground failure, of past mineral harvesting or prospecting, including furrows or vehicle tracks on the surface, shallow wells or pipe markers, and an abandoned evaporation facility 300 m south of the ground failure sites.

4.1 Lateral Spread Feature

Previous reconnaissance efforts involving field and remote observations organized by the USGS took place prior to the GEER Reconnaissance (Elliot et al. 2020). The initial findings from the preliminary report produced by this effort include 25 new surface deformations mapped with high confidence and 12 surface discontinuities mapped with lower confidence located north and northeast of the Columbus Salt Marsh. Field observations described in the preliminary report (Elliot et al. 2020) confirm many of the discontinuity features and show additional discontinuities.

A single region of lateral spread was identified on an alluvial fan about 300 m from the playa boundary and 3 km downhill from the rangefront of the Monte Cristo Range. The deformation features appear to be the extensional uphill edge of a lateral spread and extended approximately 300 m in length from north to south with a noticeable curvature of about 80 m uphill to the east in the middle of the feature. These surface traces intersected US95 and required approximately 2 weeks of road repairs by NDOT. The repair efforts were on-going during the GEER reconnaissance, and the roadway damage across US95 was already covered on June 8. While rainfall occurred the day prior to the GEER reconnaissance, there was clear evidence of surface shear and extension cracking on both sides of the highway. It is possible that rainfall during the day prior to the GEER reconnaissance likely covered some surface deformation features in the Columbus Salt Marsh, but this is unlikely due to the extent that sandy features around US 95 were generally apparent.

The location of the surface deformation trace of the lateral spread feature relative to previously mapped surface fault rupture traces is shown in Figure 4-1. Continuation of this feature was mapped by Conni De Masi Castillo via drone imagery (and also observed by the team members) as shown on Figure 4-2. The photos captured by Castillo suggest that the feature is possibly a surface deformation feature related to liquefaction (Figures 4-3 and 4-4). Figure 4-5 shows some of these distributed cracking features along the surface deformation trace. Some of the distributed cracks bound grabens with widths of approximately 23cm as shown in Figure 4-6 and vertical offsets of approximately 4cm. The ground surface elevation gradient on the apparent liquefaction feature was less than 1%. No compression features were noted to the west of this feature which might indicate the downhill end of the lateral spread. Surface materials in this area were generally coarse to fine, poorly-graded sand with silt to silty sand (with less than about 20% fines). Widespread sand boils were observed in this area which will be discussed in detail in Section 4.2.

The identification of a lateral spread associated with liquefaction would be suggested by a) the arcuate and wider-spaced zones of deformation, b) the likely shallowing of the groundwater table approaching the playa margin, c) reduction in the fan gradient in this region, resulting in lower-energy deposition, hence more uniform fine sands and lower relative density, and d) possible interfingering with silt layers marginal to the playa which would tend to confine and maintain elevated pore pressures (R. Koehler pers. comm.). The area of ground deformation is approximately downhill from the distal end of a desert wash (Figure 4-1) which may have delivered heavier sediment load, which on average would have younger deposition, than other portions of the alluvial fan.

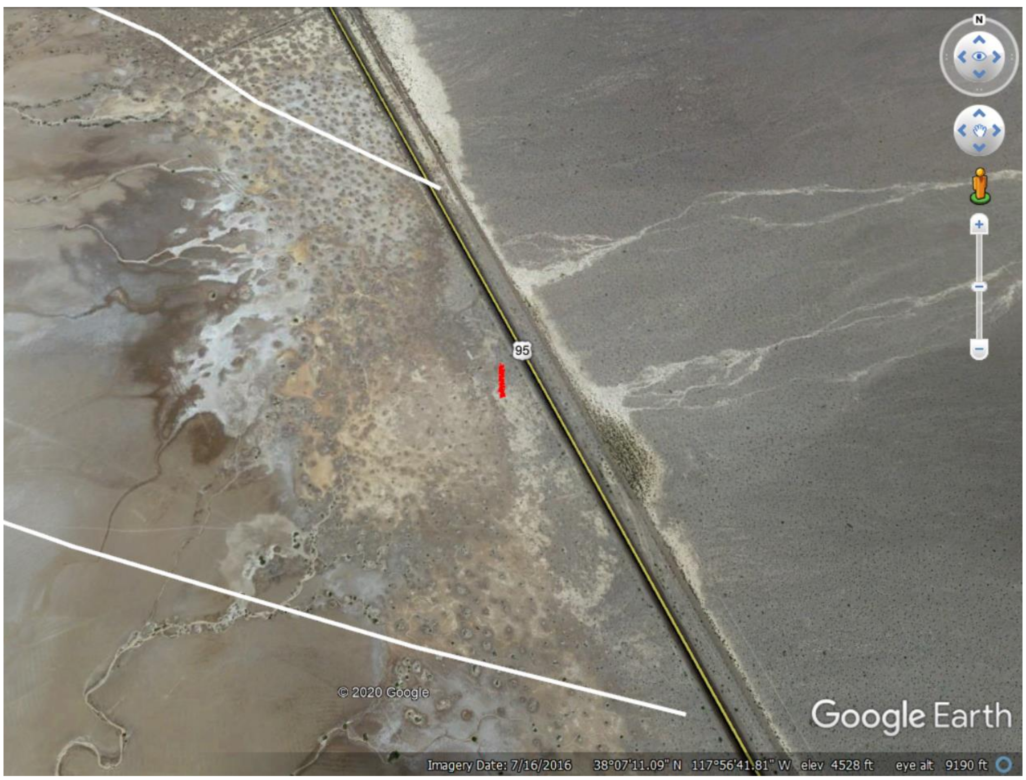

Figure 4-1: Surface deformation feature mapped by the GEER team (red) and surface fault rupture traces mapped by USGS (white; Elliot et al. 2020).

Figure 4-2: Surface deformation feature mapped by the GEER team (red) and locations of drone photos showing liquefaction deformation features (Google Earth).

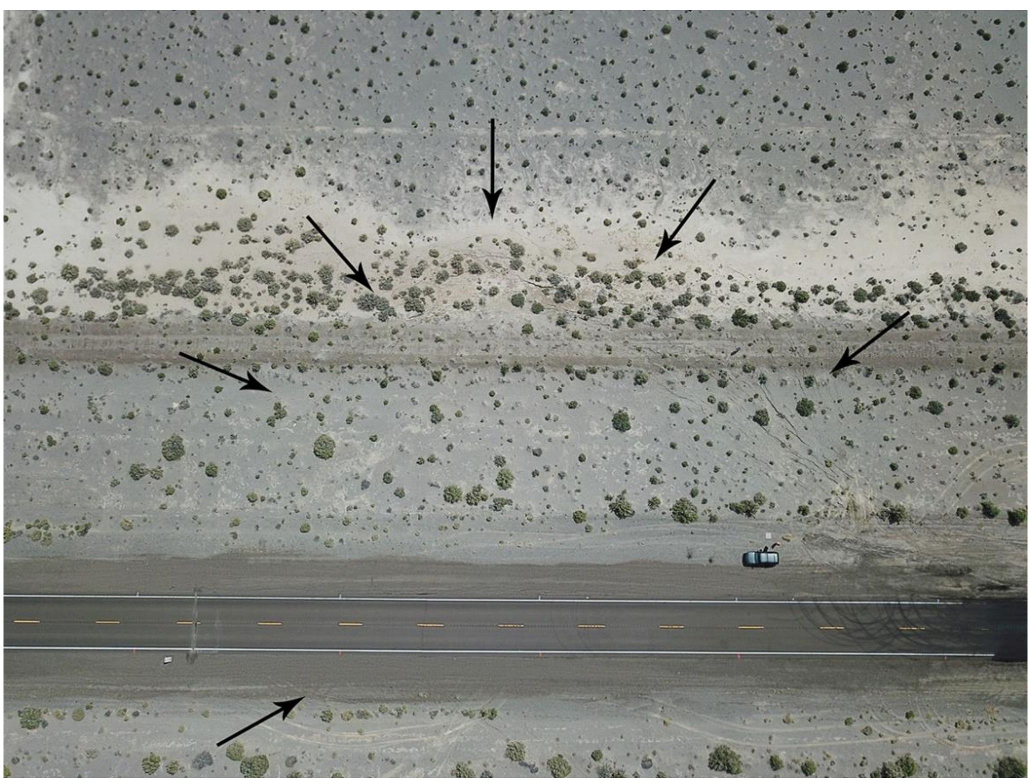

Figure 4-3: Drone image A of surface deformation adjacent to Highway 95 (38 6' 41.6077" N, 117 55' 43.4268" W, altitude 1572.76 m; photo courtesy of Conni De Masi Castillo, UNR).

Figure 4-4: Drone image B of surface deformation adjacent to Highway 95 (38 6' 41.6077" N, 117 55' 43.4268" W, altitude 1572.76 m; photo courtesy of Conni De Masi Castillo, UNR).

Figure 4-5: Distributed cracking features associated with the surface deformation trace shown in Figure 4-1 (*lat/lon = 38.11093611, -116.07064167*).

Figure 4-6: 23cm wide graben associated with the surface deformation trace (*lat/lon = 38.11118056, -116.07064722*).

4.2 Sand Boils

The GEER team documented areas of small fine-grained sand boils consisting of silt ejecta (Figure 4-7) in the borderline playa area about 200 m west of the lateral spread surface cracking and 100 m east of one of the ground oscillation features. The sand boil features were indistinct, but observable due to probable ejecta material that contrasted with the dominant surficial soils (Figure 4-8). The probable ejecta was much lighter in color than other surficial soils and appeared to be a very fine-grained silt, with low plasticity (Figure 4-9). The GEER team collected some of the ejecta material and performed laboratory testing on its index properties (see Section 7).

Figure 4-7: Location of sand boil features in comparison to other surface deformation features discussed (*Google Earth*).

Figure 4-8: Area of observed sand boils, ejecta is lighter colored material (*lat/lon = 38.1120, -116.067*).

Figure 4-9: Sand boils showing light colored ejecta (*lat/lon = 38. 1121, -116. 067*).

4.3 Ground Surface Settlements and Oscillation Features

The GEER team documented 6 enclosed ground subsidence features in the Columbus Salt Marsh generally lying west of the playa boundary in an approximate N-S direction (Fig 4-10). Figure 4-11 shows an aerial view of the southernmost of these subsidence features. These features are considered to result from ground oscillation, initially defined by Youd and Keefer (1994) as sloshing of surface deposits on a weak (usually liquefied) layer without any significant permanent lateral deformation. There is commonly extensional crack on one or more sides, and there may be minor ground subsidence due to either differential offset of the slide flake at the end of shaking, or post-liquefaction consolidation. From a kinematics standpoint, it is possible that these features do not result from excess shaking at all, but rather the surface materials detaching from the underlying ground motions and remaining stationary while the ground movement occurs outside, however Pease and O'Rourke (1997) suggest that at the correct driving frequency, these deposits may develop longer-period oscillatory motion at a natural period roughly independent from the underlying ground motions. Because of the apparent loose (dessication-cracked) nature of the playa surface, all of the observed features are extensional or shear cracks. Features GSS1, GSS2, and GSS5 were measured more closely by the GEER team and are shown in Figures 4-12 to 4-16. Based on Google Earth, the ground surface at these features was essentially flat with insignificant regional slope.

Subsidence feature GSS1 is approximately circular with N-S and E-W widths of approximately 34m. It appears in relatively flat terrain. Table 4-1 lists the observations associated with each waypoint of subsidence feature GSS1, and Figures 4-17 through 4-37 show the accompanying photographs. The blocks described in Table 4-1 are intact soil bounded by cracks, and the gaps described in Table 4-1 are open fissures in the soil in between the blocks. The subsurface conditions of this feature are analyzed using ReMi surveys as discussed in Chapter 10.

Feature GSS2 is a kidney-bean shaped subsidence feature with a concave portion on each of its E-W sides. The distance between Waypoint 1 and Waypoint 5 of GSS2 is 108.5m. Table 4-2 lists the observations associated with each waypoint, and Figures 4-38 through 4-50 show the associated photographs. As shown in Figure 4-39, the ground surface displacements associated with GSS2 cross an ephemeral stream channel within the Columbus Salt Marsh.

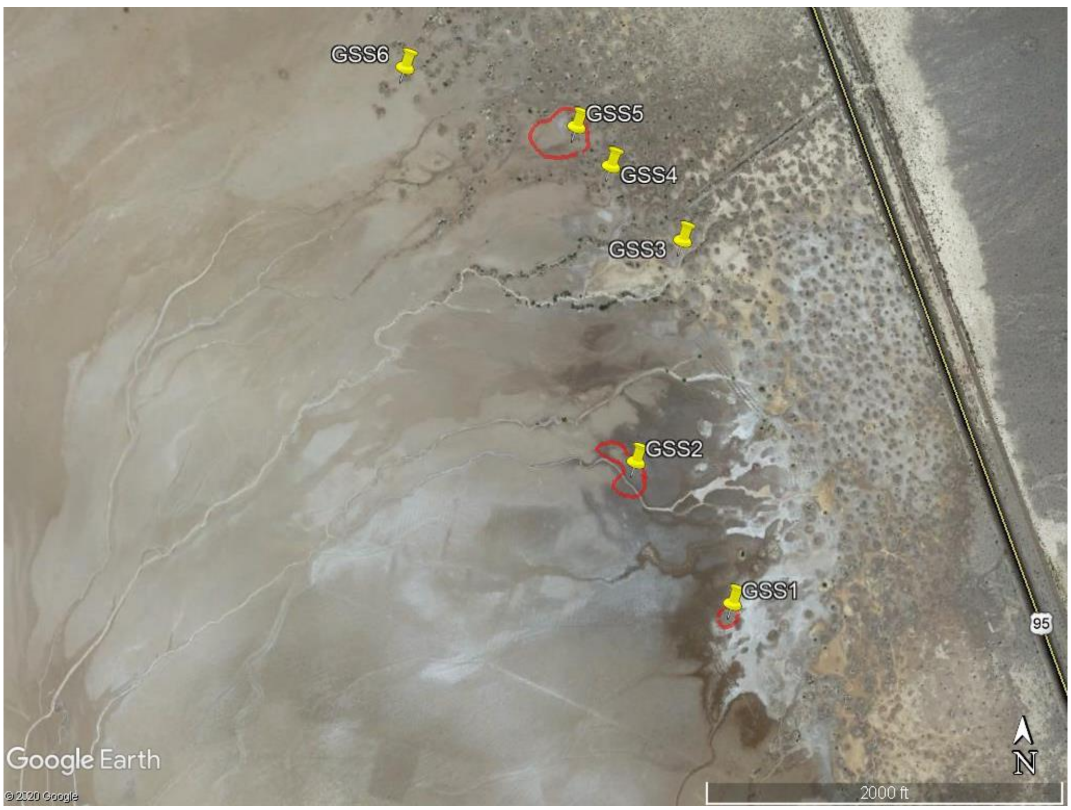

Figure 4-10: Locations of surface settlement features documented during the GEER reconnaissance (*Google Earth*).

Figure 4-11: Aerial view of the circular subsidence feature labelled GSS1 (*photo courtesy of Conni De Masi Castillo, UNR).*

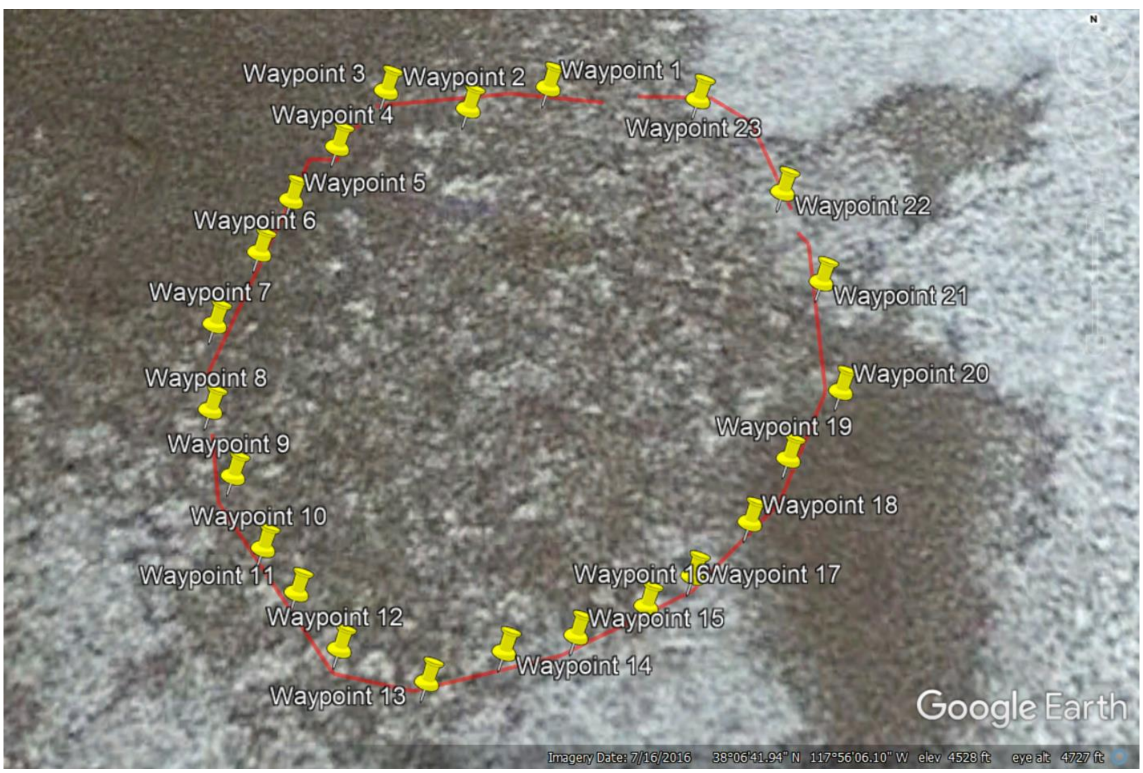

Figure 4-12: Waypoint locations associated with subsidence feature GSS1 (copyright *Google Earth*).

Figure 4-13: Aerial view of the kidney-bean shaped subsidence feature labelled GSS2 (*photo courtesy of @snowhorse420 on Twitter*).

Figure 4-14: Waypoint locations associated with subsidence feature GSS2 (copyright *Google Earth*).

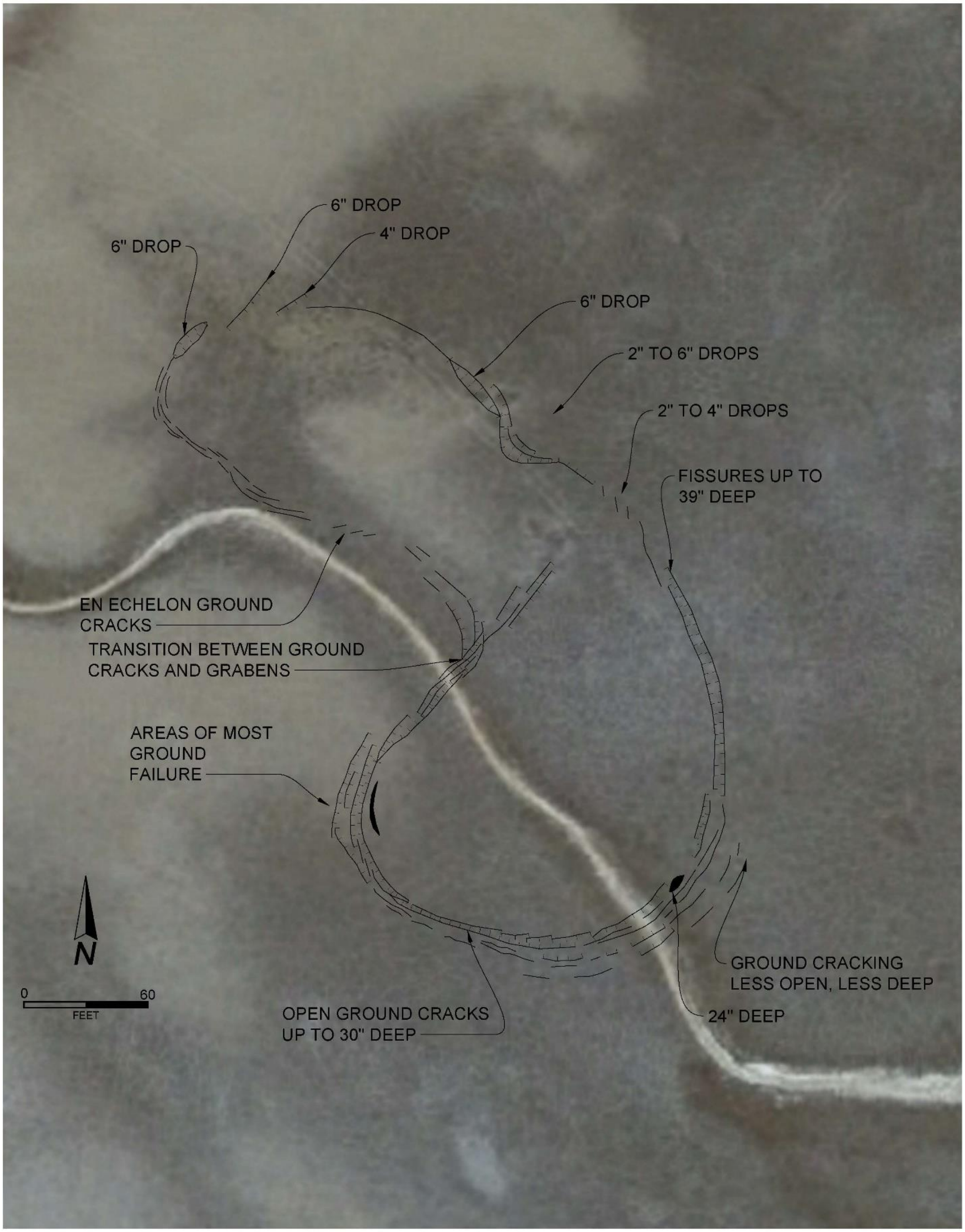

Figure 4-15: Feature GSS2 with mapped and notated features. Teeth indicate downdropped portion of grabens (Photo from Google Earth).

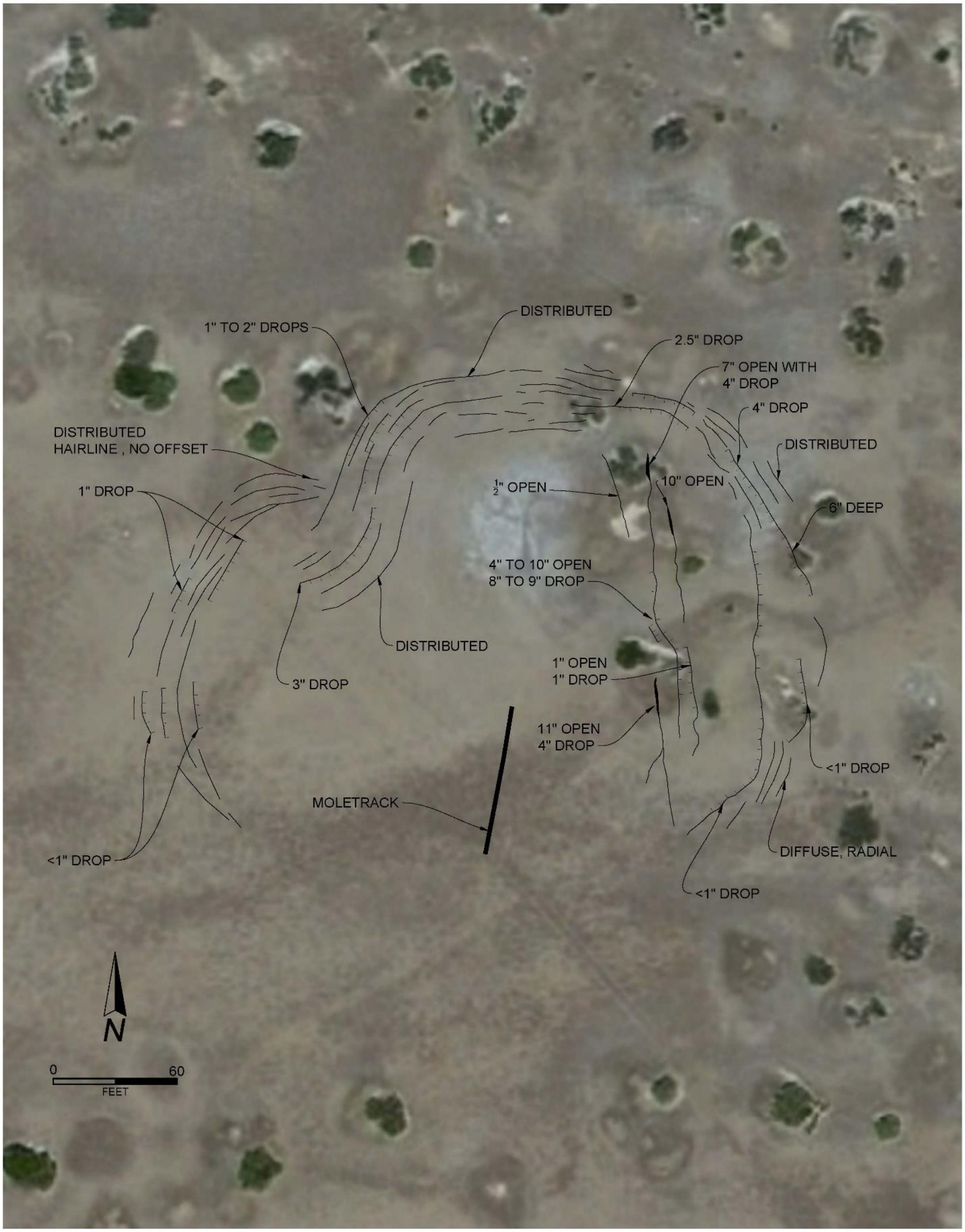

Figure 4-16: Feature GSS5 with mapped and notated features. Teeth indicate downdropped portion of grabens (Photo from Google Earth).

Table 4-1: Measurements of graben and block widths at subsidence feature GSS1.

Waypoint	Latitude, Longitude (°)	Description (Blocks bounded by surface cracks are described in order of innermost to outermost)
1	38.11181, -117.93497	Single block of horizontal width 64”. No vertical offset.
2	38.11179, -117.93502	Single block of horizontal width 49” and a vertical displacement of 15”.
3	38.11181, -117.93508	3 blocks observed with no vertical offset. Innermost block width is 30”, middle block width is 37”, and outermost block width is 38”.
4	38.11177, -117.93511	2 blocks observed with one gap in between. Innermost block width is 28”. Gap is 7” wide and 19” deep. Outermost block width is 87”.
5	38.11174, -117.93514	Six blocks observed with one gap between the third and fourth blocks. Innermost block is 22” wide. Second block is 25” wide. Third block is 24” wide. Gap is 15” wide and 27” deep. Fourth block is 65” wide. Fifth block is 23” wide. Outermost block is 21” wide.
6	38.11171, -117.93517	Five blocks observed with one gap between the innermost and second blocks. Innermost block is 67” wide with a vertical offset of 2” at its outermost edge. Gap is 22” wide and 22” deep. Second block is 22” wide. Third block is 35” wide. Fourth block is 25” wide. Outermost block is 25” wide.
7	38.11168, -117.93519	Seven blocks observed with a ap between the second and third blocks. Innermost block is 40” wide. Second gap is 20” wide and appears to slump inward. Gap is 17” wide and 32” deep. Fourth block is 20” wide. Fifth block is 18” wide. Sixth block is 20” wide. Outermost block is 17” wide.
8	38.11163, -117.93519	Seven blocks observed with gap between third and fourth blocks. Innermost block is 30” wide. Second block is 28” wide. Third block is 20” wide. Gap is 20” wide and 20” deep. Fourth block is 23” wide. Fifth block is 24” wide. Sixth block is 23” wide. Outermost block is 25” wide.
9	38.11160, -117.93517	Six blocks observed with two gaps between third and fourth blocks and between fourth and fifth blocks. Innermost block is 12” wide. Second block is 40” wide. Third block is 22” wide. First gap is 4” wide and 12” deep. Fourth block is 8” wide. Second gap is 11” wide and 18” deep. Fifth block is 34” wide. Outermost block is 53” wide.
10	38.11156, -117.93516	Five blocks observed with one gap between innermost and second blocks. Innermost block is 44” wide. Gap is 10” wide and 22” deep. Second block is 15” wide. Third block is 25” wide. Fourth block is 16” wide. Outermost block is 31” wide.
11	38.11155, -117.93513	Five blocks observed with one gap between innermost and second blocks. Innermost gap is 30” wide. Gap is 10” wide and 4” deep. Second block is 30” wide. Third block is 33” wide. Fourth block is 32” wide. Outermost block is 34” wide.
12	38.11152, -117.93511	Four blocks observed with no vertical offset. Innermost block is 44” wide. Second block is 12” wide. Third block is 30” wide. Outermost block is 48” wide.
13	38.11150, -117.93506	Three blocks observed with one gap between middle and outermost blocks. Innermost block is 55” wide. Middle block is 41” wide. Gap is 4” wide and 24” deep. Outermost block is 46” wide.
14	38.11152, -117.93501	Five blocks observed with two gaps between second and third blocks and third and fourth blocks. Innermost block is 48” wide. Second block is 22” wide. First Gap is

		2” wide and 17” deep. Third block is 13” wide. Second gap is 6” wide and 17” deep. Fourth block is 37” wide. Outermost block is 49” wide.
15	38.11152, -117.93497	Six blocks observed with two gaps between innermost and second blocks and second and third blocks. Innermost block is 30” wide. First gap is 19” wide and 19” deep. Second block is 14” wide. Second gap is 5” wide and 2” deep. Third block is 7” wide. Fourth block is 28” wide. Fifth block is 3” wide. Outermost block is 38” wide.
16	38.11153, -117.93493	Six blocks observed with one gap between second and third blocks. Innermost block is 35” wide. Second block is 19” wide. Gap is 10” wide and 18” deep. Third block is 24” wide. Fourth block is 19” wide. Fifth block is 28” wide. Outermost block is 12” wide.
17	38.11155, -117.93491	Four blocks observed with one debris-filled gap between innermost and second blocks. Innermost block is 33” wide. Gap is 34” wide and 23” deep to the bottom of the debris. Second block is 40” wide. Third block is 36” wide. Outermost block is 26” wide.
18	38.11157, -117.93487	Six blocks observed with one gap between third and fourth blocks. Innermost block is 47” wide. Second block is 30” wide. Third block is 30” wide. Gap is 18” wide and 22” deep. Fourth block is 20” wide. Fifth block is 20” wide. Outermost block is 16” wide.
19	38.11160, -117.93484	Six blocks observed with one gap between second and third blocks. Innermost block is 30” wide. Second block is 34” wide. Gap is 25” wide and 18” deep. Third block is 35” wide. Fourth block is 22” wide. Fifth block is 25” wide. Outermost block is 13” wide.
20	38.11163, -117.93480	Four blocks observed with one gap between innermost and second blocks. Innermost block is 15” wide. Gap is 3” wide and 40” deep. Second block is 53” wide. Third block is 34” wide. Outermost block is 44” wide.
21	38.11169, -117.93480	Four blocks observed with one gap between innermost and second blocks. Innermost block is 21” wide. Gap is 5” wide and 19” deep. Second block is 13” wide. Third block is 16” wide. Outermost block is 63” wide.
22	38.11174, -117.93482	Four blocks observed amongst very diffuse cracking. Gap observed between second and third blocks. Innermost block is 40” wide. Second block is 40’ wide. Gap is 12” wide and 16” deep. Third block is 52” wide. Outermost block is 76” wide.
23	38.11180, -117.93487	Five blocks observed amongst very diffuse cracking. No offset or gaps observed. Innermost block is 30” wide. Second block is 15” wide. Third block is 30” wide. Fourth block is 37” wide. Outermost block is 99” wide.

Figure 4-17: Waypoint 1 of subsidence feature GSS1 (*lat/lon = 38.11181, -117.93497*).

Figure 4-18: Waypoint 2 of subsidence feature GSS1 (*lat/lon = 38.11179, -117.93502*).

Figure 4-19: Waypoint 3 of subsidence feature *GSS1 (lat/lon = 38.11181, -117.93508).*

Figure 4-20: Waypoint 4 of subsidence feature GSS1 *(lat/lon = 38.11177, -117.93511).*

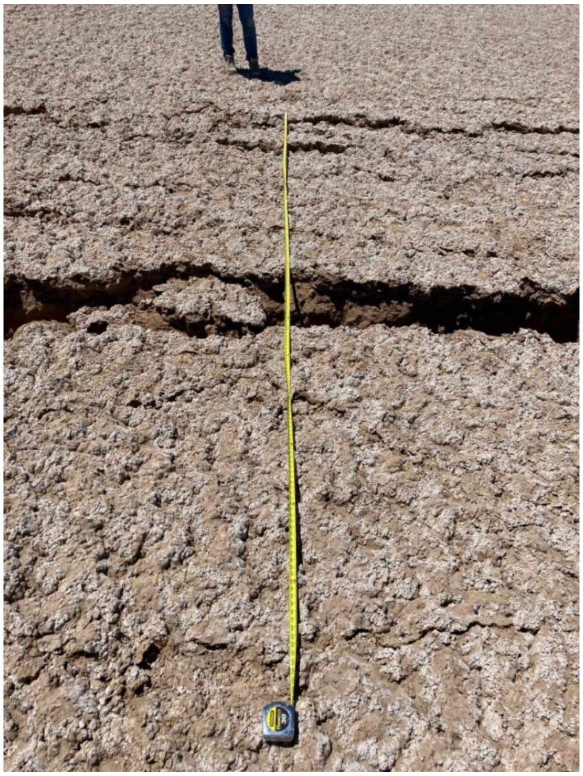

Figure 4-21: Waypoint 6 of subsidence feature GSS1 (*lat/lon =38.11171, -117.93517*).

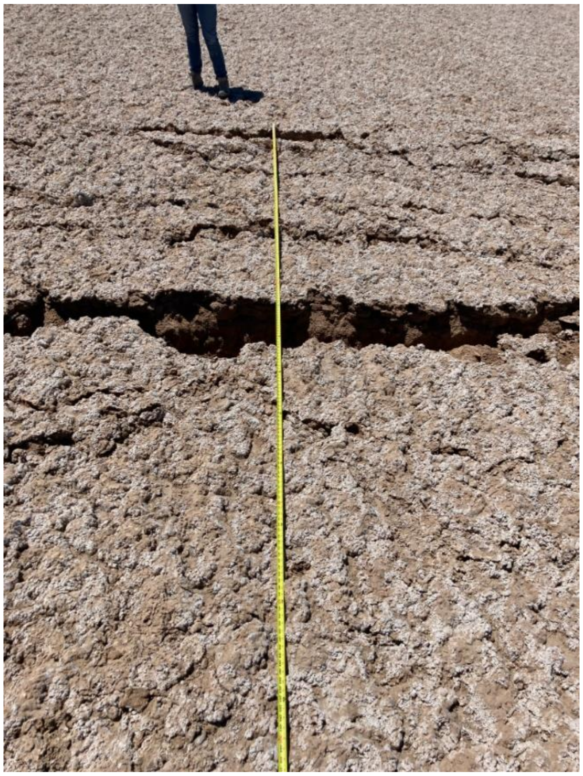

Figure 4-22: Waypoint 8 of subsidence feature GSS1 (*lat/lon = 38.11163, -117.93519*).

Figure 4-23: Waypoint 9 of subsidence feature GSS1 (*lat/lon = 38.11160, -117.93517*).

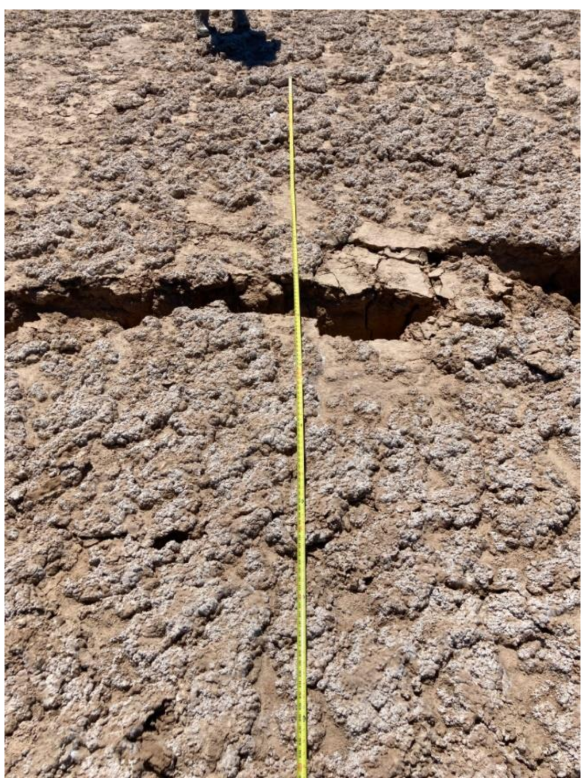

Figure 4-24: Waypoint 10 of subsidence feature GSS1 (*lat/lon = 38.11156, -117.93516*).

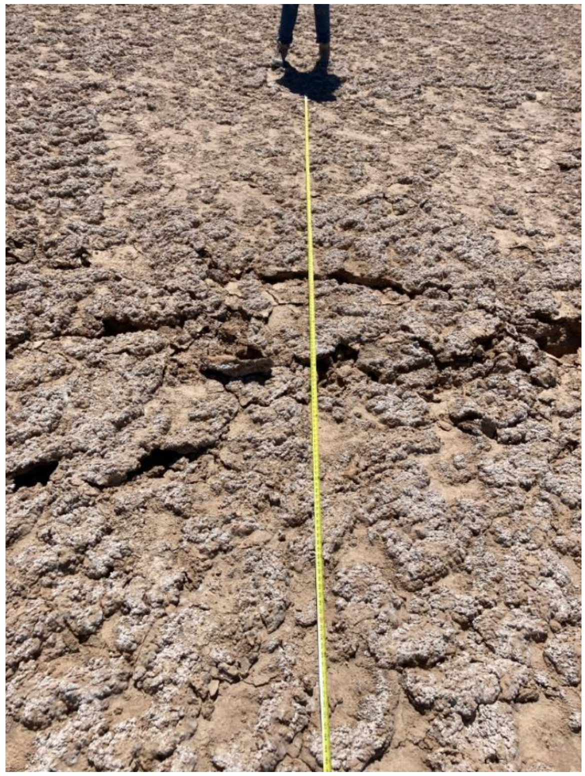

Figure 4-25: Waypoint 11 of subsidence feature GSS1 (*lat/lon = 38.11155, -117.93513*).

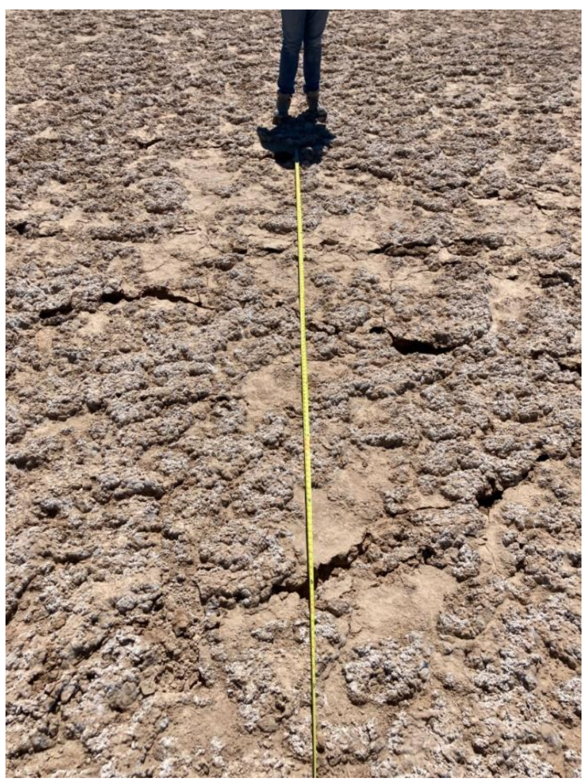

Figure 4-26: Waypoint 12 of subsidence feature GSS1 (*lat/lon = 38.11152, -117.93511*).

Figure 4-27: Waypoint 13 of subsidence feature GSS1 (*lat/lon = 38.11150, -117.93506*).

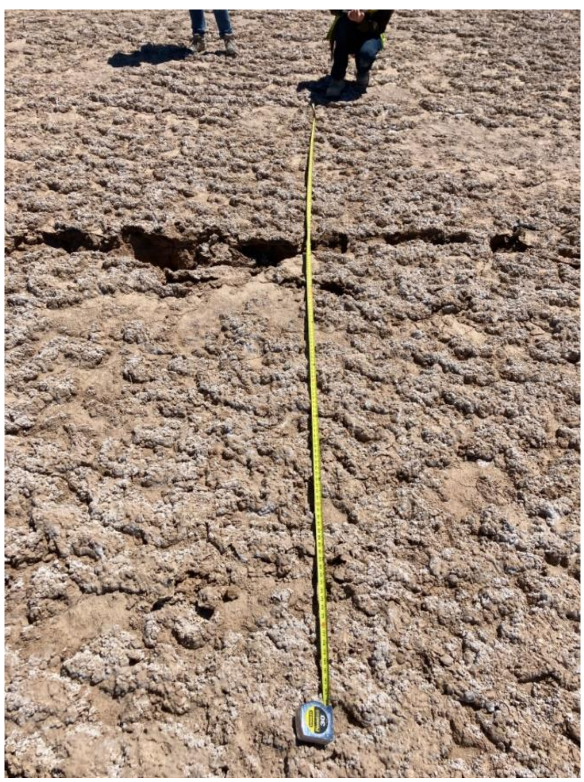

Figure 4-28: Waypoint 14 of subsidence feature GSS1 (*lat/lon = 38.11152, -117.93501*).

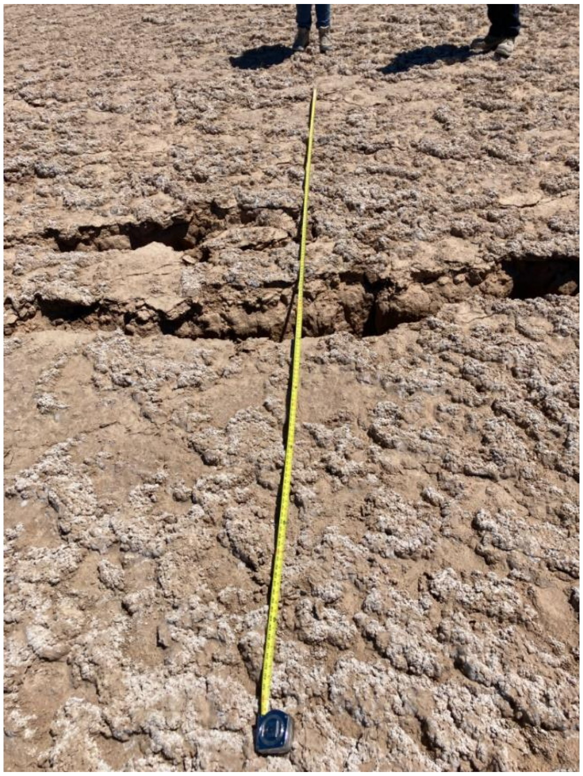

Figure 4-29: Waypoint 15 of subsidence feature GSS1 (*lat/lon = 38.11152, -117.93497*).

Figure 4-30: Waypoint 16 of subsidence feature GSS1 (*lat/lon = 38.11153, -117.93493*).

Figure 4-31: Waypoint 17 of subsidence feature GSS1 (*lat/lon = 38.11155, -117.93491*).

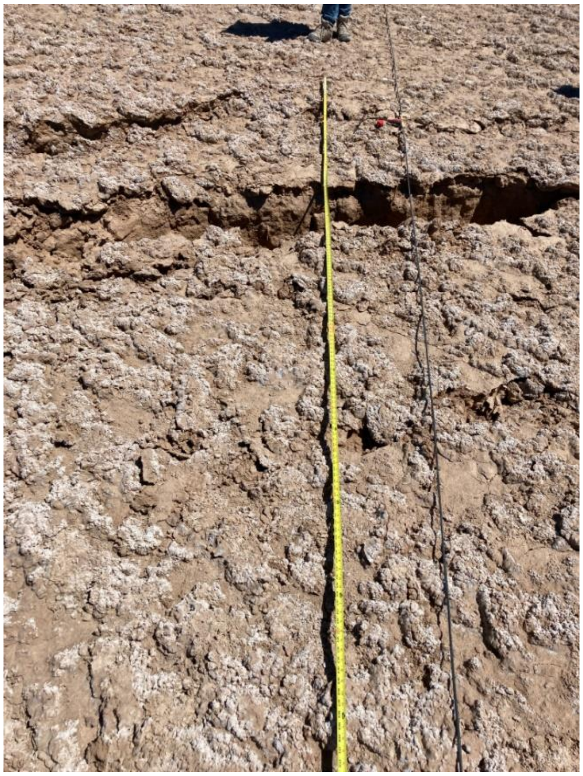

Figure 4-32: Waypoint 18 of subsidence feature GSS1 (*lat/lon = 38.11157, -117.93487*).

Figure 4-33: Waypoint 19 of subsidence feature GSS1 (*lat/lon = 38.11160, -117.93484*).

Figure 4-34: Waypoint 20 of subsidence feature GSS1 (*lat/lon = 38.11163, -117.93480*).

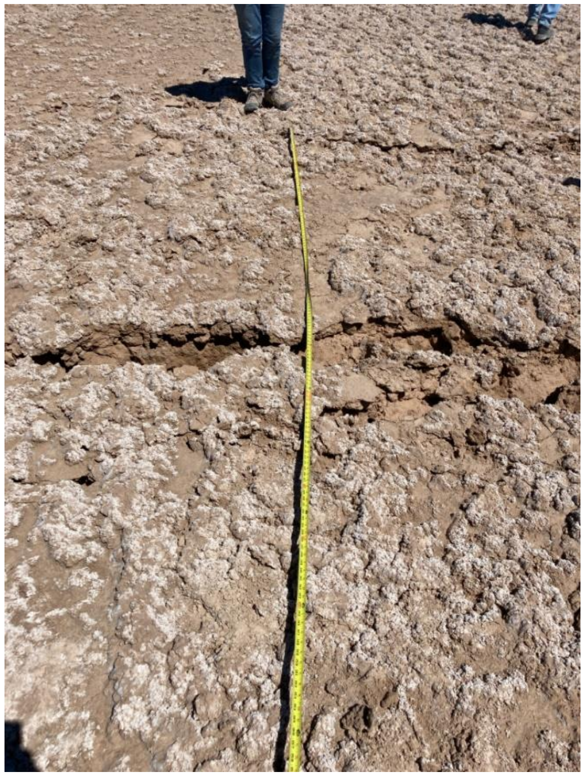

Figure 4-35: Waypoint 21 of subsidence feature GSS1 (*lat/lon = 38.11169, -117.93480*).

Figure 4-36: Waypoint 22 of subsidence feature GSS1 (*lat/lon = 38.11174, -117.93482*).

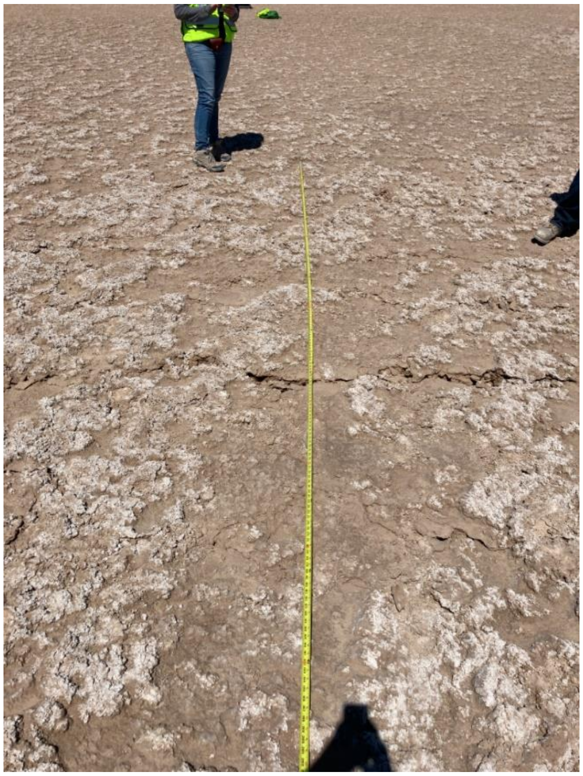

Figure 4-37: Waypoint 23 of subsidence feature GSS1 (*lat/lon = 38.11180, -117.93487*).

Table 4-2: Measurements of ground surface displacements at subsidence feature GSS2

Waypoint	Latitude, Longitude (°)	Description
1	38.11355, -117.93671	
2	38.11368, -117.93661	
3	38.11385, -117.93703	
4	38.11398, -117.93707	
5	38.11430, -117.93746	
6	38.11405, -117.93736	
7	38.11433, -117.9371	
8	38.11387, -117.93662	45” wide debris-filled fissure. 39” to the bottom of the debris.
9	38.11417, -117.93697	3 grabens observed. First graben (outermost) is 43” wide with no vertical offset. Second (middle) graben is 51” wide and drops 6” at its outer edge. Second graben appears to slump inward. Third graben (innermost) is 49” wide and contains a crack 30” in from its outermost edge. The third graben has an offset of 4” at its outer edge. There exists a 10”-wide 28”-deep gap adjacent to the innermost edge of the third graben.
10	38.11422, -117.93699	
11	38.11422, -117.93754	
12	38.11390, -117.93683	

Figure 4-38: Ground surface displacements at Waypoint 1 of subsidence feature GSS2 (*lat/lon = 38.11355, -117.93671*).

Figure 4-39: Ground surface displacements at Waypoint 1 of subsidence feature GSS2 looking northwest (*lat/lon = 38.11355, -117.93671*).

Figure 4-40: Ground surface displacements at Waypoint 2 of subsidence feature GSS2 (*lat/lon = 38.11368, -117.93661*).

Figure 4-41: Ground surface displacements at Waypoint 2 of subsidence feature GSS2 looking southeast (*lat/lon = 38.11368, -117.93661*).

Figure 4-42: Ground surface displacements at Waypoint 3 of subsidence feature GSS2 looking northwest (*lat/lon = 38.11385, -117.93703*).

Figure 4-43: Ground surface displacements at Waypoint 3 of subsidence feature GSS2 looking southeast (*lat/lon = 38.11385, -117.93703*).

Figure 4-44: Ground surface displacements at Waypoint 4 of subsidence feature GSS2 (*lat/lon = 38.11398, -117.93707).*

Figure 4-45: Ground surface displacements at Waypoint 6 of subsidence feature GSS2 looking northeast (*lat/lon = 38.11405, -117.93736*).

Figure 4-46: Ground surface displacements at Waypoint 7 of subsidence feature GSS2 looking northeast (*lat/lon = 38.11433, -117.93716).*

Figure 4-47: Ground surface displacements at Waypoint 7 of subsidence feature GSS2 (*lat/lon = 38.11433, -117.93716).*

Figure 4-48: Ground surface displacements at Waypoint 9 of subsidence feature GSS2 *(lat/lon = 38.11417, -117.93697).*

Figure 4-49: Ground surface displacements at Waypoint 10 of subsidence feature GSS2 looking southwest (*lat/lon = 38.11422, -117.93699).*

Figure 4-50: Ground surface displacements at Waypoint 10 of subsidence feature GSS2 (*lat/lon = 38.11422, -117.93699).*

4.4 Ground Surface Settlement Patterns

With regard to the circular pattern of the observed settlements at ground surface which were presented in Section 4.3, a hypothesis is that there are buried salt layers in the playa that resulted from evaporation on older (now buried) soil horizons. The salt layers are basically circular because they were surface ponds that formed in localized low points. These salt layers are then buried. During the earthquake, the salt crystals were crushed and the ground collapsed. This could explain why all of the settlement features looked like the ground had settlement and rotated into the middle of the feature. This hypothesis should be tested using additional field tests such as boring logs accompanied with sampling at frequent interval depths.

5.0 Earthquake Ground Shaking Characteristics

This section describes the recorded ground motions and reported shaking intensity from the **M**6.5 Monte Cristo Range Earthquake on May 15, 2020.

5.1 Recorded Ground Motions

The **M**6.5 Monte Cristo Range earthquake was recorded by at least 222 strong motion recording stations, belonging to 9 different networks (Table 5-1), located within a distance of about 450 km from the epicenter. The vast majority of these records are included as part of the Center for Engineering Strong Motion Data (CESMD) data-set for this event, while at least two additional nearby recordings (i.e., NN-TVH1 and IM-NV31) can be obtained from the Incorporated Research Institutions for Seismology (IRIS).

Table 5-1: Stations and networks that recorded the May 15, 2020 M6.5 Event (CESMD, 2020; IRIS, 2020)

Network Code	**# of Stations**	**Network Name**
NP	62	National Strong-Motion Project (NSMP), USGS
NC	61	Northern California Seismic Network (NCSN), USGS
CI	28	Southern California Seismic Network (SCSN), Caltech
BK	25	Berkeley Digital Seismic Network (BDSN), University of California at Berkeley
CE	18	California Strong Motion Instrumentation Program (CSMIP), CGS
NN	18	Nevada Seismic Network, UNR/NSL
WR	6	California Division of Water Resources (CDWR)
GS	3	U.S. Geological Survey Networks (USGS)
IM	1	International Miscellaneous Stations
TOTAL	**222**	

Strong motion station coverage in Nevada is sparse, and seismographs in the subject study area included by the CESMD and IRIS data sets for this event are primarily concentrated in California. The locations of the seismographs and their approximate Peak Ground Accelerations (PGAs) are mapped in Figure 5-1. A plot of measured PGA versus distance to the epicenter is presented in Figure 5-2, in relation to the Boore & Atkinson (2008) Ground Motion Prediction Equation (GMPE), which assumes a soil shear wave velocity in the upper 30 m (Vs30) of 760 m/s. This figure was directly obtained from CESMD (2020). A map modelling approximate contours of the peak horizontal ground acceleration for this event is presented in Figure 5-3.

The seven stations in Table 5-2 below were selected for closer examination and processing, due to their relatively close epicentral distance and/or high PGA. It is interesting to note that the highest PGA of 0.051g was recorded at the Bridgeport, California CE-65654 recording station, which was located 119 km away from the epicenter. It is believed that “looser” soil conditions at CE-65654, as indicated by the inferred Vs30 and its location within an alluvial valley, may have attributed to greater ground motion amplification at this site, as opposed to the other listed sites situated closer to the epicenter.

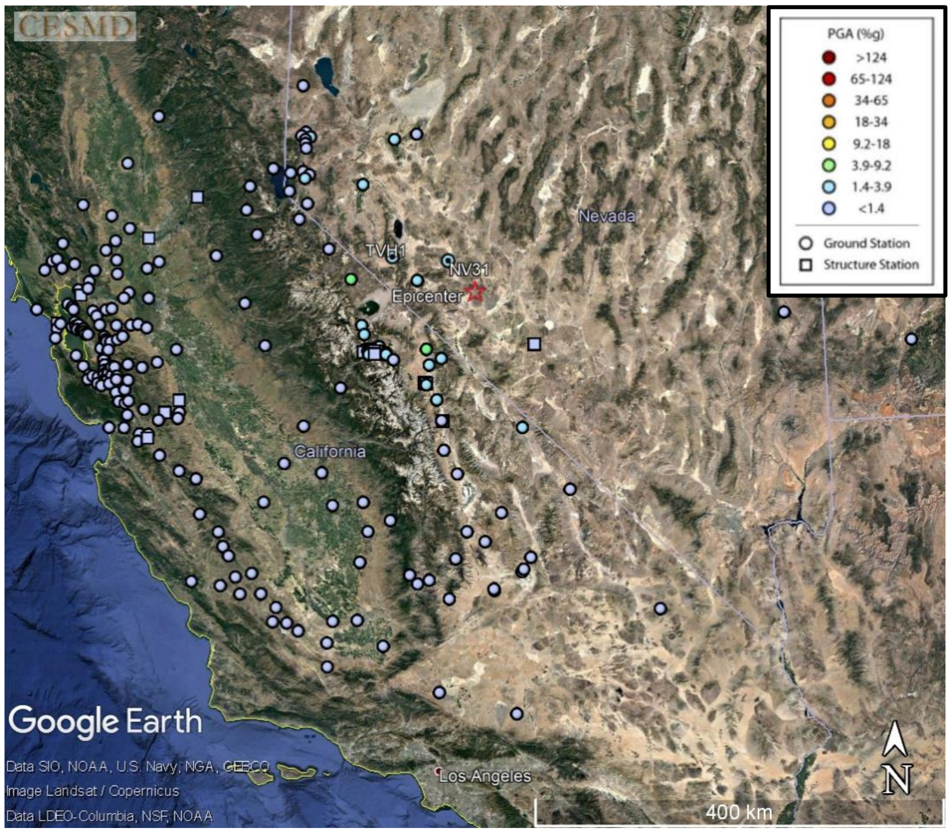

Figure 5-1: Map of CESMD and some IRIS recording stations for the May 15, 2020 event, depicting the approximate PGA at each station (CESMD, 2020; Iris, 2020; Google Earth).

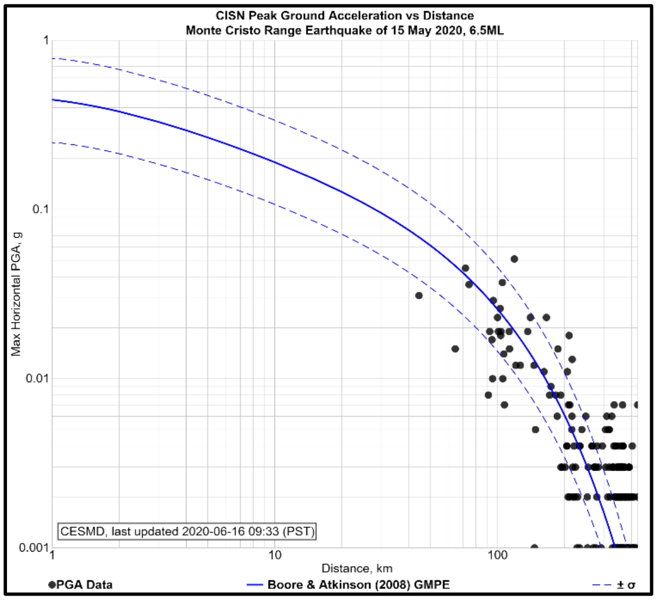

Figure 5-2: Chart showing PGA vs. distance for the May 15, 2020 event (CESMD, 2020).

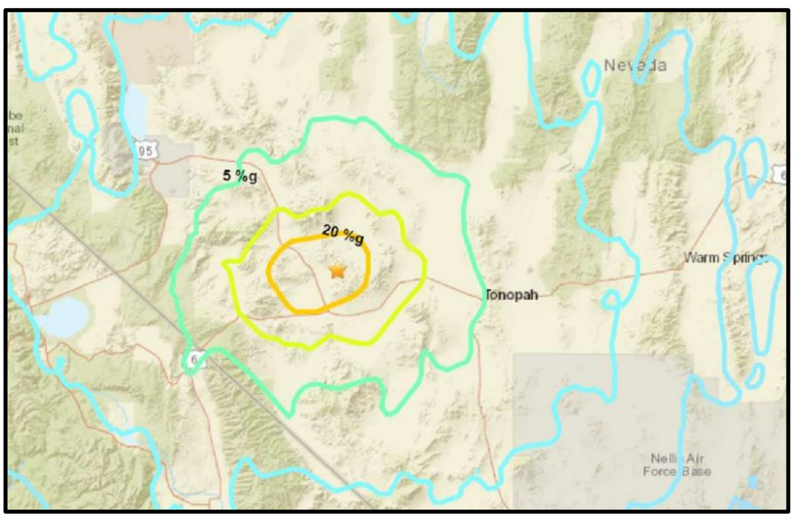

Figure 5-3: ShakeMap computer program modeled PGA contours for the May 15, 2020 event (Program version 4.0; Worden, et. al., 2020).

The processed ground motion data (3 components) for six of these seven sites was downloaded from CESMD (2020), and plots of the acceleration, velocity, displacement, arias intensity, and acceleration response spectra were reproduced in Appendix A. The NN-TVH1 raw ground motion data was downloaded from IRIS (2020), and time history and spectral plots are similarly included for this station in Appendix A. However, NN-TVH1 required manual detrending and demeaning of the acceleration history, and may still include high frequency motions that should be removed prior to any future engineering analyses.

Table 5-2: Details for selected recording stations (CESMD 2020; IRIS 2020)

Network Code/ Station ID	Station Name	Lat/Long	Epicentral Distance (km)	PGA (g)	Vs30 (m/s)
NN-LHV	Little Huntoon Valley Nevada w84gm	38.251, 118.505	56.1	0.031	477 (inferred)
NN-TVH1	TV Hill 1, Hawthorne, NV	38.457, -118.766	56.2	0.031	698 (inferred)
CE-54428	Chalfant; Zack Ranch	37.662, -118.399	71.8	0.045	322 (inferred)
NP-1679	Chalfant Valley; Fire Station	37.528, -118.367	82.4	0.036	301 (inferred)
CE-54388	Bishop; 2-story Office Bldg	37.370, -118.397	98.9	0.024	522 (measured)
NC-MLI	Lincoln Peak	37.637, -119.018	116.0	0.036	557 (inferred)
CE-65654	Bridgeport; Main & School Street	38.255, -119.229	119.1	0.051	336 (inferred)

*Vs30, if available, has been either inferred from Vs30 maps or measured directly (CESMD, 2020)

The **M**6.5 event was also recorded by the "NVAR Array Site 31" in Mina, Nevada, about 35 km from the epicenter, as shown on Figure 5-4. The recorded motions were downloaded from IRIS (2020) and processed, however, it appears that the recording instrument reached a maximum acceleration limit near 0.025 g, causing erratic behavior. Due to this malfunction, that record is not considered further in this report.

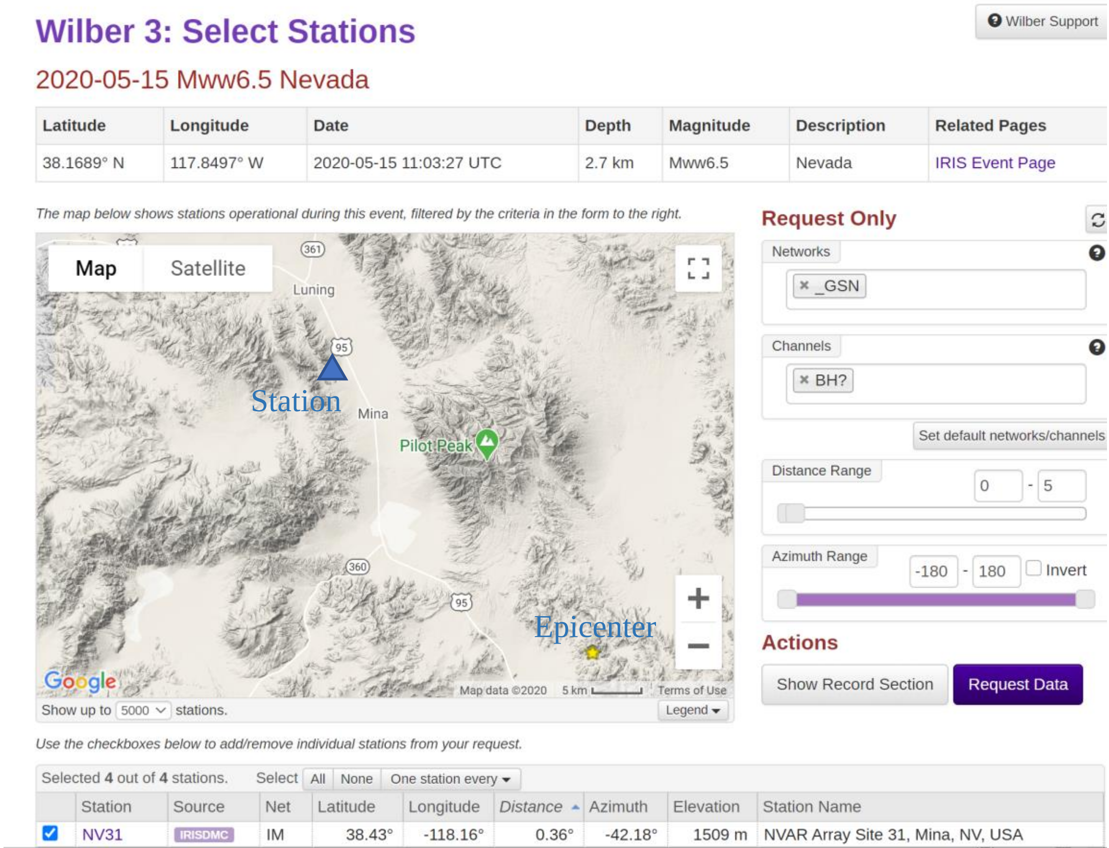

Figure 5-4: IRIS Ground motion recording station for the May 15, 2020 Monte Cristo Range earthquake (Wilber3; Newman et al, 2013).

5.2 Observations Near Recording Stations

The GEER team visited the location of the "CE-65654 Bridgeport – Main & School Street" recording station on June 10, 2020. This station is located in Bridgeport, California and is housed within the property of the Bridgeport Fire Station building. Several open fields and streams surround the town of Bridgeport. The GEER team examined the area surrounding the Fire Station building, as well a nearby stream channel flowing towards the Bridgeport Reservoir (Figure 5-5). No signs of earthquake damage or ground failure were observed.

(a)

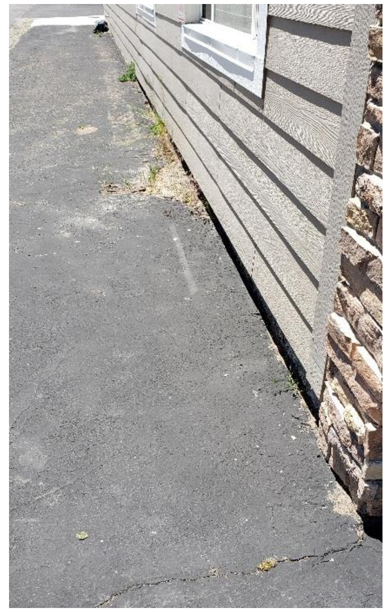

(b)

(c)

Figure 5-5: Bridgeport, CA photos near recording station CE-65654 with no signs of earthquake damage; (a) West facing view of Bridgeport Fire Station building front (*lat/long = 38.2557, -119.2288)*, (b) east floor edge of Fire Station building (sand shown likely wind-blown from nearby properties and settled within pre-earthquake asphalt spalls and cracks; *lat/long = 38.2556*, -*119.2289*), (c) stream channel east of town of Bridgeport, CA with no observable ground failure (*lat/long = 38.2571*, -*119.2236*).

6.0 Rockfalls

The GEER team documented on June 8, 2020, the aftermath of an earthquake-induced rockfall that occurred on the southwestern end of an isolated rocky ridgeline located east of US95 at Latitude 38° 8'45.74"N and Longitude 117°56'40.07"W as shown in Figure 6-1.

The rockfall debris included one large boulder (shown in Figure 6-3 to 6-4) with a debris cone consisting of smaller, angular cobbles to boulders of widths on the order of 0.5m (shown in Figure 6-5 to 6-6). The boulder was approximately 2.7m at its widest point and had travelled approximately 12m from the cliff face. Figure 6-2 shows the position of the large boulder as it was located on the rockface prior to the Monte Cristo Earthquake and is compared with a similar view as seen from US95 after the rockfall event.

As mapped by Stewart, Kelleher, and Zorich (1994), the western portion of the ridgeline is underlain by the Roberts Mountains Allochthon, consisting of Late Devonian to Late Cambrian siliceous and volcanic rocks. The rockface, including the source area of the rockfall, consisted of several different rock types, including breccia, shale, and a shear zone. The rock mass surrounding the source area of the boulder was moderately fractured, with planar fractures spaced at approximately 0.15m to 0.6m. The intact boulder appeared to be much larger than the spacing of the rock mass surrounding its original position, as well as being lithologically distinct.

The GEER team traversed the perimeter of the promontory looking for further evidence of rockfall. Several small debris cones and impact scars appeared fresh to slightly weathered, such as in Fig 6-7, but it was not clear that these rock falls were due to the recent earthquake. Several cobble-sized and smaller clasts were observed with fresh to slightly weathered surfaces, generally located within a meter of the toe of the slope. These features were located along the western slope face of the promontory that included the main rockfall. No significant recent rock fall features were observed on the north, east, and south sides of the promontory.

Figure 6-1: Location of rockfall within hill located west of US95.

Figure 6-2: Before and after images of the rockfall (*lat/lon = 38.145794, -117.94509*). Google street view image is from August 2018.

Figure 6-3: Boulder from the rockfall, looking northwest (*lat/lon = 38.14613078, -117.944488056*).

Figure 6-4: Boulder from the rockfall, looking west. Smaller debris is visible at the bottom of the picture. (*lat/lon = 38.14613078, -117.944488056*).

Figure 6-5: Rockfall debris located between the boulder and the rockface, looking east. (*lat/lon = 38.14596278, -117.9445302*).

Figure 6-6: Rockfall debris located between the boulder and the rockface, looking northwest. (*lat/lon = 38.047707, -117.896156*).

Figure 6-7: Fresh to slightly weathered impact scar on rock outcrop, south of main rockfall. (*lat/lon = 38. 1458, -117. 1457*).

7.0 Field and Laboratory Tests

7.1 Refraction Microtremor Surveys

Six Refraction Microtremor (ReMi) seismic surveys were performed at the playa ground failure sites to provide a preliminary evaluation of the soil stiffness and possible layering/depth of ground failures. ReMi surveys provide means to obtain basic subsurface stiffness information on an essentially continuous basis across the explored location without physical intrusion. ReMi data was collected with an 88-m-long array of 12 vertical-component geophones in a straight line. The ReMi method utilizes background vibrations and determines the slowest arrival time for shear waves to determine the shear-wave velocity based on Raleigh-Wave characteristics. A slowness versus frequency wave transformation is obtained for multiple 30-second readings, and picks are made of the shear-wave velocity and layer thickness from the dispersion curve. The method is cost effective but is subject to some subjective interpretation of the layering and thickness by the modeler. The layout of the geophone lines (where crossing locations of ground failure zones) was discussed with the modeler so that layer boundaries were more or less consistent between different crossing ReMi lines. Louie (2001) estimates that ReMi can provide a 30-m depth estimate of shear wave velocity within 20% accuracy. It is acknowledged that the accuracy would decrease at deeper depths.

Three ReMi surveys were performed adjacent to ground failure site GSS1 (Figure 4-7), one was performed at the sand ejecta site (JP3), and two were performed on or adjacent to site GSS2. Two ReMi surveys were performed perpendicular to each other crossing the ground failure at site GSS1 (Line 2A east-west and line 2B north-south). A third line (2D) was conducted from the same starting point as Line 2B but in a westerly direction so as to lie entirely outside of the ground failure zone.

The JP3 site location (Line 3) was selected based on suspected ejecta from shrinkage cracks in this area (Figure 7-1). Site 3 was also approximately half-way between the lateral spread cracking under US 95 and the playa ground failures (Figure 7-2), and potentially might indicate typical conditions for the wider, lateral-spread type failure observed at the highway. However, the ground conditions may possibly change rapidly between the playa and lower alluvial fan depositional environment.

Figure 7-1: View facing south along ReMi Line 3 (lat/lon = 38.111691, -117.932915)

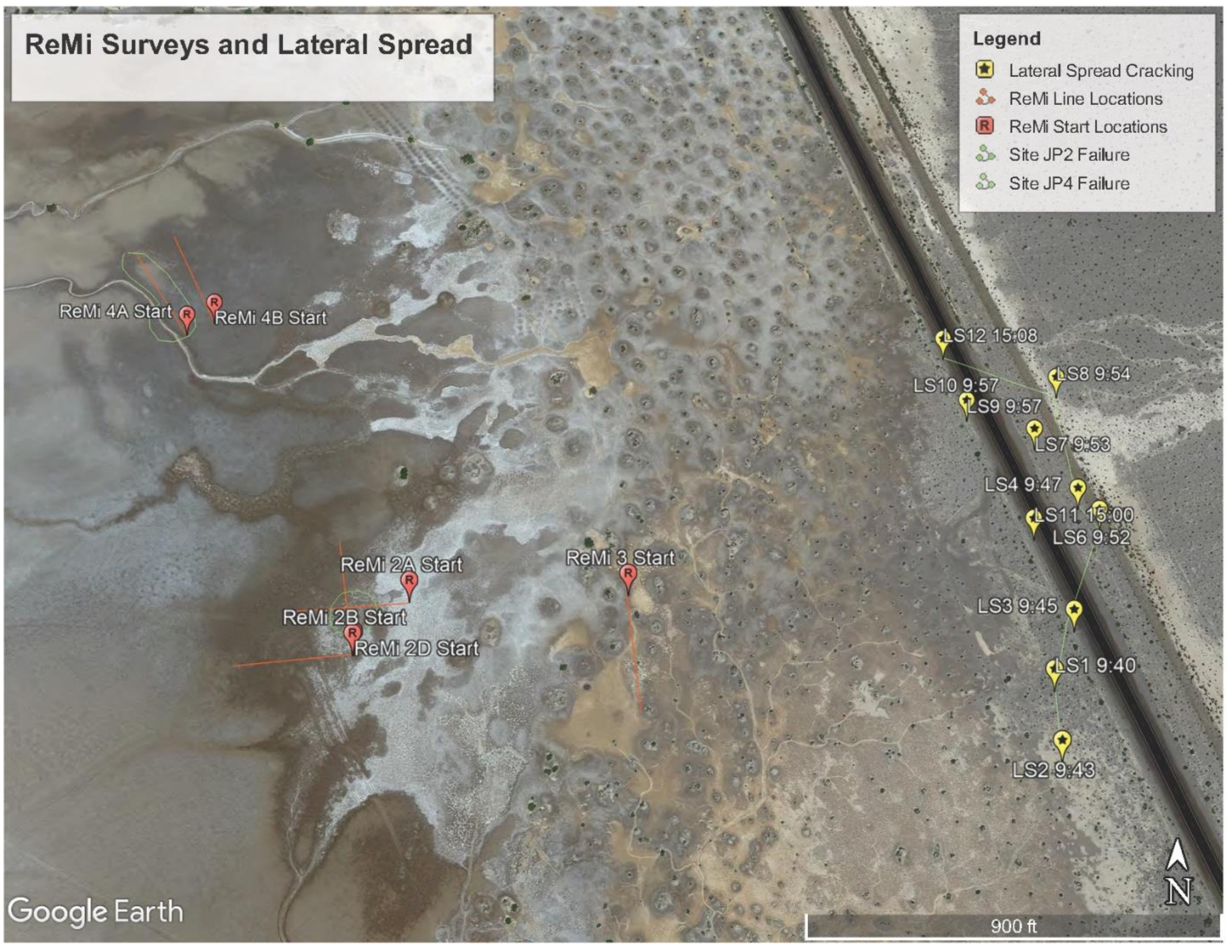

Figure 7-2: ReMi Survey Locations Relative to Playa Ground Failures and Alluvial Fan Lateral Spread Cracking at US95 (Background Image – Google Earth).

Two ReMi surveys were performed at GSS1/JP4. One survey (Line 4A) was entirely on the ground failure zone and the second survey (Line 4B) was about 30 m east of the ground failure zone and 60 m from Line 4A.

Two different results are provided from each ReMi survey – a 1-D profile (average for the entire line) and a 2-D profile. The 1-D profile is generated first for the entire survey, including the interpretation by the geologist. Second, the 2-D profile is generated for the central two-thirds of the ReMi line. The results for each subset of geophones is compared to the average overall results, to create a modified shear-wave velocity profile for multiple regions along the 88-m survey.

Results of the ReMi surveys are shown on Figure 7-3. There is little difference in shear wave velocity between the playa ground failure sites and sites without ground failure. Each site has a loose zone in the upper 0.45-0.7 m that may be associated with shrinkage cracks, and the shear-wave velocity to 8.5-10 m depth is less than 110 m/s. For sands, a shear-wave velocity of less than about 150 m/s would be interpreted as a loose granular material and below 200 m/s would indicate medium density and potential susceptibility to liquefaction during strong ground shaking (>0.3 g). However, the materials are likely to be intermediate/mixed fine-grained soils (with variable plasticity) for which there is no direct correlation between shear-wave velocity and strength/liquefaction potential. In any case, the soil type (granular versus fine-grained) cannot be determined from shear-wave velocity results. The moderate increase in shear wave velocity in all the seismic surveys at about 8.5 m depth suggests that there is a depositional, density, and/or aging boundary at this depth and (in combination with the expected vertical limits with depth of a 30 m wide failure zone) that ground failures potentially may not extend to greater than 8.5 m depth.

The inverse-weighted average in the upper 30 m (Vs30, used in determining building code site class) is slightly higher for the non-failure ReMi lines (151 m/s) compared to the ground failure zones (143 m/s). Site 3 was included as a ground failure site due to the sand ejecta, although no other failure features were noted. The average Vs30 for all six sites was 146 m/s with a standard deviation of 5 m/s. However, both results are within 2% of the average value at all sites and are unlikely to be statistically different from each other for a small sample size. Interestingly, both sites 2A and 4B without ground failure and the sand boil site have higher shear-wave velocity at greater than 22 m depth – 250 m/s versus ground-failure sites at about 200 m/s. These stronger layers may be primarily what increases the average Vs30 for the three non-liquefied sites. However, shear wave velocities at greater than about 20 m depth are often less reliable.

If the ReMi shear wave velocity differences at greater than 22 m depth are valid, it is possible that the primary mechanism that influenced ground failure was soil amplification/wave propagation through weaker soils immediately under the ground failure sites. The sites with lower shear-wave velocity profiles at depth would potentially have increased amplification of longer-period ground motions, which may have triggered ground failure in these localized areas.

Furthermore, the lateral variations in measurements observed in the vicinity of the ground failures (e.g., the shear wave velocity differences between Lines 4A and 4B below 22 feet depth, and the variation at all depths across Line 4A), may subject the soil profile to spatially incoherent wave propagation and scattering. This incoherency can potentially cause excessive tensile and compressive forces within the soil mass during shaking, which may result in observable ground distortions. However, it is also possible that the observed variations in shear-wave velocity are simply within the accuracy of ReMi interpretation and modeling.

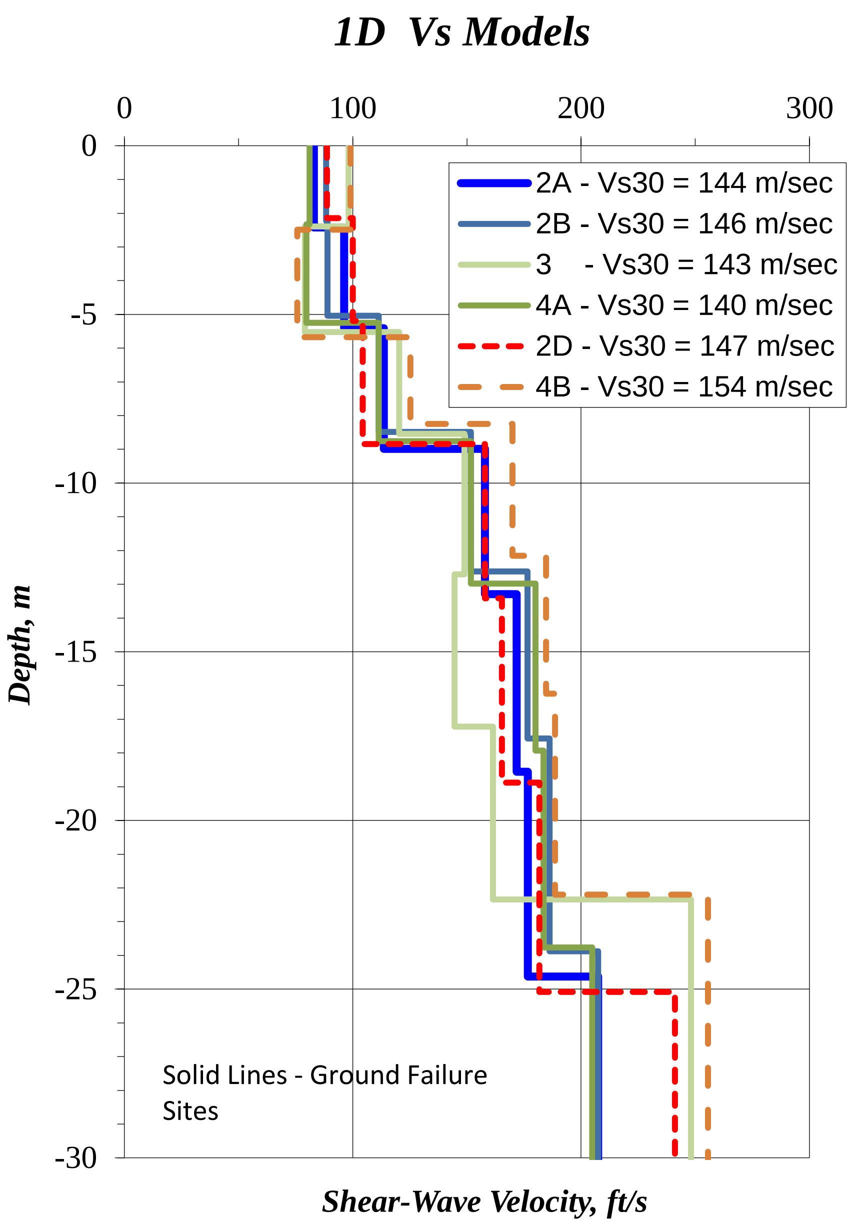

Figure 7-3: 1D ReMi Profiles of Shear-Wave Velocity versus Depth.

The presented shear wave velocity profiles in Figure 7-3 were obtained using an inversion process in which a number of data points were selected to fit a dispersion curve. Figures 7-4 to 7-9 present the measured dispersion curves and the picked data points to obtain the six shear velocity profiles shown in Figure 7-3.

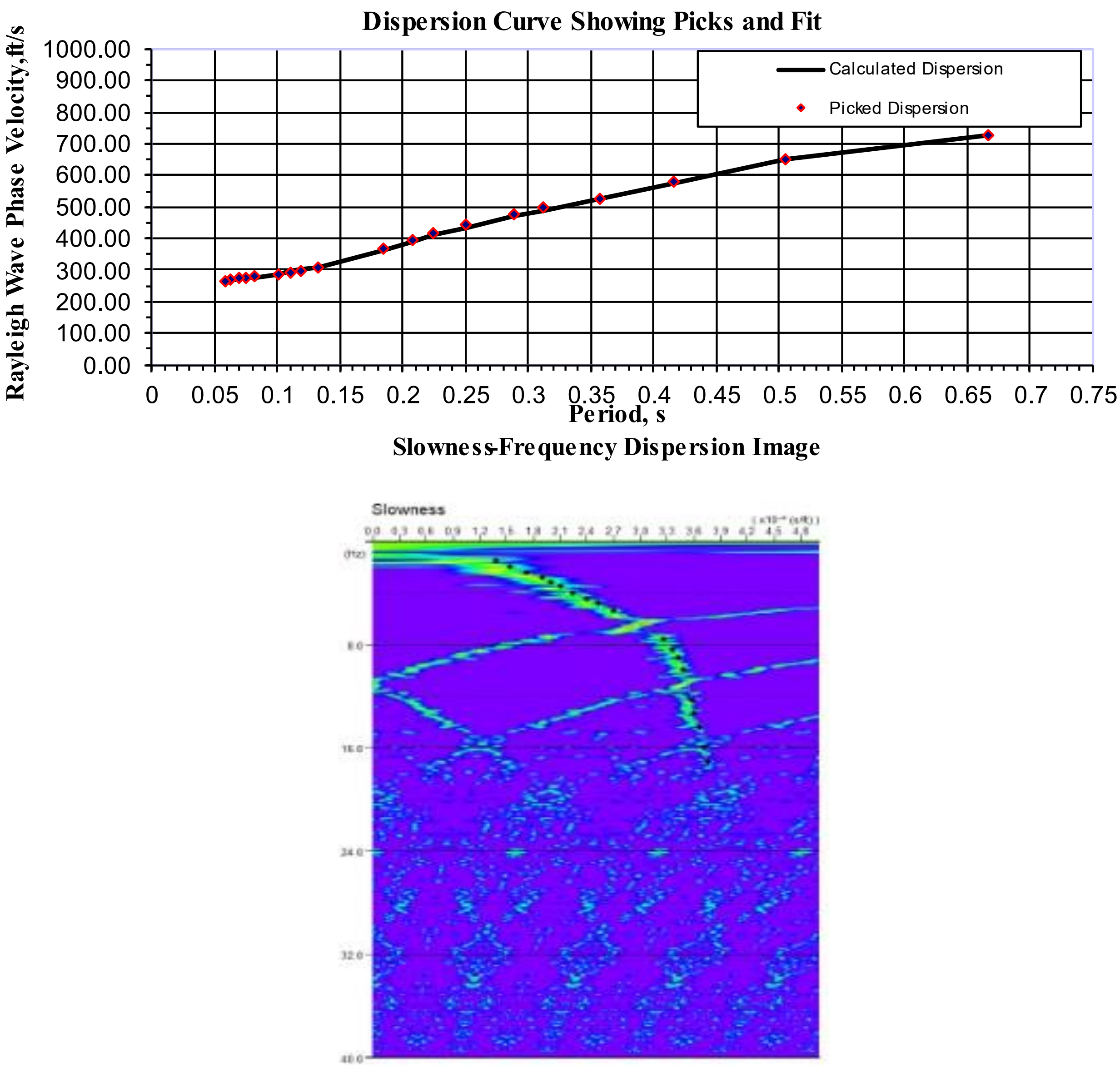

Figure 7-4: Dispersion Curve and Image Line 2A.

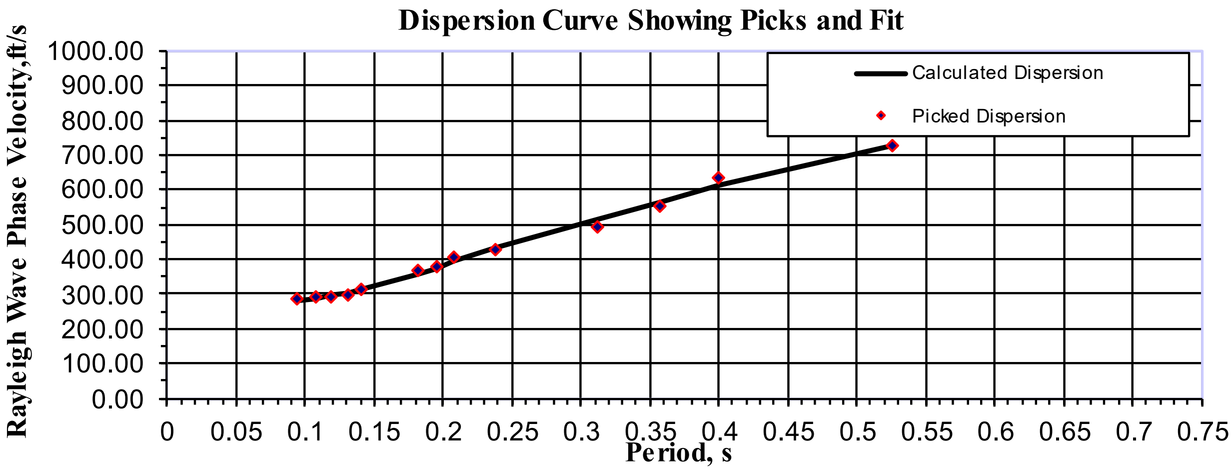

Slowness-Frequency Dispersion Image

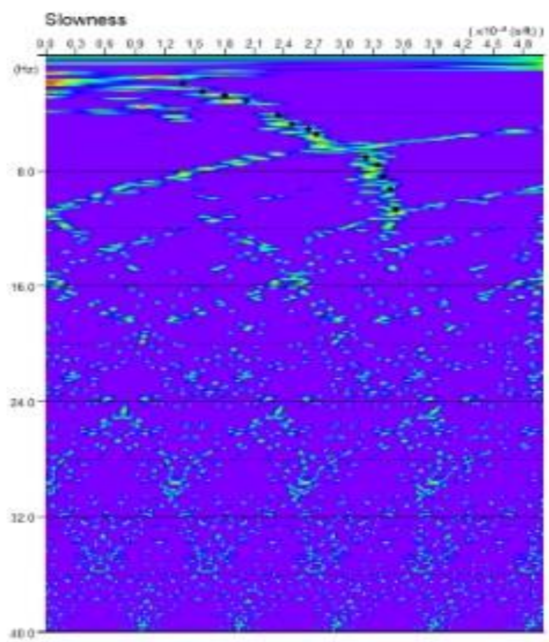

Figure 7-5: Dispersion Curve and Image Line 2B.

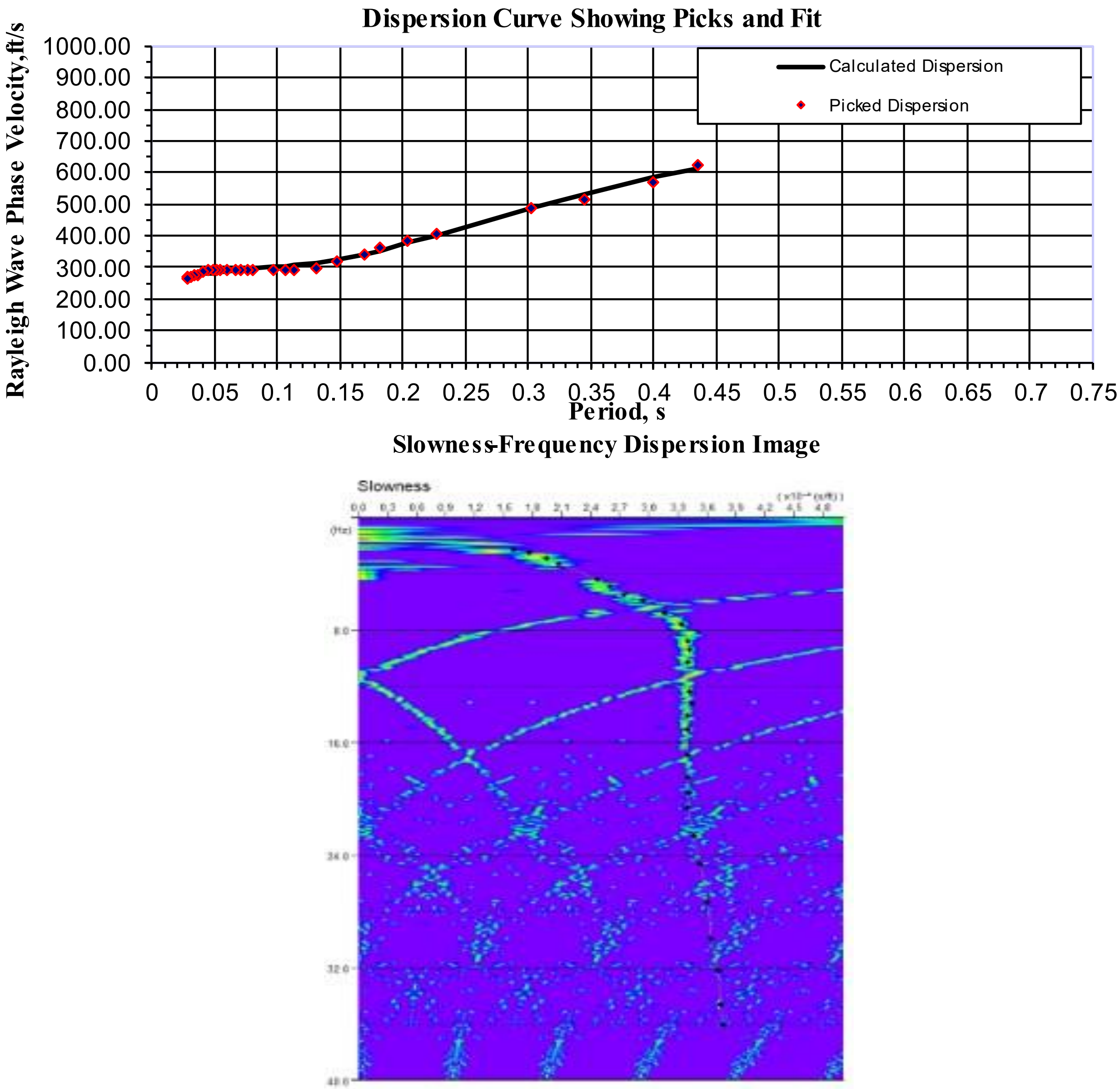

Figure 7-6: Dispersion Curve and Image Line 2D.

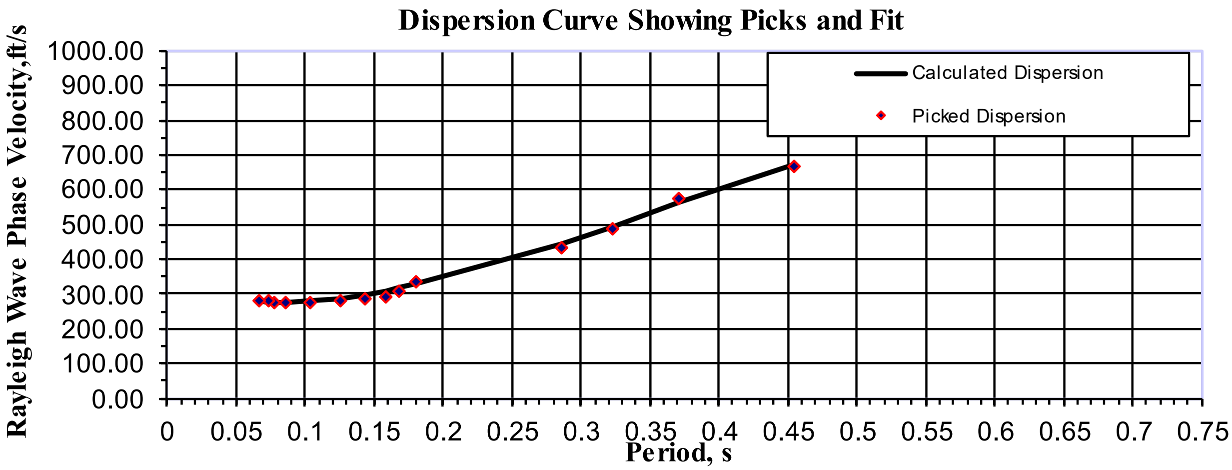

Slowness-Frequency Dispersion Image

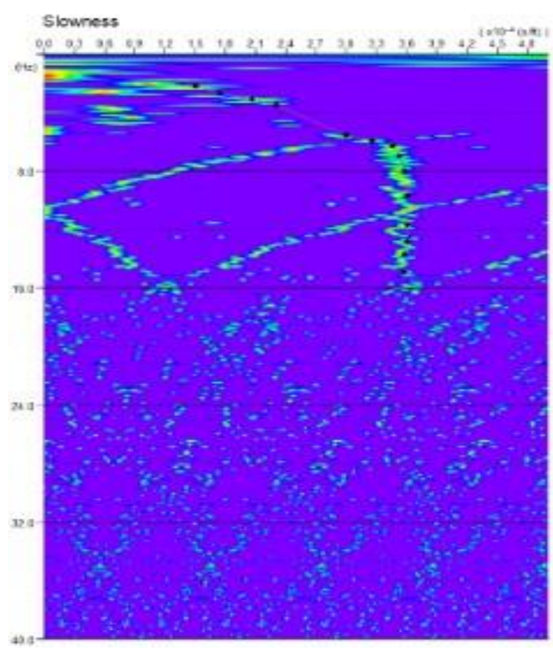

Figure 7-7: Dispersion Curve and Image Line 3.

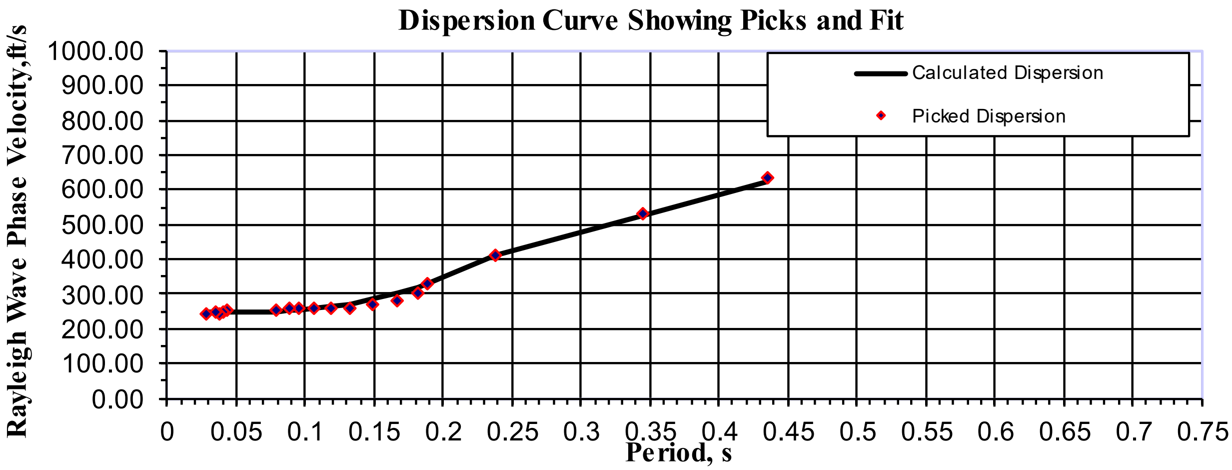

Slowness-Frequency Dispersion Image

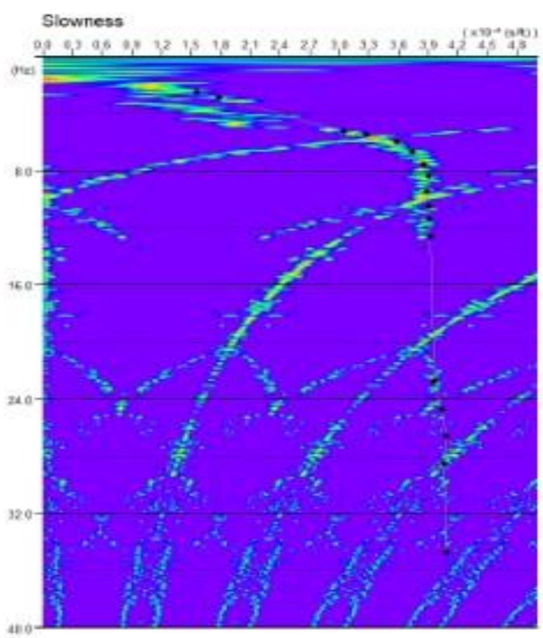

Figure 7-8: Dispersion Curve and Image Line 4A.

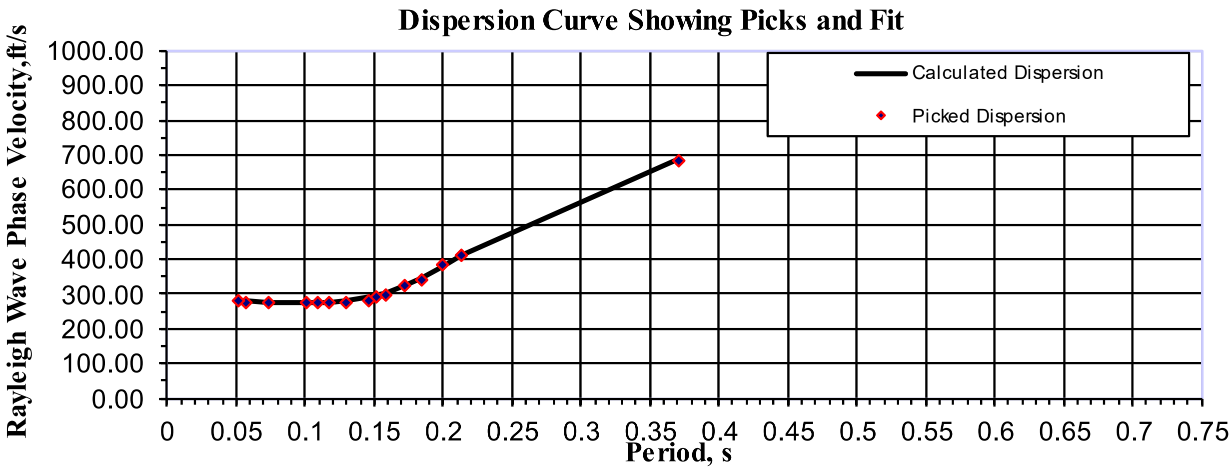

Slowness-Frequency Dispersion Image

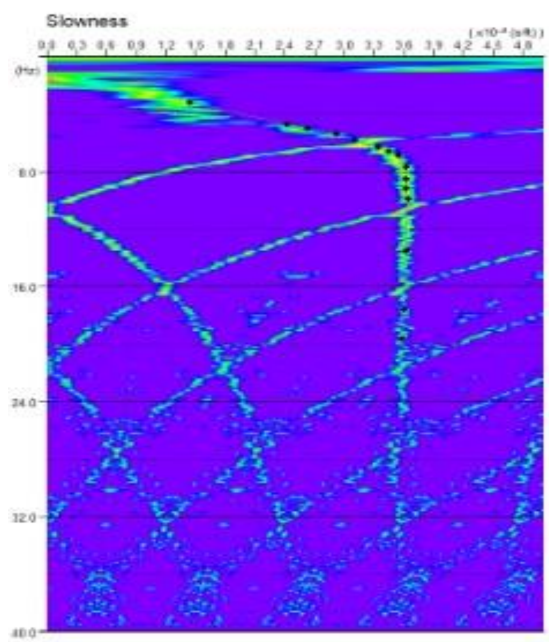

Figure 7-9: Dispersion Curve and Image Line 4B.

7.2 Spatial Variation of Ground Properties

The following paragraph discuss the significance of potential variation and distribution of features and what it implies.

Both vertical (stratigraphic) and horizontal variation in soil consistency should be expected that would trigger local variations in liquefaction potential. All of the sites, including the lateral spread area crossing US 95, and the ground oscillation features on the edge of the playa, were approximately at the distal end of a moderate-size alluvial wash from the Monte Cristo Range (shown on Figure 4-1). This wash both would recharge groundwater, provide younger deposition, and change the grain size of materials present near these particular sites. Further upstream than US 95, groundwater would expect to become deeper (due to the increasing gradient of the alluvial fan) and the sand deposit would be both coarser-grained and more energetic (with possible higher relative density). The lateral spread side near the base of the alluvial fan, and the ground oscillation feature would represent a transitional zone with differential deposition of increasingly fine-grained deposits with distance. It is possible that playa deposits further into Columbus Salt Marsh increase in plasticity and exceed the criteria for liquefiable behavior. Increased salinity could also result in partial cementation with salts further west into the playa.

Furthermore, for an active playa boundary, it would not be unexpected for interfingering of playa and more active alluvial deposition, such as from large flash-flood events from the adjacent desert washes. These would have the potential for sedimenting larger pockets of sand or more-liquefaction-susceptible materials, further into and be interbedded with more clayey playa deposits. This would certainly trigger the type of flake ground failures observed in the ground oscillation features. These layers might be thin enough that they would not be easily detected by shear-wave velocity measurements.

Ultimately, the analyses above point to the plausibility of liquefaction in causing lateral spread, sand boils, and ground oscillation at this site, however there is an absence of needed additional data to better quantify and understand the ground motions, soil properties with depth, and groundwater conditions to make a more complete assessment at this time.

Figures 7-10 to 7-15 present the two-dimensional velocity profiles obtained from the ReMi measurements.

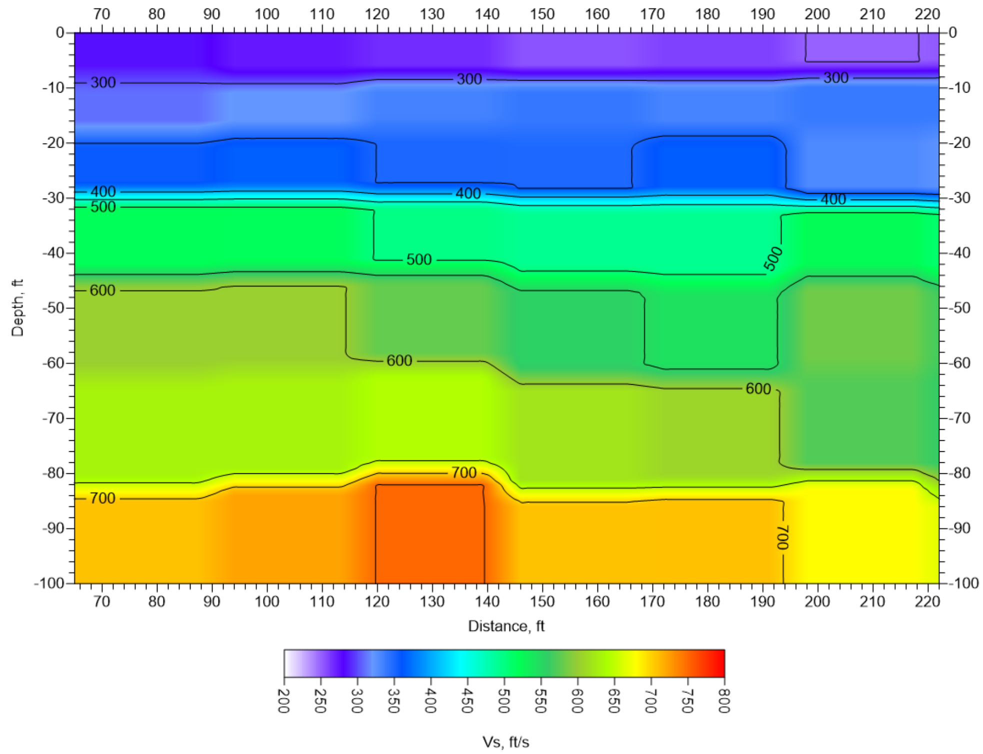

Figure 7-10: ReMI Results - Line-2A Two-Dimensional SWV Model – EW – Crosses ground failure zone from 80 to 180 feet.

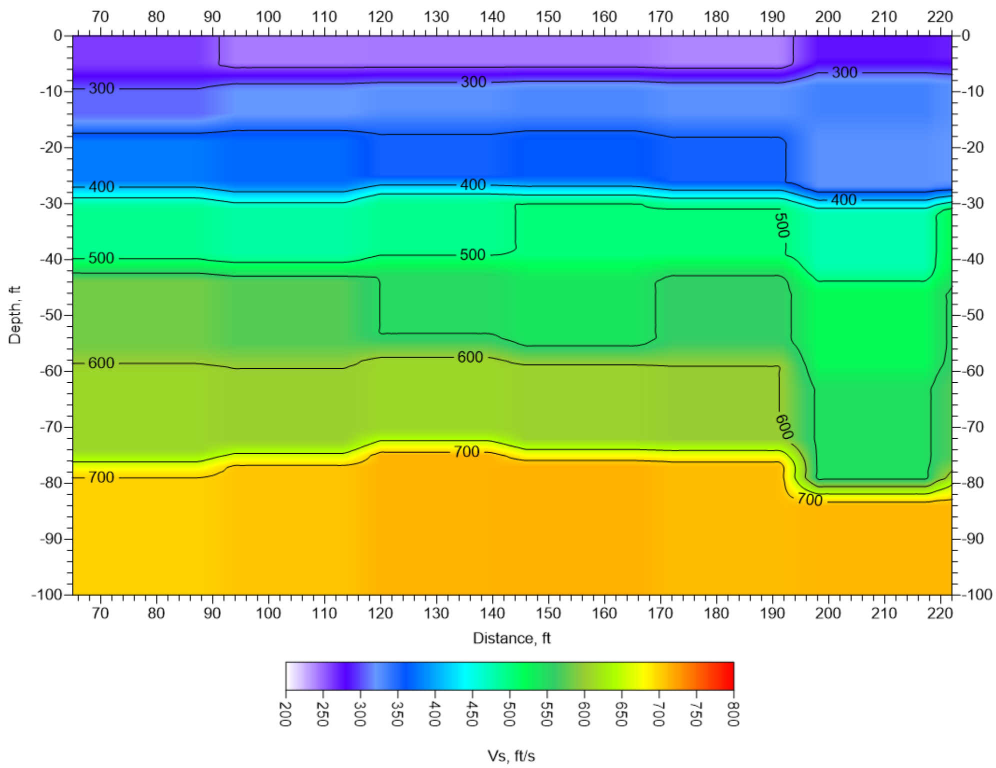

Figure 7-11: Line-2B Two-Dimensional SWV Model – NS – Crosses ground failure zone from 50 to 160 feet.

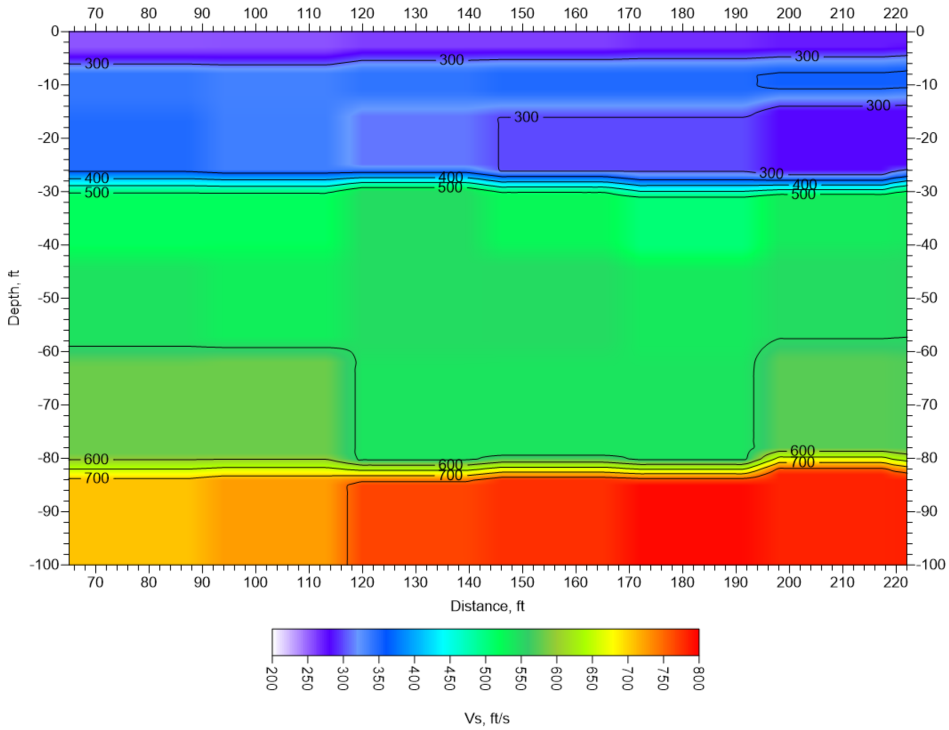

Figure 7-12: Line 2D Two-Dimensional SWV Model – Background ReMi survey not crossing failure.

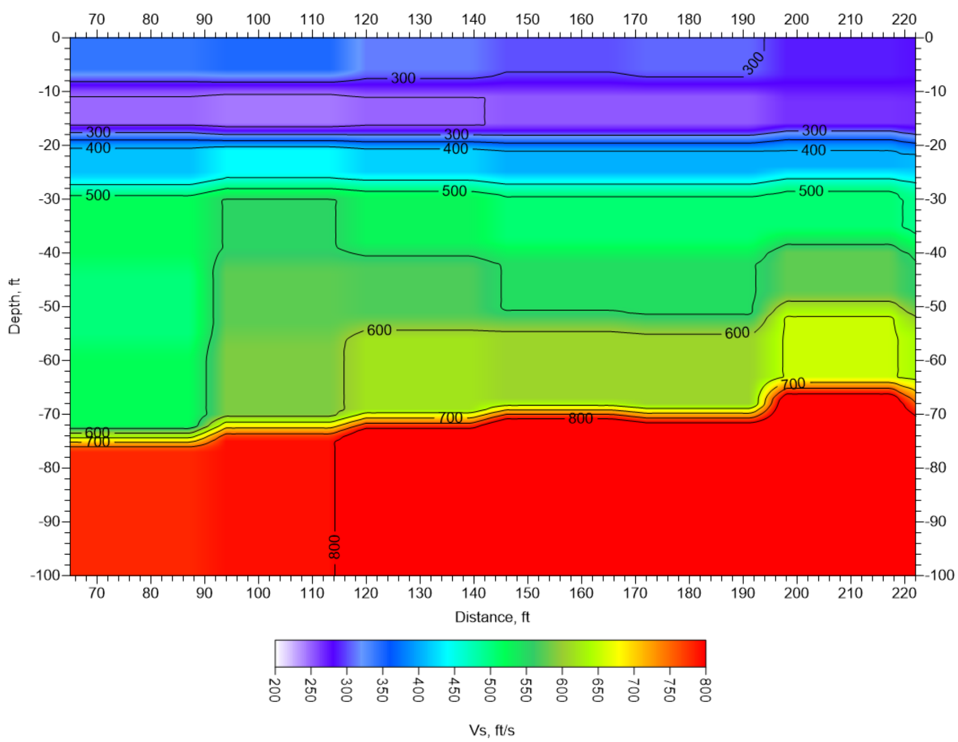

Figure 7-13: Line 3 Two-Dimensional SWV Model – Pausible Air-Ejecta Site, otherwise no Known Ground Deformation.

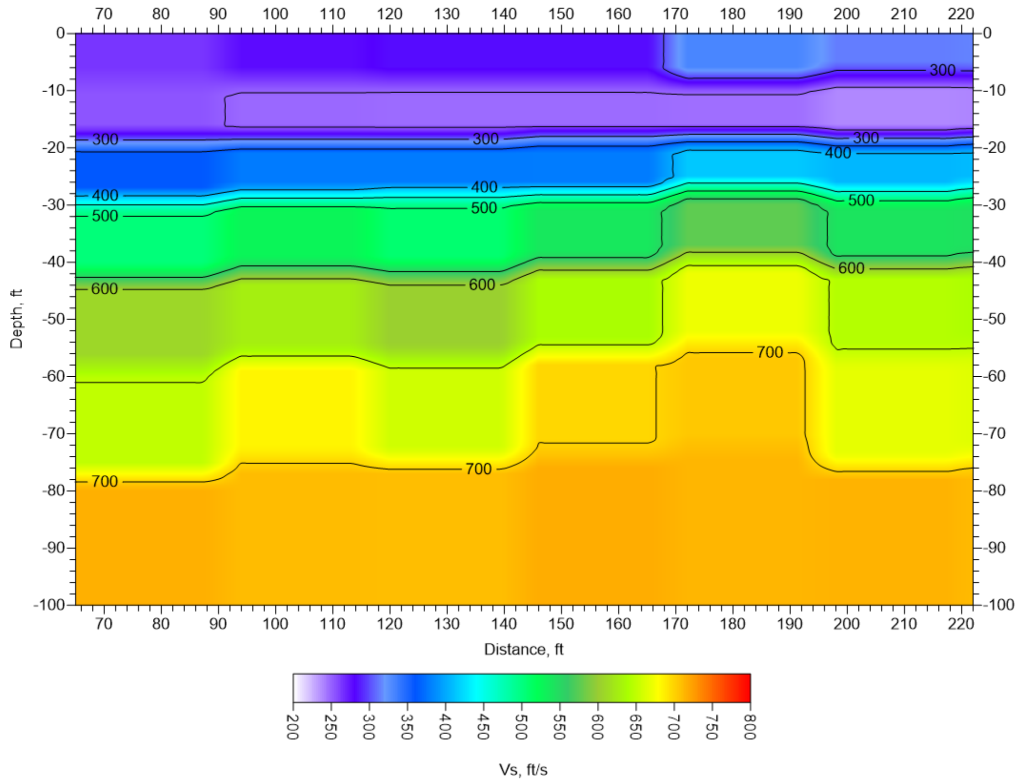

Figure 7-14: Line 4A Two-Dimensional SWV Model – Entirely Across Ground Failure Zone.

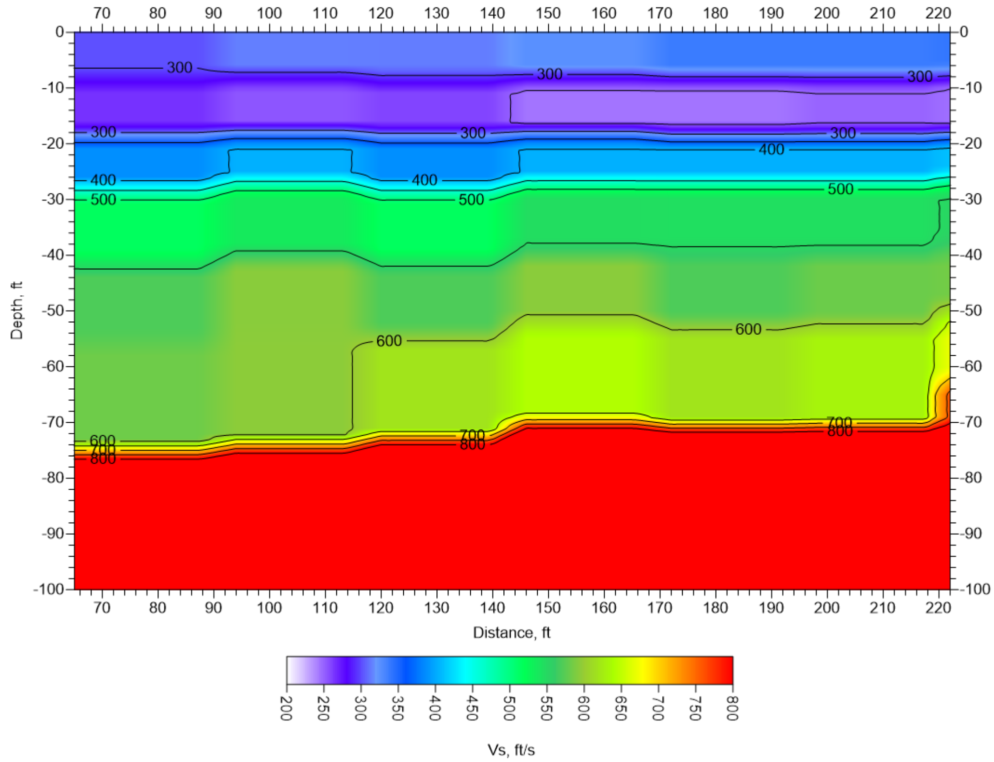

Figure 7-15: Line 4B Two-Dimensional SWV Model – 100 feet East and Outside of Ground Failure Zone.

7.3 Field Sampling

On June 9, 2020, the GEER team obtained soil samples for laboratory index testing to determine the physical properties and composition of surficial soils near some of the features of greatest interest within the Columbus Salt Marsh. A primary goal of this testing program is to elucidate whether the surficial soil crust was capable of preventing or permitting liquefaction manifestations (e.g., sand boils, settlement, fracturing) to propagate to the surface, assuming deeper liquefaction did indeed occur in this region. A total of 3 *Boil* samples were obtained within the low-lying area of the marsh, about 300 meters east of US 95. Additionally, 4 *GSS1* samples were obtained within the western edge of the fracture produced by the GSS1 ground displacement feature. The sample locations are mapped in Figure 7-16.

The *Boil* samples were taken at two different locations where the surficial soil compositions were believed to be distinct from one another. Samples *Boil #1 and #2* were taken within one of two slightly depressed (i.e., by ~1 to 2 inches) surface features that were lighter in color than the majority of the surrounding ground (Figure 7-17). A single test hole was used to obtain both samples, to a maximum depth of 2 feet. The surface of the depressed features prior to sampling felt highly compacted, and desiccation cracks were clearly visible. It is unclear whether these features were the result of liquefaction manifestations reaching the surface, or due to some other natural causes prior to the earthquake. Sample *Boil #3* was taken in an area where the ground surface felt "soft" and deformable when walked over. It was also adjacent to what appeared to be dissipation holes and cracks (Figure 7-18), which may have acted as outlets for excess pore pressures, following possible liquefaction of surficial soils under perched water conditions or deeper soils beneath the water table. No groundwater was visible during sampling.

The *GSS1* samples were taken at a single location along the western side of the GSS1 surface feature described in Chapter 4. Sample *GSS1 #1* was taken near the surface, about 3 feet away from the outside edge of the fracture (Figure 7-19a). Samples *GSS1 #2*, *#3* and *#4*, were taken within the already open fracture, down to a depth of about 5 feet (Figure 7-19b). Samples were only taken from soil that was freshly exposed during the excavation, either from the side walls of the excavation or from beneath the base of the current excavation level. No groundwater was visible during sampling.

GEER team members used a shovel to excavate down to the sample depths at each test location (Figure 7-20). Plastic "zip-lock" bags were used to store and label the samples immediately after obtaining them (Figure 7-20). These bags remained sealed until tested in the lab, in an attempt to retain the in-situ moisture conditions.

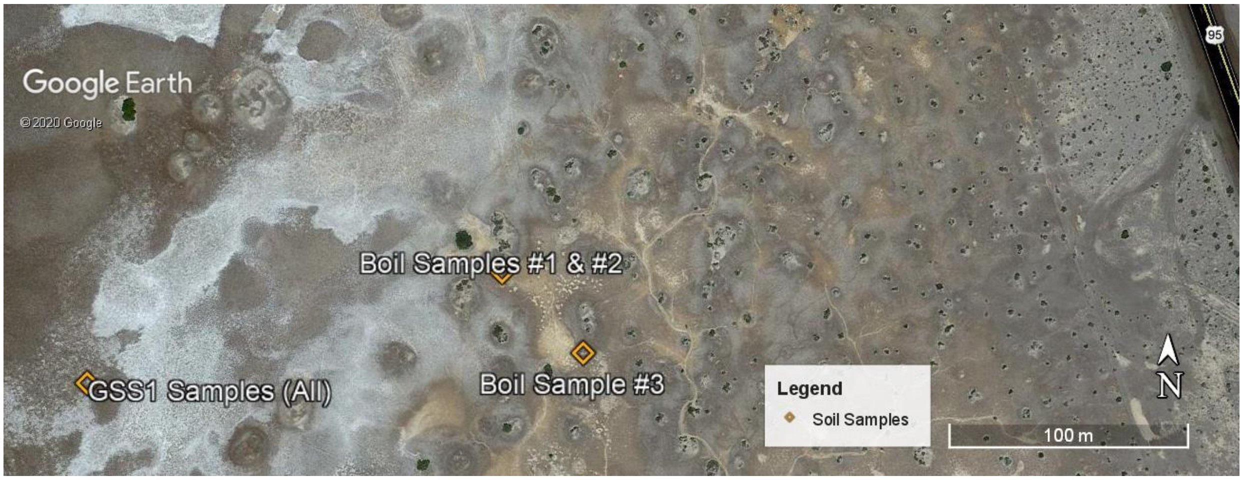

Figure 7-16: Map of soil sample locations (background image from Google Earth).

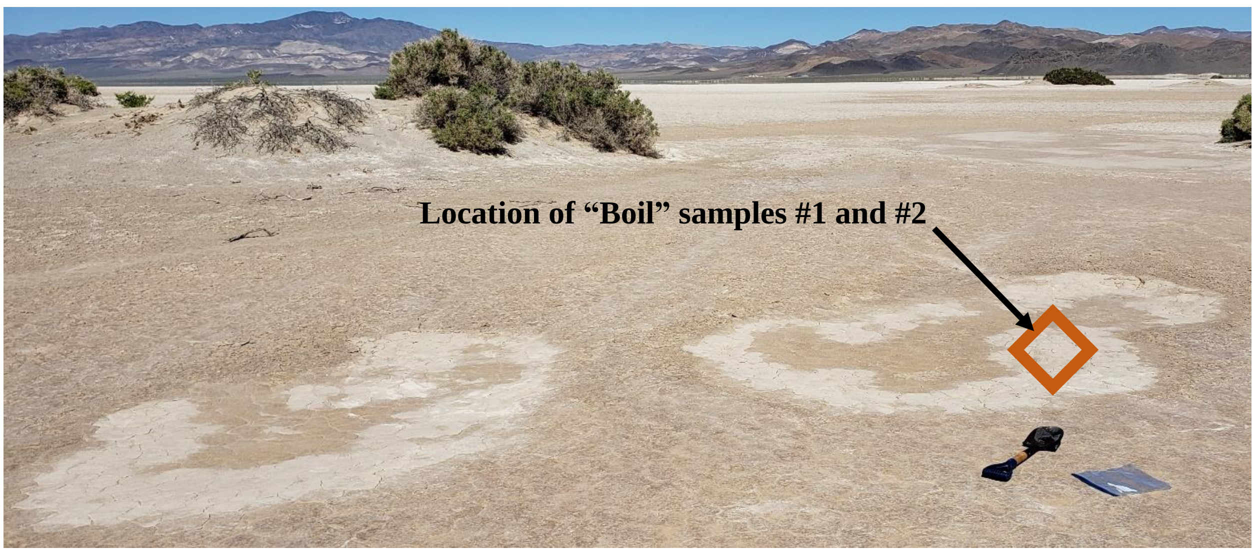

Figure 7-17: Locations of samples *Boil #1* and *#2* prior to sampling *(lat/long = 38.11204, -117.93291).*

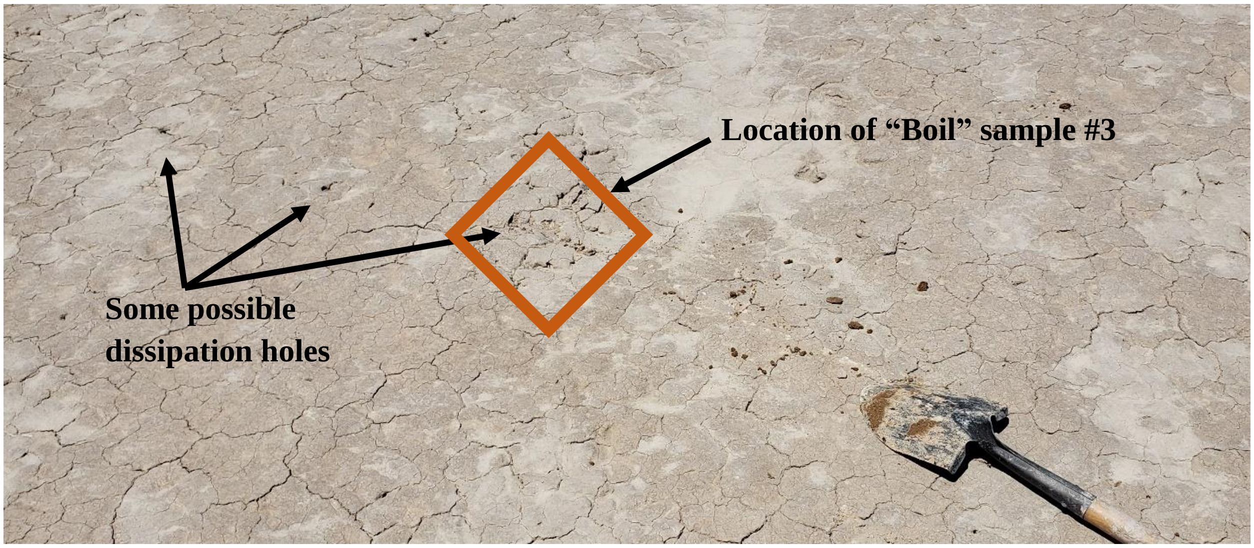

Figure 7-18: Location of sample *Boil #3* prior to sampling *(lat/long = 38.11174, -117.93252).*

(a)  (b) 

Figure 7-19: Locations during sampling of (a) Samples GSS1 #1 (lat/long = 38.11159, -117.93487), and (b) Samples GSS1 #2, #3, and #4 (lat/long = 38.11160, -117.93499).

7.4 Laboratory Testing and Results

A laboratory testing program was undertaken at the geotechnical engineering laboratory of the University of Nevada, Reno during the month following the GEER mission. For each of the 7 soil samples obtained, the following index tests were performed in accordance with applicable American Society for Testing and Materials (ASTM) standards:

- Sieve analysis with hydrometer (ASTM D422)
- Plasticity and liquid limit (ASTM D4318)

- Moisture content (ASTM D2216)

Figure 7-20: Obtaining and storing sample *GSS1 #2* in a moisture sealing plastic bag *(lat/long = 38.11161, -117.93488)*.

Based on the lab results, each sample was classified according to the Unified Soil Classification System (USCS; i.e., ASTM D2487) and the American Association of State Highway and Transportation Officials (AASHTO) soil classification system (i.e., ASTM D3282).

Table 7-1 summarizes some of the important results from the lab tests performed, which may assist in identifying the composition and consistency of the surficial soils. This information may also indicate the susceptibility of the surficial soils to liquefaction triggering, depending on saturation conditions at the time of the earthquake. The liquefaction susceptibility of these soil samples will be further discussed in Section 10 of this report. The processed lab data is included in Appendix B.

Table 7-1: Summary of laboratory index test results

Sample ID	Depth (inches)	Sample Location (lat/long)	USCS	AASHTO Class	Moisture Content (%)	Fines Content (%)	Plasticity Index
Ejecta #1	3 to 9	38.1120, -117.9329	CL-ML	A-4	13.9	81	4.5
Ejecta #2	19 to 24	38.1120, -117.9329	CL-ML	A-4	22.0	80	6.7
Ejecta #3	2 to 8	38.1117, -117.9325	ML	A-4	10.4	71	5.8
GSS1 #1	2 to 8	38.1116, -117.9349	CL-ML	A-4	2.7	79	8.8
GSS1 #2	60	38.1116, -117.9349	CL-ML	A-4	25	83	4
GSS1 #3	42	38.1116, -117.9349	CL-ML	A-4	24.2	65	2.2
GSS1 #4	30	38.1116, -117.9349	CL-ML	A-4	16.7	46	NP

8.0 Transportation Systems (Highways and Culverts)

The main transportation systems within the vicinity of the epicenter are US Highway 95 (US 95) and US State Route 6 (US 6). The epicenter is roughly 7 miles due north of the junction of US 95 and US 6 at Coaldale. In this section we briefly describe performance of the transportation systems and supporting structures (i.e. pavement, concrete box culverts and corrugated metal culverts) within the area of the epicenter through field observations gathered on June 8 and 9, 2020.

8.1 US 95 and US 6 Junction

The Nevada Department of Transportation (NDOT) maintains US 95 and US 6 within the region. Highway US 95 north of Coaldale experienced one large transverse fracture across the pavement. Multiple small ground surface ruptures were observed west of the highway embankment running parallel and into the adjacent to Columbus Marsh. At the time of the reconnaissance US 95 was closed for emergency repairs, therefore the ruptured pavement section was not physically observed by our team. The following photo in Figure 8-1, sourced from a local newspaper, documents the rupture across US 95 the morning of the event. At the time of emergency repairs, NDOT closed that section of US 95 and rerouted traffic using an alternate route through US 6. NDOT escorted our reconnaissance team along the closed portion of US 95 to conduct our field observations. No visible damage was observed on the alternate route on US 6. Figure 8-2 presents the transverse cracks observed parallel to the highway and trending into Columbus Marsh.

Figure 8-1: Transverse crack across US 95 the morning of the event, looking east towards Monte Cristo Range (courtesy of Reno Gazette Journal, May 22, 2020 online edition) (approx. Lat./Long. 38.11226, -117.9290).

Figure 8-2: Transverse cracks observed parallel of western embankment of US 95 and looking south toward Coaldale (Photo taken June 9th, 2020) (Lat./Long. 38.11226, -117.9290).

8.2 Box Culvert (M-137B)

Our team inspected a box culvert, identified by NDOT as M-137B, just north of the junction of US 95 and US 6 at Coaldale. Structure M-137B provides flow underneath US 95 from the Coaldale Wash and is roughly 6 miles south of the epicenter at NDOT milepost marker 95ES-85.52. Structure M-137B consists of a concrete buttress on either side of US 95 and included corrugated metal pipe serving as a conduit for drainage beneath the highway. The dimensions of the concrete buttresses on M-137B were approximately 5 feet in height and 25 feet wide (Figure 8-3). The corrugated conduits were observed to contain detritus from previous drainage events through the wash (Figure 8-4). The conduits were approximately 4.2 feet in diameter. Each concrete buttress wall was inspected for signs of distress. No damage was observed in the structure resulting from the May 15th event.

Figure 8-3: Western concrete buttress of NDOT Structure M-137B at Coaldale Wash (Lat./Long. 38.03281, -117.888).

Figure 8-4: Eastern concrete buttress of NDOT Structure M-137B at Coaldale Wash showing infilling of detritus from previous flow events (Lat./Long. 38.03269, -117.887).

Additional corrugated metal pipe culverts (CMP) were also observed crossing US 95 in several sections near the epicenter. Figure 8-5 presents a typical CMP near the epicenter. No signs of distress or damage was observed with these structures.

Figure 8-5: Corrugated Metal Pipe Culvert crossing US 95 north of Coaldale Wash and south of epicenter (Lat./Long. 38.0679, -117.908).

9.0 Industrial Facilities

The Monte Cristo Range Earthquake occurred in a remote location in Nevada, centered approximately 56 miles west of Tonopah, Nevada (population 2,500) and 40 miles southeast of Hawthorne, Nevada (population 3,300). We only observed two industrial facilities that may have been impacted by the event. Brief descriptions of the two facilities are presented below.

9.1 Candelaria Mine Site

Candelaria Mine is an open-pit silver mine that is not currently active. Reclamation of the site has been ongoing since 1998 when the mine dumps were re-contoured and seeded, and the heap leach piles were rinsed and seeded. The site is located 10 miles west of the epicenter (Figure 9-1).

Figure 9-1: Map showing observed industrial facilities.

We observed the mine dumps from the access road (a distance of about 1,000 ft) and did not see any signs of slope failure, settlement, or distress, see Figures 9-2 and 9-3.

(a)

(b)

Figure 9-2: Photos of Candelaria Mine Dump looking south from access road. No visible damage was noted. (Photos MJR09-01 and MJR09-02).

We also observed portions of the open pit high wall that were visible from near the access road (Figure 9-3). There were signs of shallow surface sloughing on the cut benches, but there was no indication that the sloughing was due to the earthquake.

Figure 9-3: Photo of Candelaria Mine open pit high wall looking South west from edge of pit. Photo GL16-1).

9.2 Mine Processing Plant

We also observed an old mine processing plant at the north end of the Columbus Salt Marsh (Figure 9-1) where a small laboratory is now set up where we were able to ask the sole employee about the event. The site inlcuded one permananet building (Figure 9-4), approximately 120 feet by 100 feet in plan view. The building was 2-stories tall and constructed with a combination of masonry block walls and metal. The employee reported that several small (less than 1-inch aperture) diagonal cracks were found radiating out from the top corners of the doors in the building. We were able to visually confirm the existence of the cracks, but we were not granted permission to enter the building to take photographs.

Figure 9-4: Buildings at the Mine Processing Plant. Photo looking south. (Photo GL29-1).

The site also included a partially built masonry block structure (Figure 9-5). The structure did have some damage, but it was not clear that the damage was caused by the earthquake.

Figure 9-5: Partially built masonry block building at the Mine Processing Plant. Photo looking west. (Photo GL29-4).

There were also 8 metal tanks approximately 50 to 60-feet in diameter and 15 feet high that were empty at the time of the earthquake. No damage was reported at the tanks.

The employee did report that the shaking was “very strong” and lasted about 10 seconds, and that items did fall from the shelves and out of cupboards. He also noted that the water supply line for the water tank ruptured during the earthquake.

10.0 Liquefaction Potential Assessment

Surface displacement features in and near Columbus Salt Marsh are believed to result from liquefaction. The results of shear-wave velocity surveys and laboratory testing were evaluated to assess the liquefaction potential in this section.

According to the Boore and Atkinson (2008) GMPE and the plot in Figure 5-2, it is suggested that, for the sites being approximately 9 km from the primary fault plane and potentially the earthquake epicenter, that the average predicted ground acceleration would be 0.2g and the range of possible ground accelerations (plus or minus one standard deviation, or 88% probability) would be 0.12g to 0.35g.

The depth of groundwater is not known in the Columbus Salt Marsh, but is assumed to be in the range of 3 to 4 m. Soils were moist (and shrinkage cracks generally absent) at about 1.0 m depth; moisture content was practically the same at 1.1 m and 1.5 m at 24% to 25% by dry weight, respectively. Groundwater level might be as shallow as 2 to 2.5 m depth, but we consider it more likely that there is a considerable fringe of capillary rise and a groundwater depth of at least 4 m would be reasonable. Mechanism of ground oscillation and lateral spread would generally suggest that a shallower failure plane would probably be more reasonable from the size and kinematics of small (30 m diameter) ground oscillation features identified on the playa, and for the migration of excess pore water in small sand boils.

Liquefaction potential can be assessed using shear-wave velocity for saturated granular soils in Youd et al (2001), using the general approach adopted by Andrus & Stokoe (2000). Curves were developed for clean sands, silty sands with 20% fines, and for silty sands with more than 35% fines. The liquefaction threshold for 35% fines or more was evaluated for the earthquake magnitude, potential ground accelerations, and assumed groundwater table at 4 m depth. The liquefaction threshold versus depth on Figure 10-1 can be compared to the shear wave profiles measured at the side to identify which depth intervals are potentially liquefiable.

The results of the liquefaction analysis suggest that at the average-minus-one-standard-deviation ground acceleration of 0.12g, the site soils would potentially have been close to incipient liquefaction between about 4 m and 8.5 m depth. For the predicted average peak ground acceleration, soil could have liquefied to far greater depth, in excess of 20 m. The results of liquefaction prediction above may not be applicable because low-stiffness clays on the site may potentially not be liquefiable based on the criteria below, and the method is not believed to be well-calibrated to materials with significantly greater than 35% fines. The response at the average ground conditions suggest that, with a slightly more powerful earthquake, significantly more ground failure might have been observed at the Columbus Salt Marsh site.

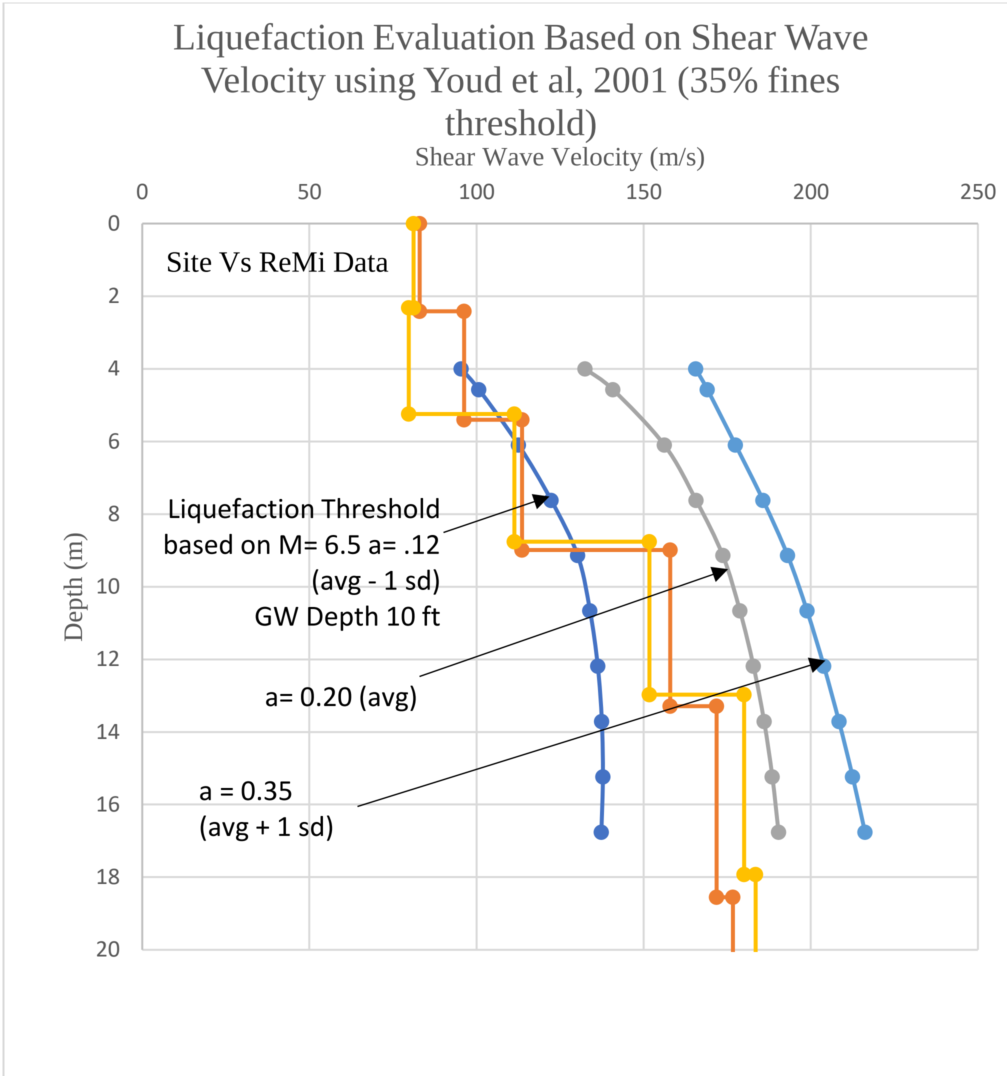

Figure 10-1: Liquefaction evaluation based on shear wave velocity using Youd et al. (2001) methodology.

Results of laboratory index testing, which were presented in Section 7 and Appendix B, indicate that most of the near surface materials sampled are potentially liquefiable based on the state-of-the art liquefaction prediction methods based on plasticity. Shallow soils were not sufficiently saturated to liquefy, but the stabilization of water content at 24% to 25% at 1.1 to 1.5 m depth suggests soils were nearly fully-saturated at and below that depth. Furthermore, the liquid limit at 1.5 m depth was 28%. With respect to various classification criteria,

- Soils classified as SC, SM, ML or CL with fines (percent finer than 0.005 mm < 15%, LL< 35 and WC >0.90 LL will be susceptible to liquefaction per Youd et al 2001. The second and third criteria are met by all site sample but some of the samples, particularly from the hand-dug test pit at GSS1, had closer to 20% to 30% smaller than 0.005 mm particle size based on hydrometer testing. The criteria for percent passing 0.005 mm was based on "Chinese liquefaction criteria" is generally not credited by more modern researchers.

- Soils classified as SC, SM, ML or CL with low plasticity fines (LL< 37 and PI< 12) and WC >0.80 LL will be susceptible to liquefaction per Seed et al 2003. The WC/LL ratio for the 1.5 m depth sample in the ground oscillation crack was 25/28 = 89%. All three criteria are valid for the site soils.
- Soils classified as SC, SM, ML or CL with low plasticity fines (LL< 37 and PI< 7) and WC >0.80 LL will be susceptible to liquefaction per Idriss and Boulanger 2004. All three criteria are valid for the site soils, except that the deepest sample from the GSS1 hand-dug test pit had PI = 8.
- For soils with a liquid limit of less than 30, Idriss and Boulanger (2008) recommends that the transition from liquefiable behavior to clay-like behavior would be at about PI = 3 to 7. Using this criteria, two of the six samples tested were more in the clay-behavior range than in sand-like (liquefaction) behavior range, including the samples at 1.1 and 1.5 m depth samples adjacent to ground displacement feature GSS1. The range of fine-grained behavior overall suggests that some of the playa silts may be non-liquefiable, but some may fall within the liquefiable range.

The following paragraph discuss the significance of potential variation and distribution of features and what it implies.

Both vertical (stratigraphic) and horizontal variation in soil consistency should be expected that would trigger local variations in liquefaction potential. All of the sites, including the lateral spread area crossing US 95, and the ground oscillation features on the edge of the playa, were approximately at the distal end of a moderate-size alluvial wash from the Monte Cristo Range (shown on Figure 4-1). This wash would both recharge groundwater, and provide younger deposition, and change the grain size of materials present near these particular sites. Further upstream than US 95, groundwater would expect to become deeper (due to the increasing gradient of the alluvial fan) and sand deposit would be both coarser-grained and more energetic (with possible higher relative density). The lateral spread site near the base of the alluvial fan, and the ground oscillation feature would represent a transitional zone with differential deposition of increasingly fine-grained deposits with distance. It is possible that playa deposits further into Columbus Salt Marsh increase in plasticity and exceed the criteria for liquefiable behavior. Increased salinity could also result in partial cementation with salts further west into the playa.

Furthermore, for an active playa boundary, it would not be unexpected for interfingering of playa and more active alluvial deposition, such as from large flash-flood events from the adjacent desert washes. These would have the potential for sedimenting larger pockets of sand or more-liquefaction-susceptible materials, further into and be interbedded with clayier playa deposits. This would certainly trigger the type of flake ground failures observed in the ground oscillation features. These layers might be thin enough that they would not be easily detected by shear-wave velocity measurements.

Ultimately, the analyses above point to the plausibility of liquefaction in causing lateral spread, sand boils, and ground oscillation at this site, however there is an absence of needed additional data to better quantify and understand the ground motions, soil properties with depth, and groundwater conditions to make a more complete assessment at this time.

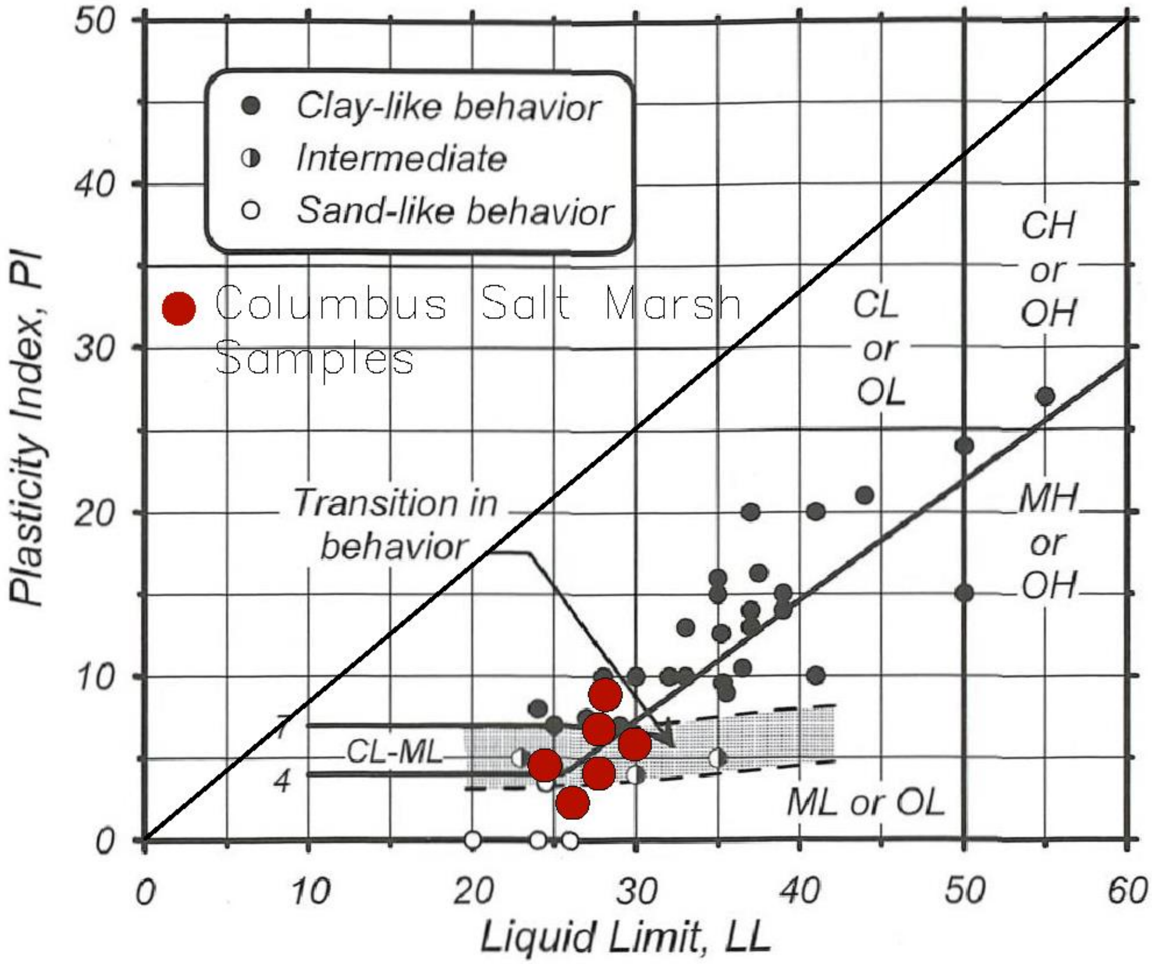

Figure 10-2: Fine-grained liquefaction criteria recommended by Idriss and Boulanger (2008).

11.0 References

1. Albers, J.P., and Stewart, J.H., 1972, Geology and Mineral Deposits of Esmeralda County, Nevada, Nevada Bureau of Mines and Geology, Bulletin 78.
2. Andrus, R. D., & Stokoe II, K. H. (2000). Liquefaction resistance of soils from shear-wave velocity. *Journal of Geotechnical and Geoenvironmental Engineering*, *126*(11), 1015-1025.
3. CESMD, 2020, Center for Engineering Strong Motion Data, website accessed 24 June 2020, https://www.strongmotioncenter.org/index.html
4. CESMD, 2020, Center for Engineering Strong Motion Data, website accessed 24 June 2020, https://www.strongmotioncenter.org/index.html
5. dePolo, Craig M. (2014). Historical earthquakes in Nevada; Nevada Bureau of Mines and Geology (NBMG), accessed 6/24/2020, from NBMG web site: http://www.nbmg.unr.edu/nhmpc/Presentations/Earthquake_Hazard_Presentations/NDEM_dePolo_1Oct14.pdf
6. Elliot, A., Pickering, A., and Hatem, A. (May 26, 2020). Preliminary Field Report: 05.15.20 M6.5 Monte Cristo Range Earthquake, NV. United States Geological Survey.
7. Idriss, I. M., & Boulanger, R. W. (2008). *Soil liquefaction during earthquakes*. Earthquake Engineering Research Institute.
8. IRIS, 2020. Mww 6.5 Nevada Event Page, Incorporated Research Institutions for Seismology (IRIS). http://ds.iris.edu/ds/nodes/dmc/tools/event/11230644, last accessed 2019-07-03.
9. Koehler, Richard D. (2020). *Rapid Response to the M6.5 Monte Cristo Mountains Earthquake, The Largest Earthquake in Nevada in 65 Years*. Presented through Nevada Bureau of Mines and Geology (NBMG) Geological Society of Nevada Zoom Lecture, 6/16/2020.
10. Louie, John, 2001, Faster, Better: Shear-Wave Velocity to 100 Meters Depth from Refraction Microtremor Arrays, Bulletin of the Siesmological Society of America, Vol 91 No. 2, April 2001.
11. Moeller, S.A., 1986, Geology and Mineralization in the Candelaria Mining District, Mineral County, Nevada, in Bulk Mineable Precious Metal Deposits of the Western United States, Symposium Proceedings, Geological Society of Nevada.
12. Nevada Bureau of Mines and Geology (NBMG), 2020. Monte Cristo range earthquake – May 15th, 2020, 4:03 am PDT, accessed 6/20/2020, from NBMG web site: http://www.nbmg.unr.edu/Geohazards/Earthquakes/MonteCristoRangeEQ.html
13. Nevada Bureau of Mines and Geology (NBMG), 2020. Monte Cristo range earthquake – May 15th, 2020, 4:03 am PDT, accessed 6/20/2020, from NBMG web site: http://www.nbmg.unr.edu/Geohazards/Earthquakes/MonteCristoRangeEQ.html
14. Nevada Division of Water Resources, 2020, Well Log Database, website accessed 20 June, 2020, http://water.nv.gov/WellLogQuery.aspx

15. Newman, R.L., Clark, A., Trabant, C.M., Karstens, R., Hutko, A.R., Casey, R.E., Ahern, T.K., 2013. Wilber 3: A Python-Django Web Application For Acquiring Large-scale Event-oriented Seismic Data. December. http://ds.iris.edu/wilber3/find_stations/11230644, last accessed 2020-07-03.
16. Oldow, J.S., Katopody, D.T., Kerstetter, S.R., and Mueller, N.J., 2016, Regional Setting, Geometry, and Structure of the Northern Fish Lake Valley Basin, 48 pages, dated 15 August.
17. Stewart, J.H., and Carlson, J.E., 1978, Geologic Map of Nevada, USGS Open File Report 03-66, prepared by the United States Geological Survey in cooperation with the Nevada Bureau of Mines and Geology, scale 1:500,000
18. Stewart, J.H., Kelleher, P.C., and Zorich, E.A., 1994, Geologic map of the Monte Cristo Range area, Esmeralda and Mineral Counties, Nevada: U.S. Geological Survey, Miscellaneous Field Studies Map MF-2260, scale 1:62,500.
19. United State Geological Survey (USGS), 2020a, M6.5 - Monte Cristo Range, NV earthquake, accessed 6/20/2020, from USGS web site: https://earthquake.usgs.gov/earthquakes/eventpage/nn00725272/executive
20. United States Geological Survey (USGS), 2020b, Quaternary Fault and Fold Database, website accessed 25 June 2020, https://earthquake.usgs.gov/hazards/qfaults
21. United States Geological Survey (USGS), 2020c,Advanced National Seismic System (ANSS) Comprehensive Earthquake Catalog (ComCat), website accessed 25 June 2020, https://earthquake.usgs.gov/earthquakes/search/Earthquake
22. University of Nevada, Reno (UNR), (2020). Monte Cristo earthquake fault still active with 6,500 aftershocks, dated 6/1 2020, accessed 6/20/20, from UNR: https://www.unr.edu/nevada-today/news/2020/monte-cristo-earthquake
23. Wesnousky, S.G., 2005, Active Faulting in the Walker Lane, published in Tectonics, Vol. 24, 35 pages, dated 16 June.
24. Westwater Resources, 2020, Columbus Basin Lithium Brine Project, website accessed 20 June, 2020, https://www.westwaterresources.net/projects/lithium/columbus-basin
25. Worden, C.B., E. M. Thompson, M. Hearne, and D.J. Wald (2020). ShakeMap Manual Online: technical manual, user's guide, and software guide, U. S. Geological Survey. http://usgs.github.io/shakemap/. DOI: https://doi.org/10.5066/F7D21VPQ.
26. Worden, C.B., E. M. Thompson, M. Hearne, and D.J. Wald (2020). ShakeMap Manual Online: technical manual, user's guide, and software guide, U. S. Geological Survey. http://usgs.github.io/shakemap/. DOI: https://doi.org/10.5066/F7D21VPQ.
27. Youd, T. L., & Idriss, I. M. (2001). Liquefaction resistance of soils: summary report from the 1996 NCEER and 1998 NCEER/NSF workshops on evaluation of liquefaction resistance of soils. *Journal of Geotechnical and Geoenvironmental Engineering*, *127*(4), 297-313.

Appendix A:

Processed Ground Motion Plots of Nearby Recording Stations

NNLHV, 2020MAY15, HNE

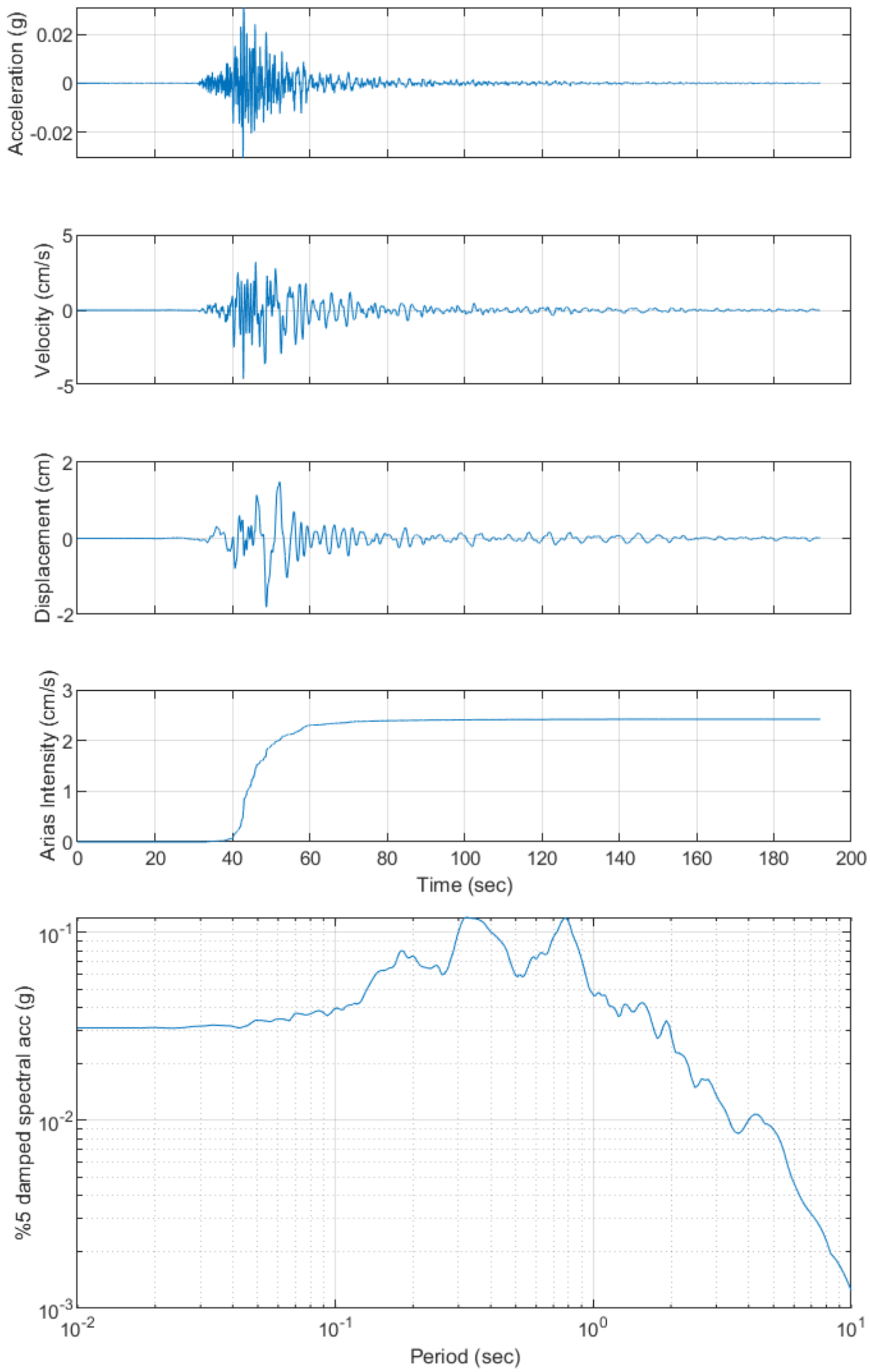

NNLHV, 2020MAY15, HNN

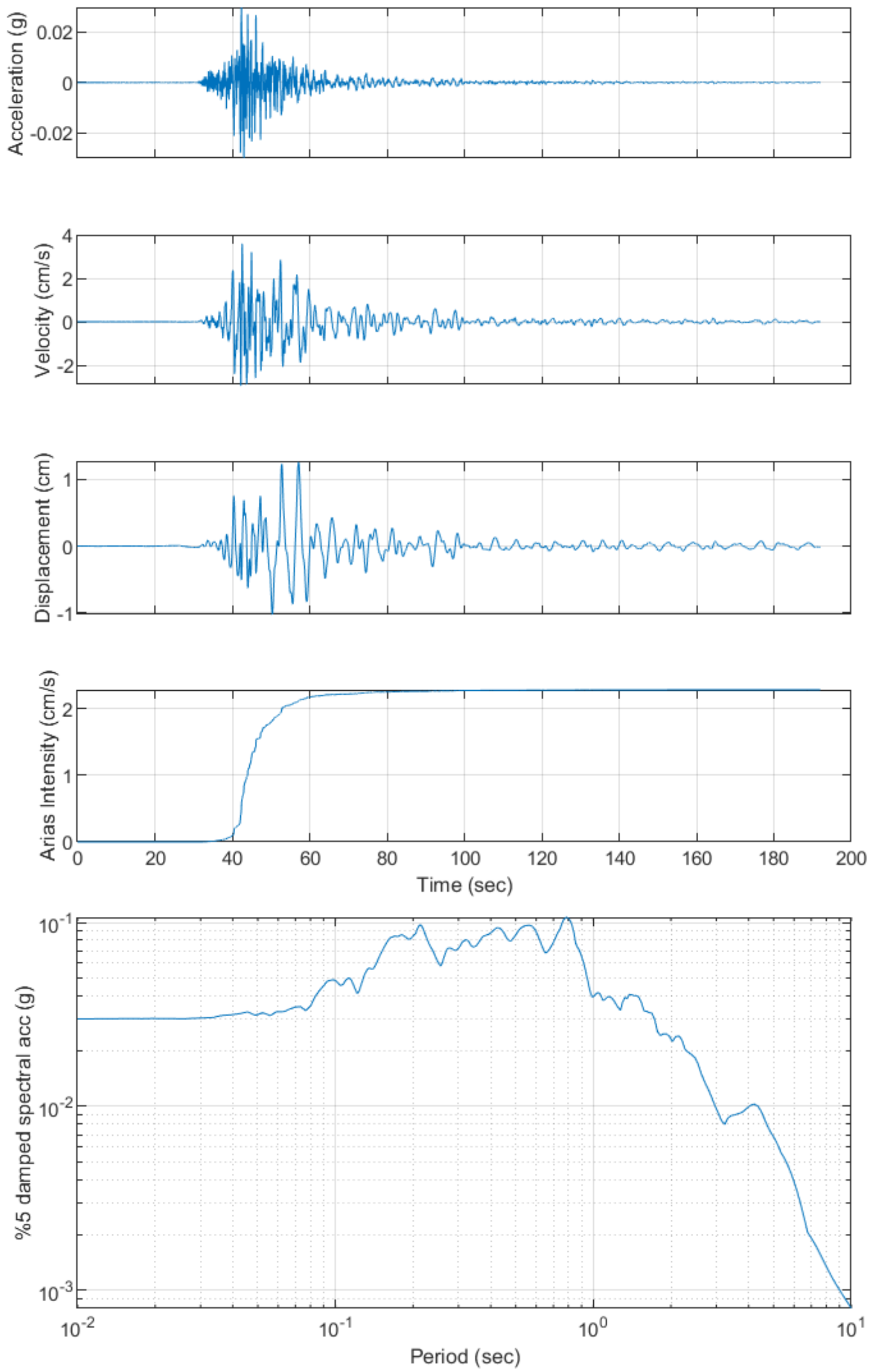

NNLHV, 2020MAY15, HNZ

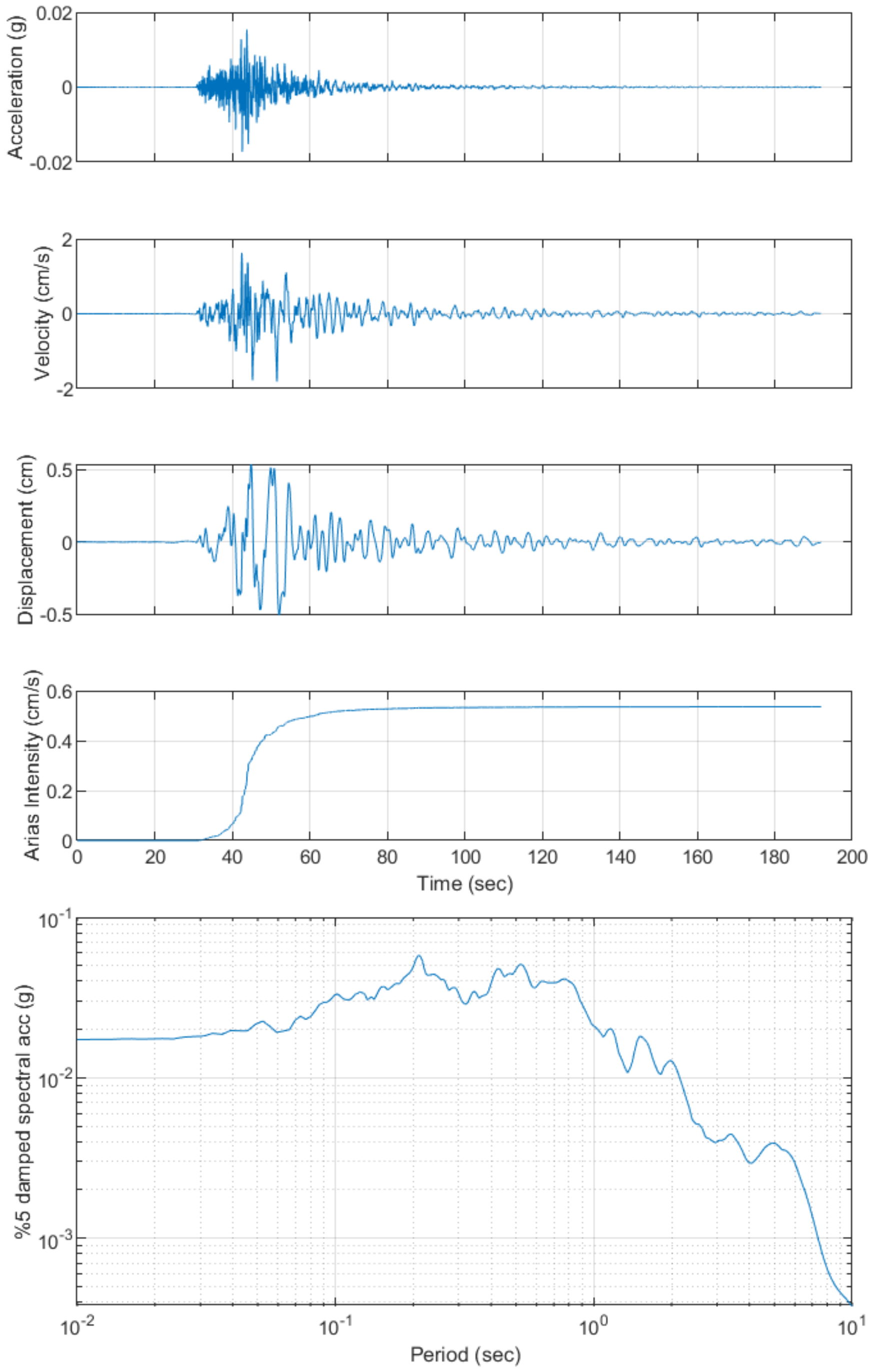

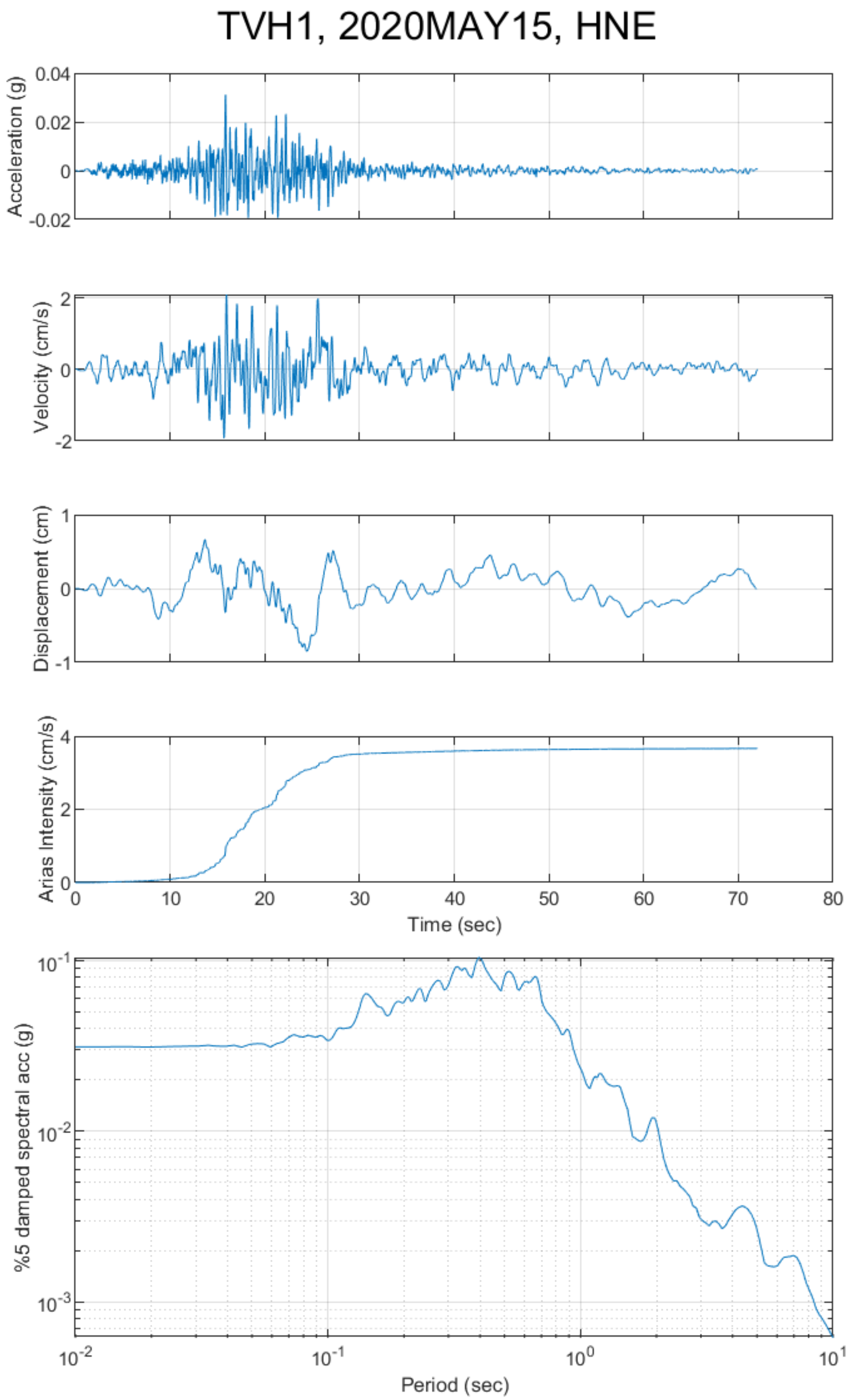
TVH1, 2020MAY15, HNE
Acceleration (g)
Velocity (cm/s)
Displacement (cm)
Arias Intensity (cm/s)
Time (sec)
%5 damped spectral acc (g)
Period (sec)

TVH1, 2020MAY15, HNN

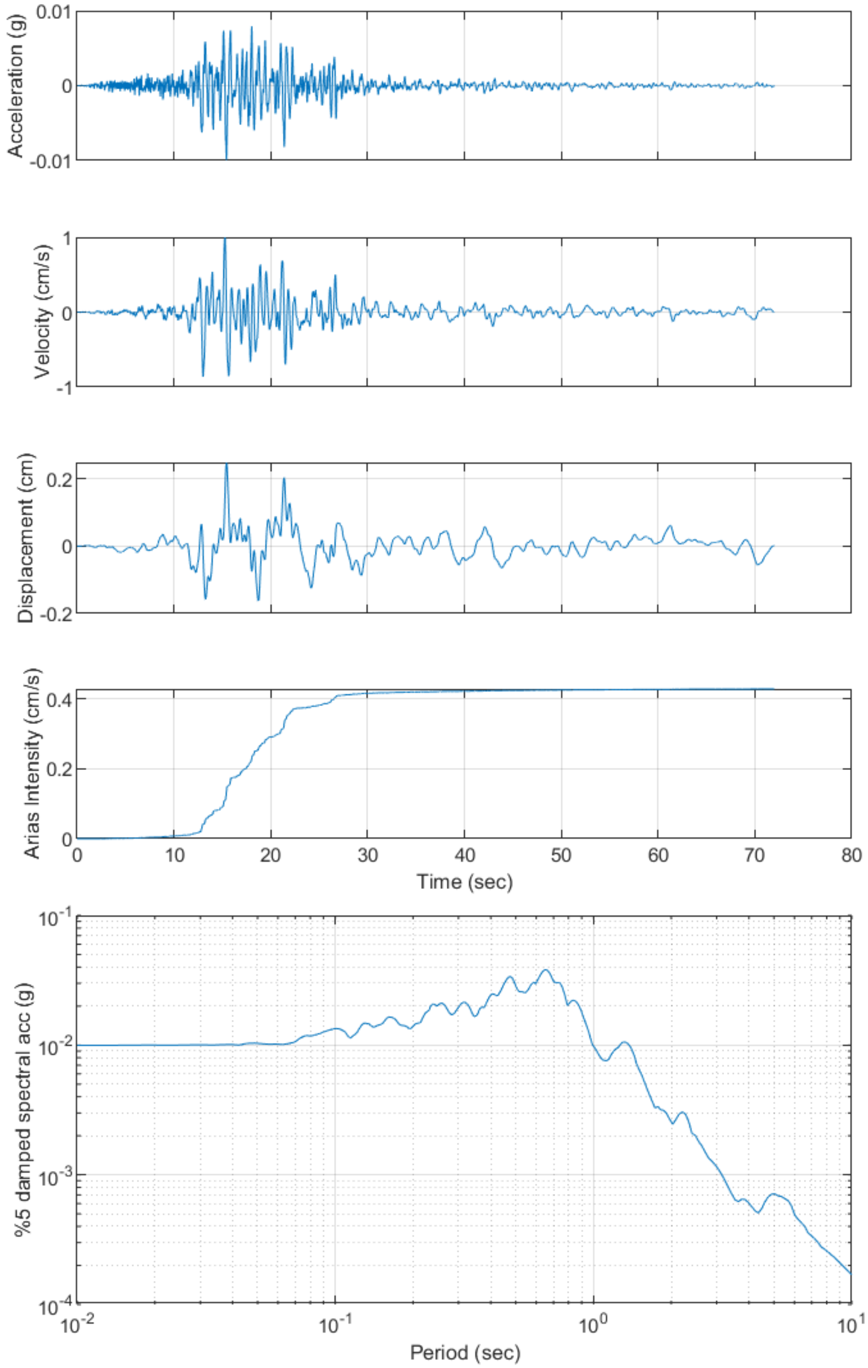

TVH1, 2020MAY15, HNZ

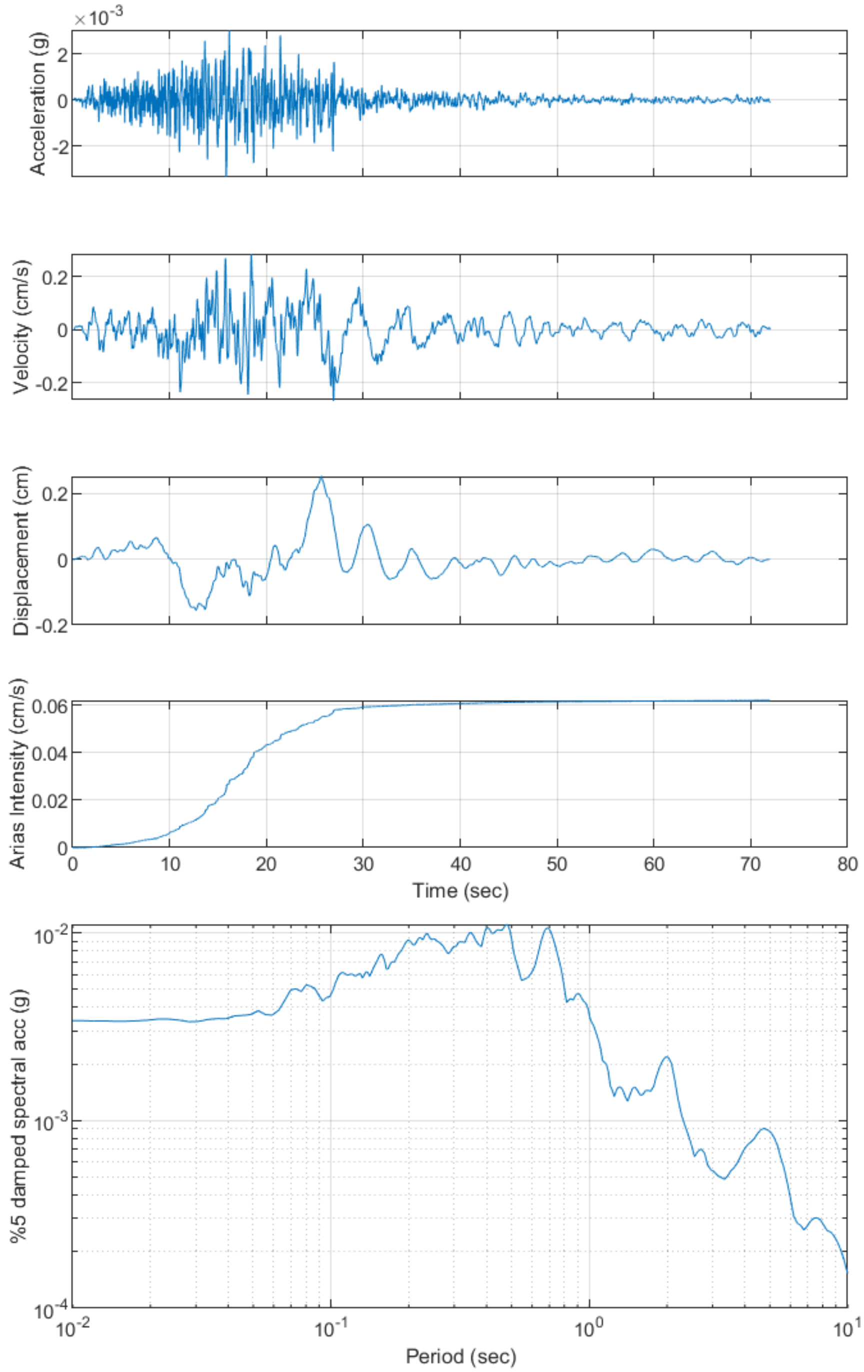

CE54428, 2020MAY15, 90deg

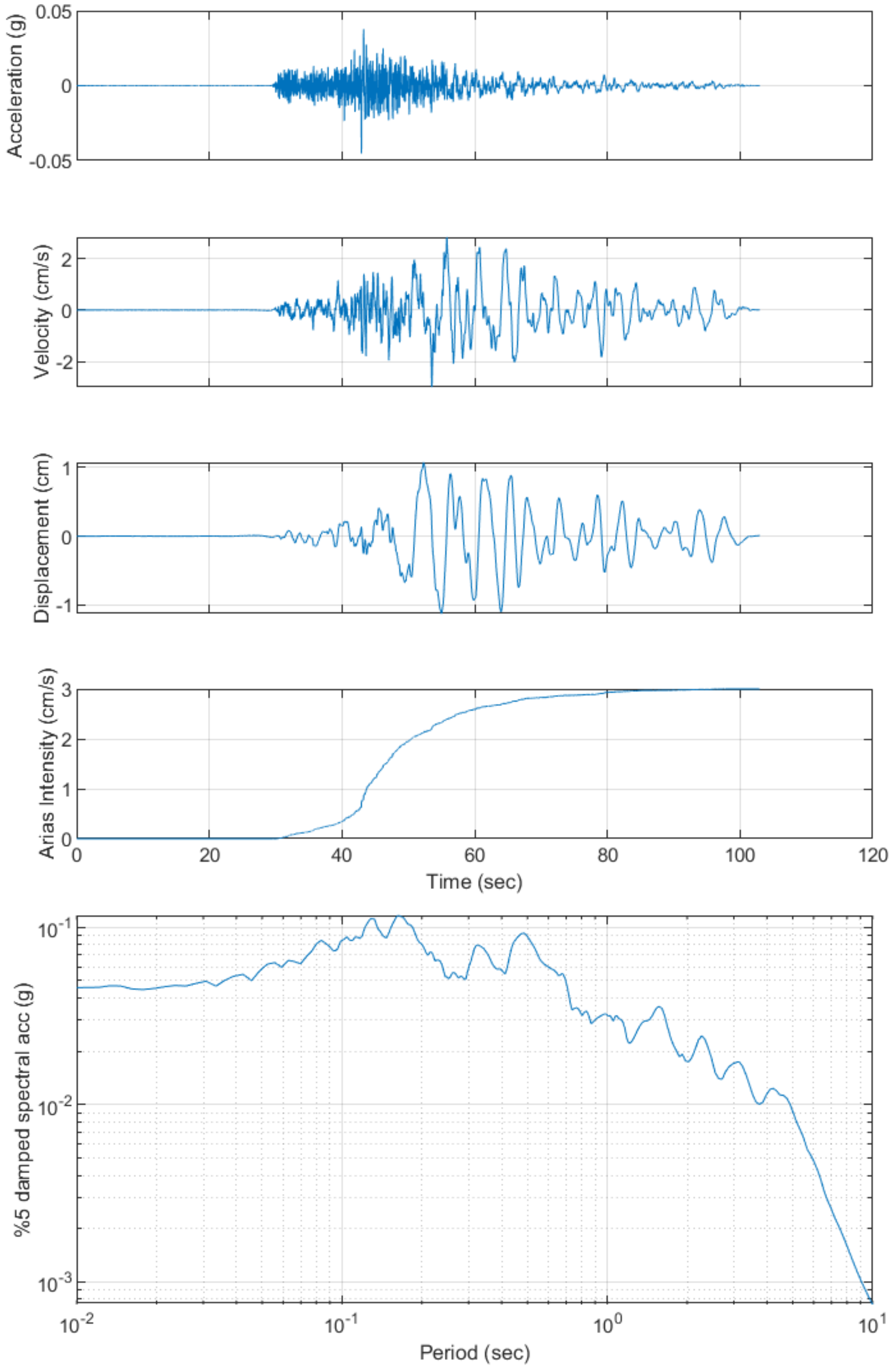

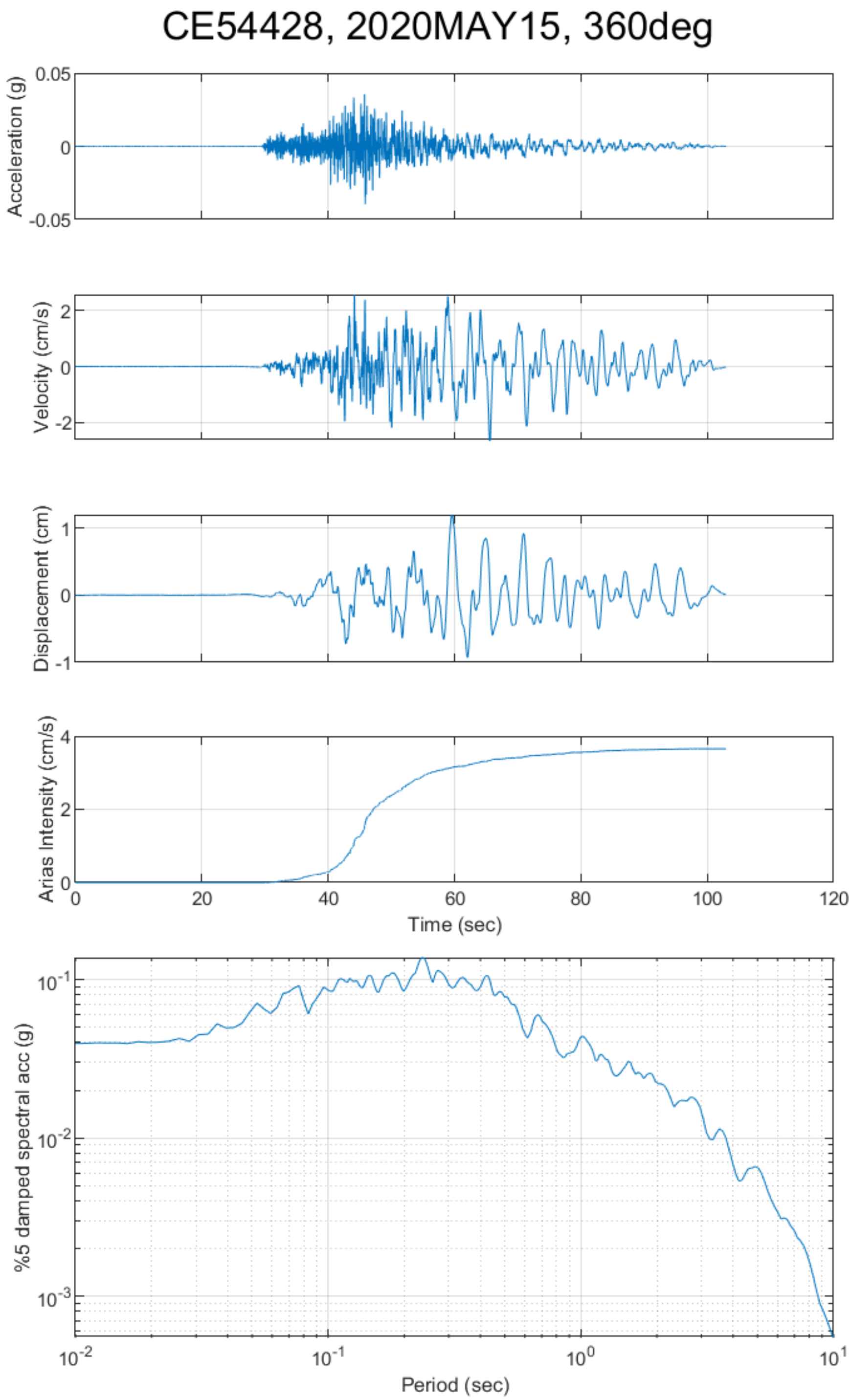
CE54428, 2020MAY15, 360deg
Acceleration (g)
Velocity (cm/s)
Displacement (cm)
Arias Intensity (cm/s)
Time (sec)
%5 damped spectral acc (g)
Period (sec)

CE54428, 2020MAY15, UP

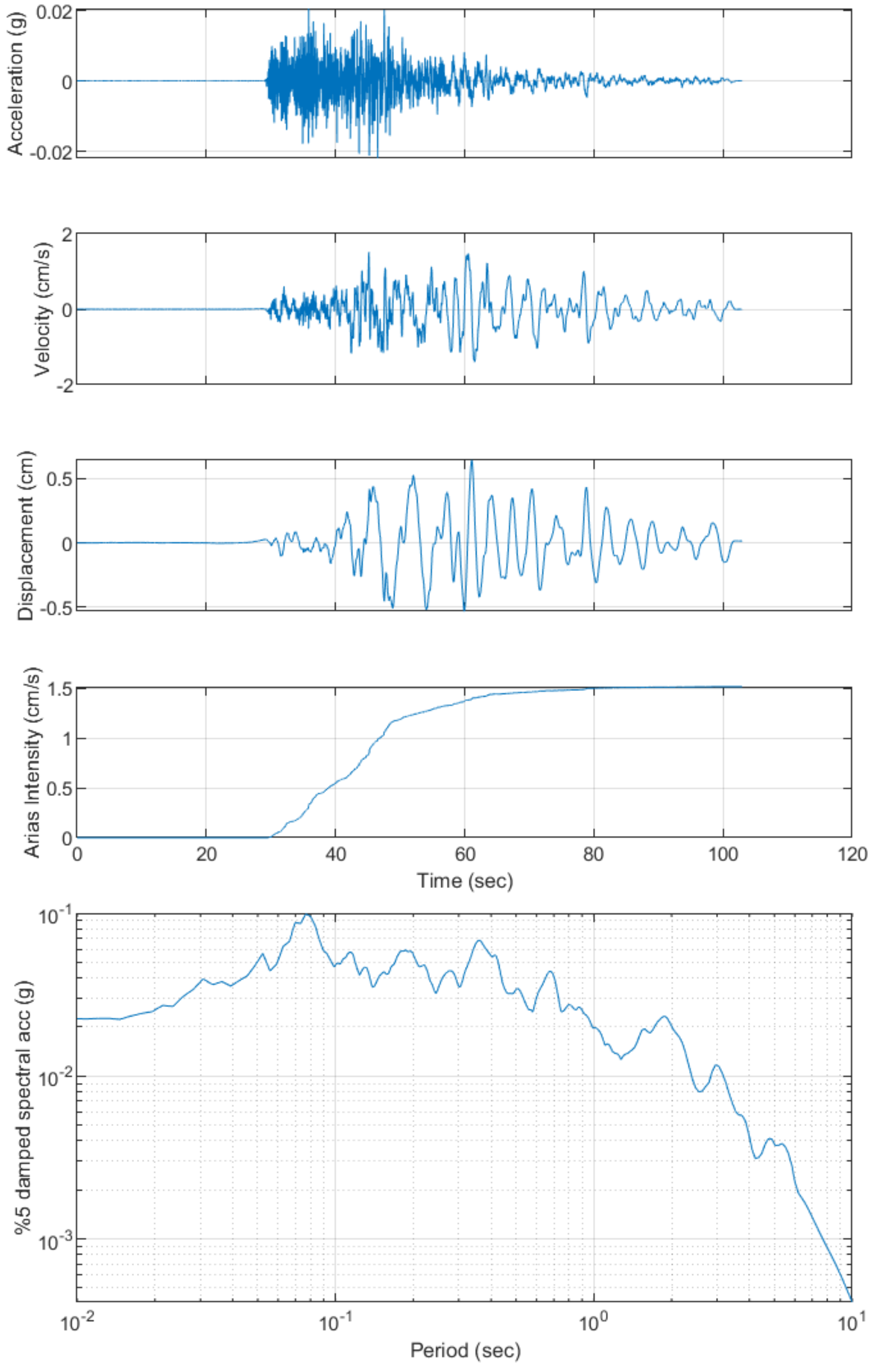

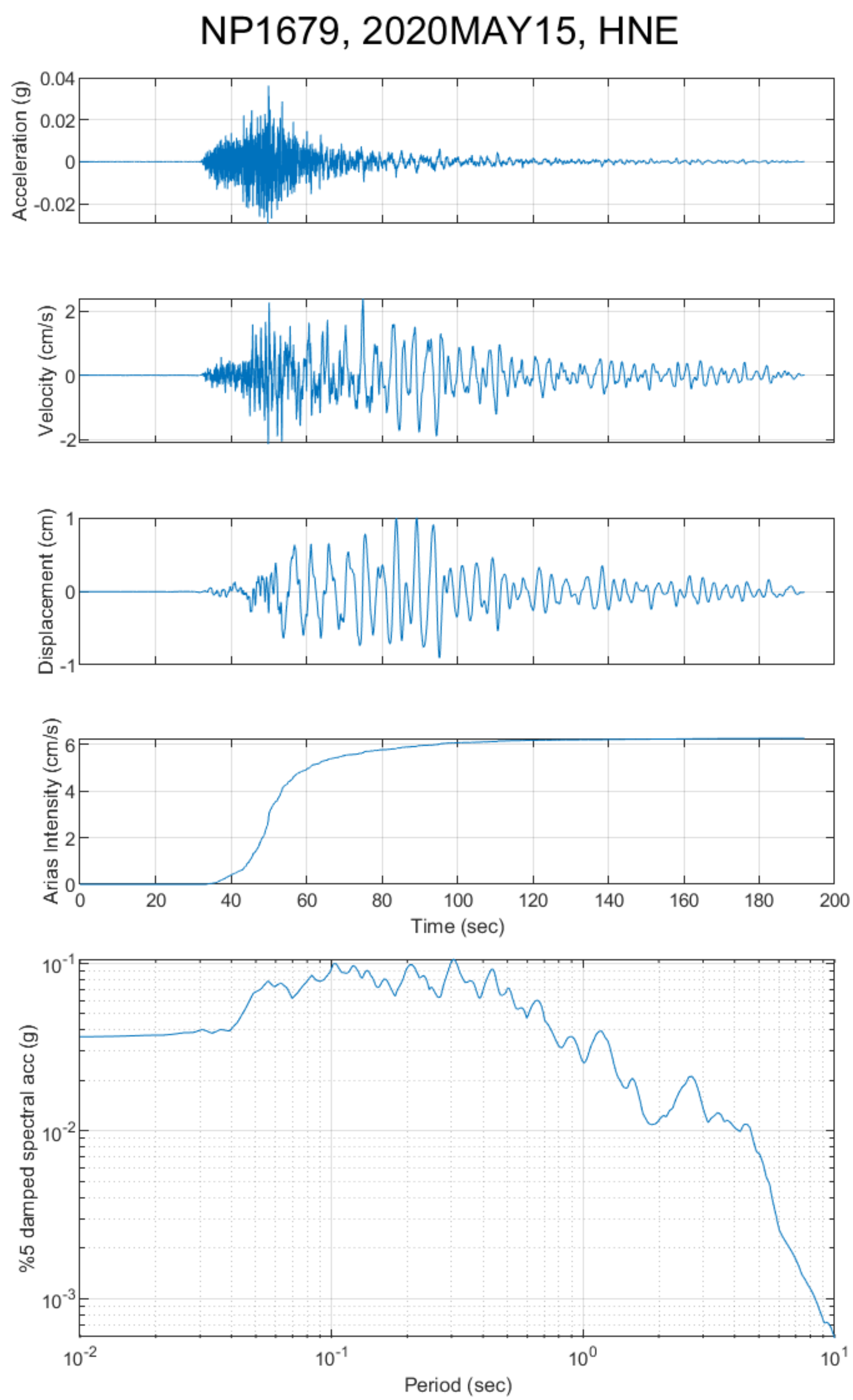

NP1679, 2020MAY15, HNE
Acceleration (g)
0.04
0.02
0
-0.02
Velocity (cm/s)
2
0
-2
Displacement (cm)
1
0
-1
Arias Intensity (cm/s)
6
4
2
0
0
20
40
60
80
100
120
140
160
180
200
Time (sec)
%5 damped spectral acc (g)
10^{-1}
10^{-2}
10^{-3}
10^{-2}
10^{-1}
10^{0}
10^{1}
Period (sec)

NP1679, 2020MAY15, HNN

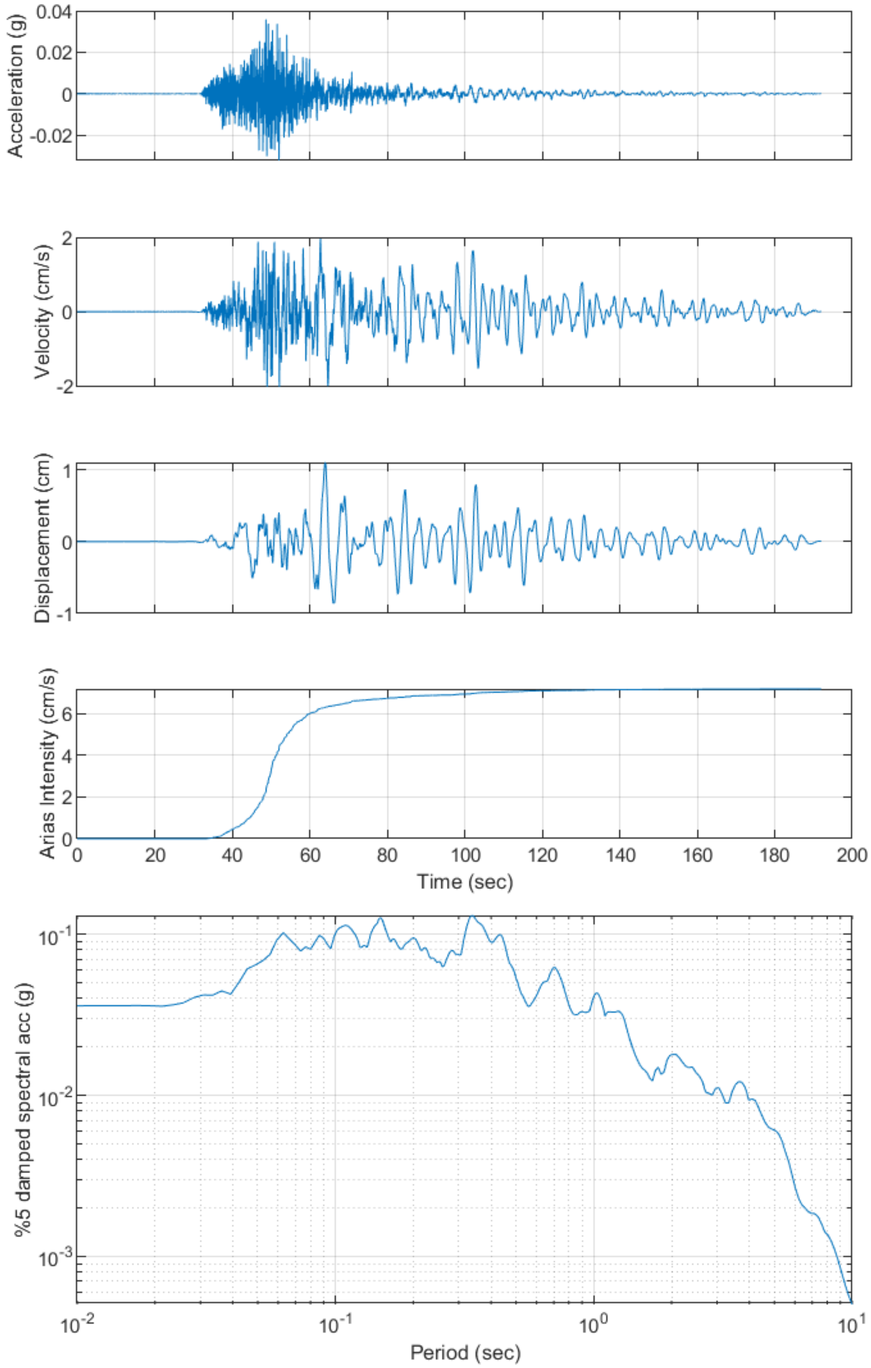

NP1679, 2020MAY15, HNZ

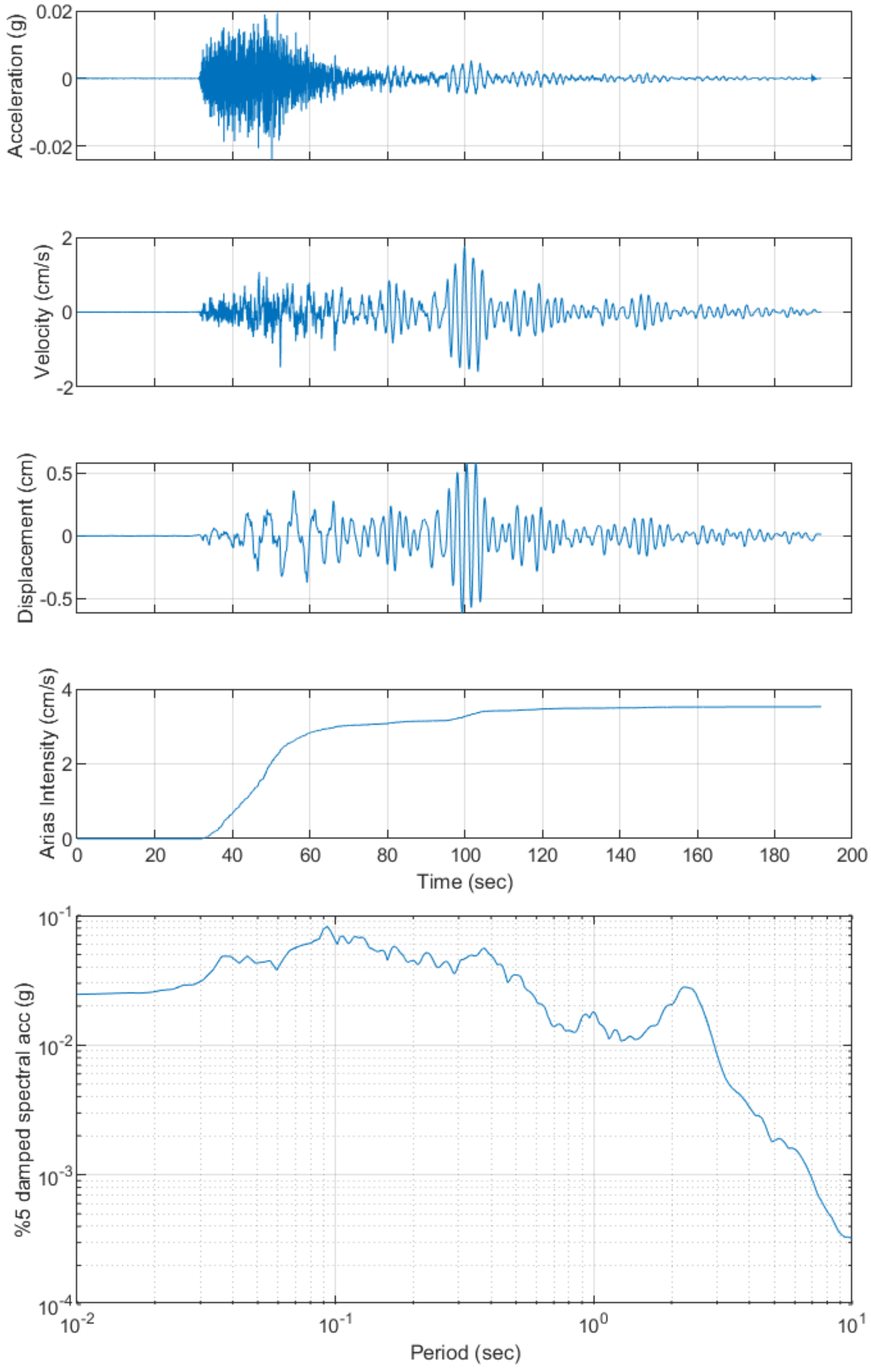

CE54388_GrndCenter, 2020MAY15, 270deg

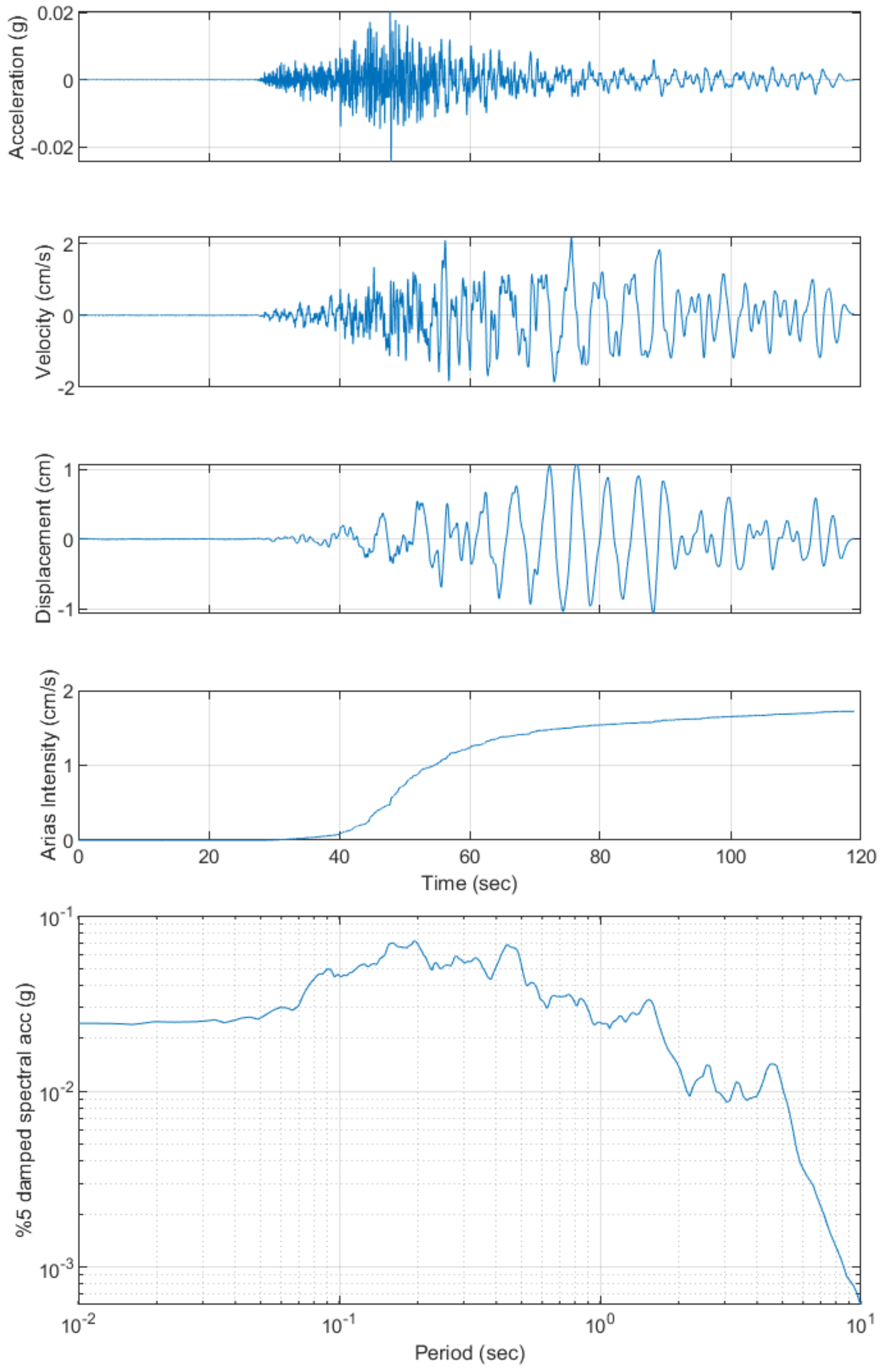

CE54388_GrndCenter, 2020MAY15, 360deg

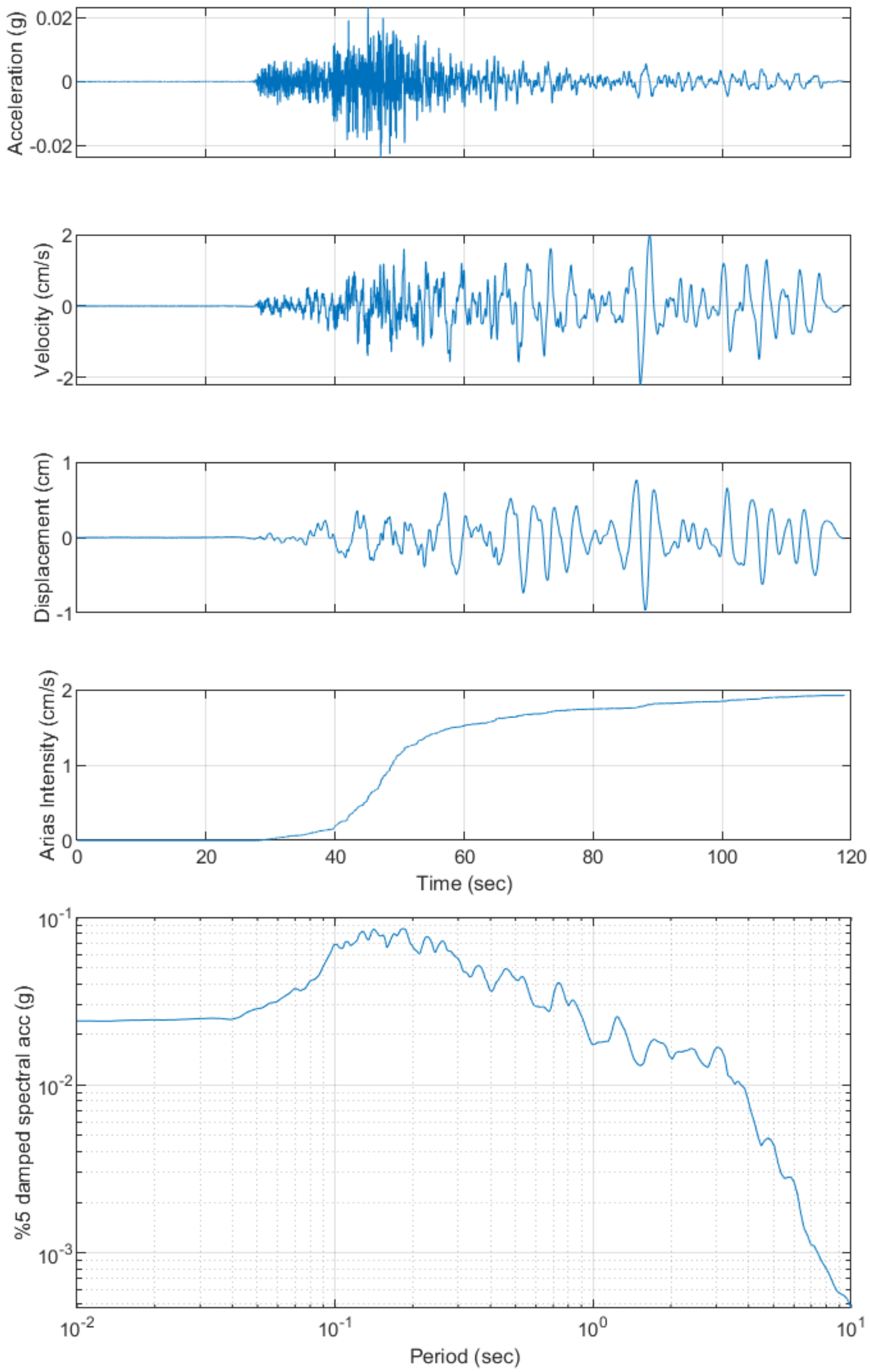

CE54388$_G$rndCenter, 2020MAY15, UP

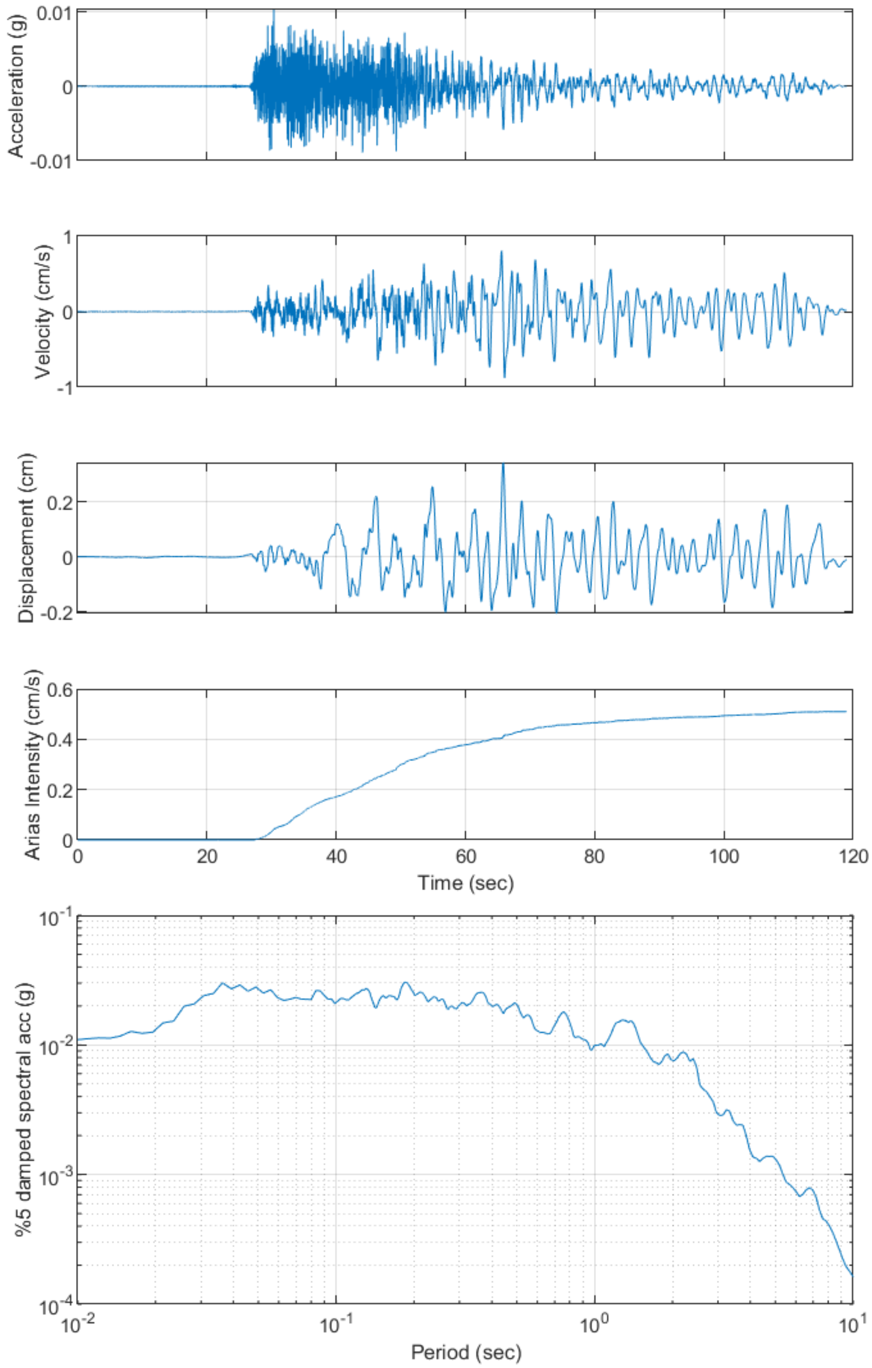

NCMLI, 2020MAY15, HNE

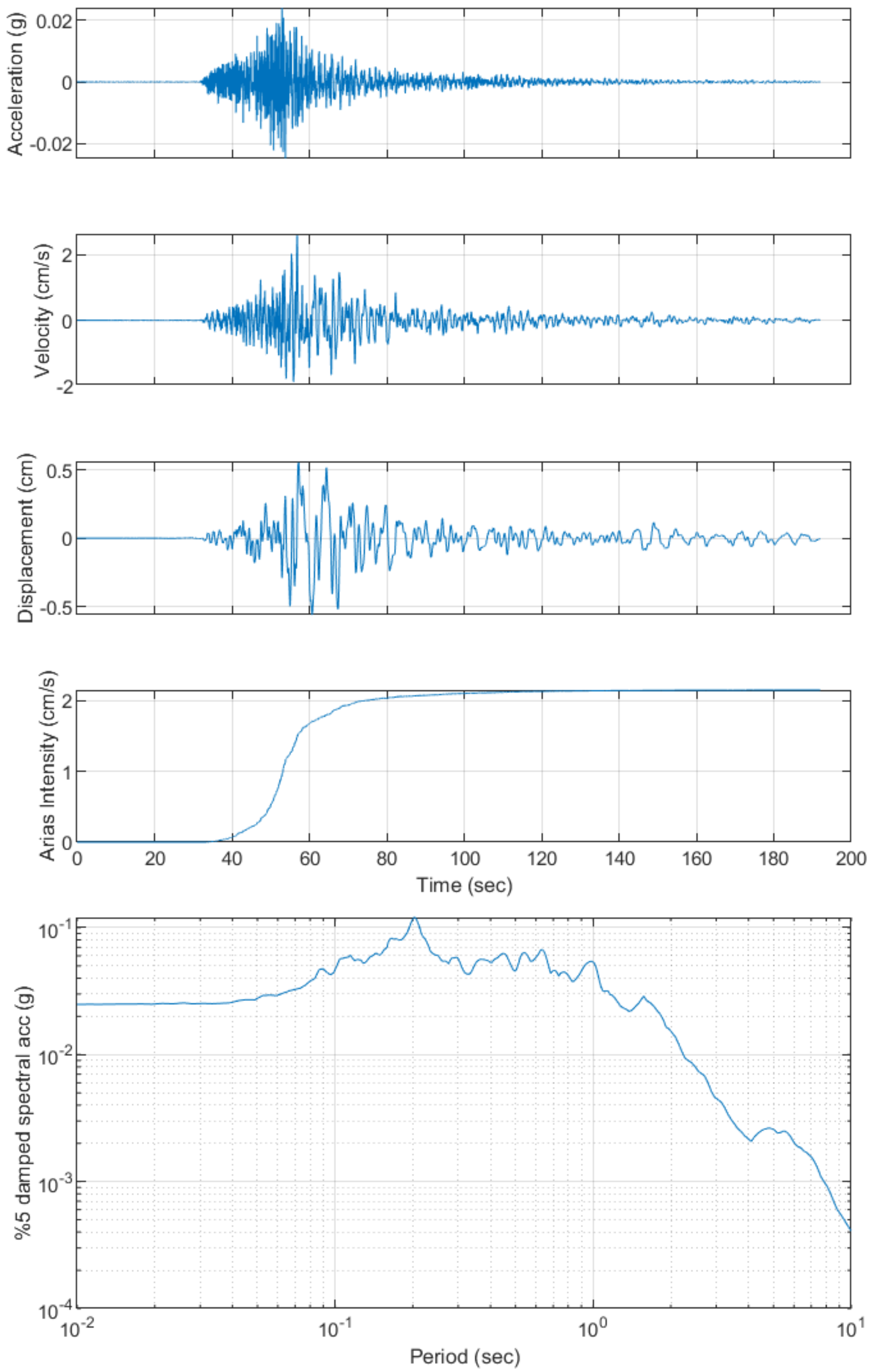

NCMLI, 2020MAY15, HNN

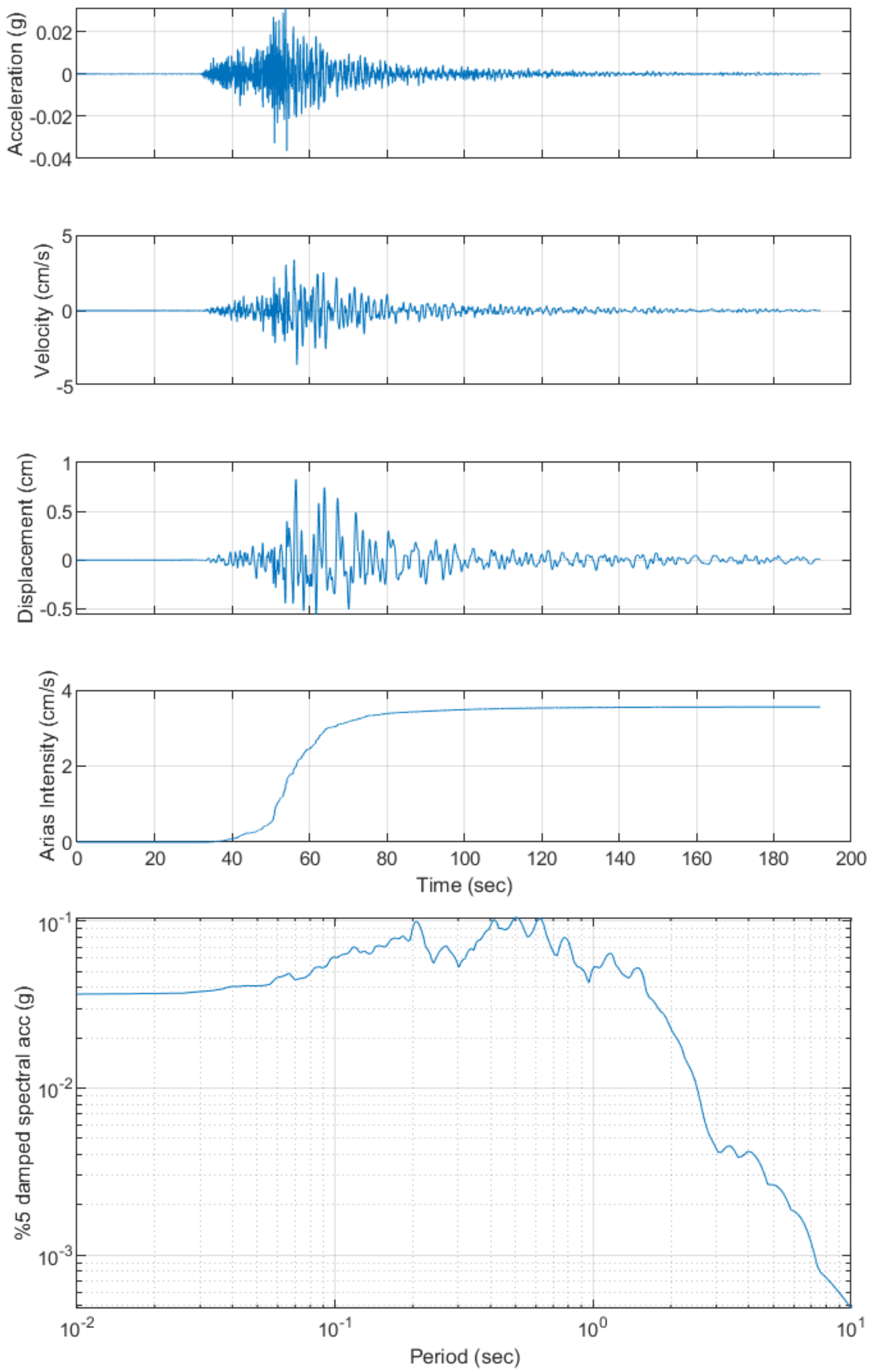

NCMLI, 2020MAY15, HNZ

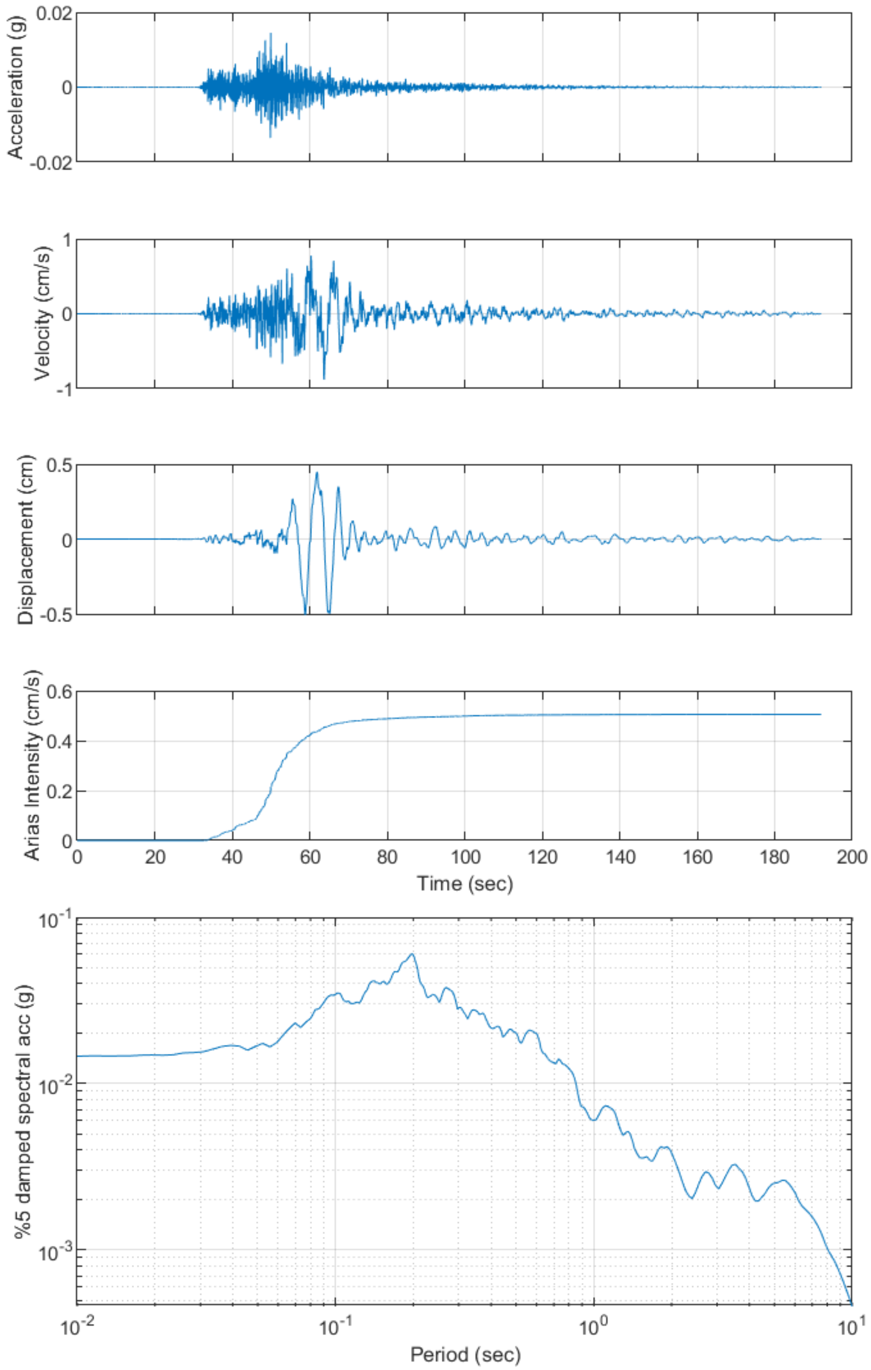

CE65654, 2020MAY15, 90deg

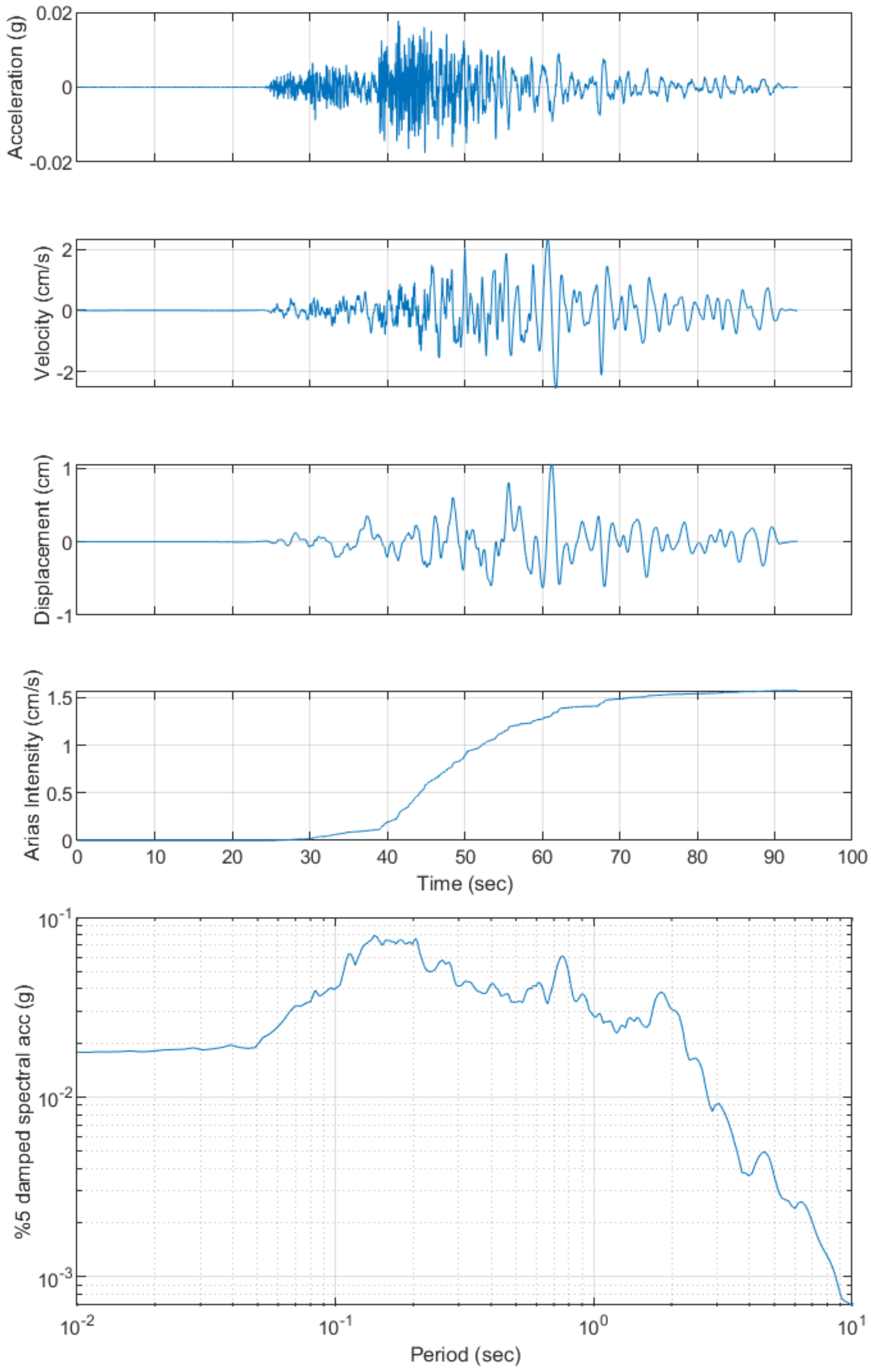

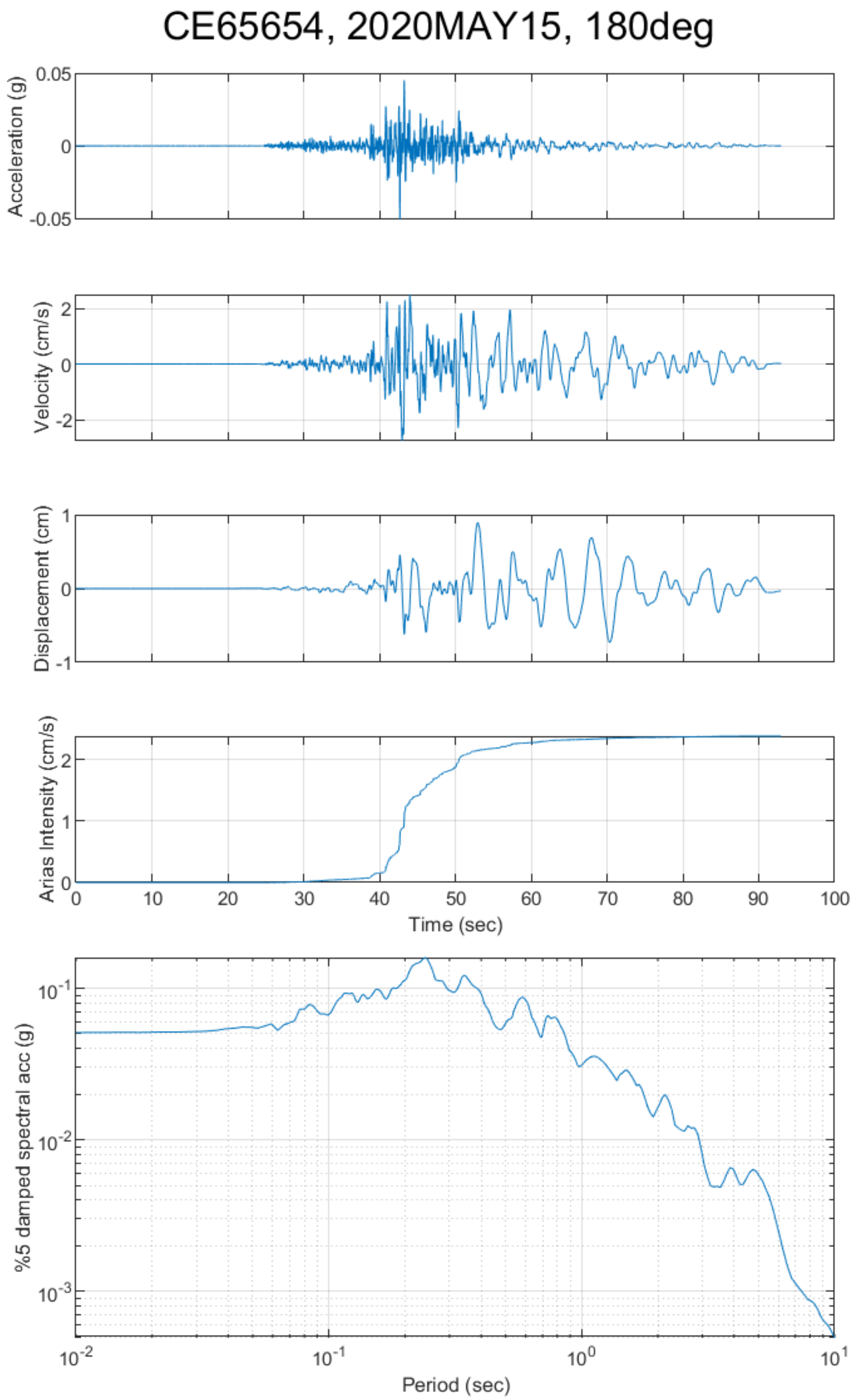

CE65654, 2020MAY15, 180deg
Acceleration (g)
0.05
0
-0.05
Velocity (cm/s)
2
0
-2
Displacement (cm)
1
0
-1
Arias Intensity (cm/s)
2
1
0
0
10
20
30
40
50
60
70
80
90
100
Time (sec)
%5 damped spectral acc (g)
10^{-1}
10^{-2}
10^{-3}
10^{-2}
10^{-1}
10^{0}
10^{1}
Period (sec)

CE65654, 2020MAY15, UP

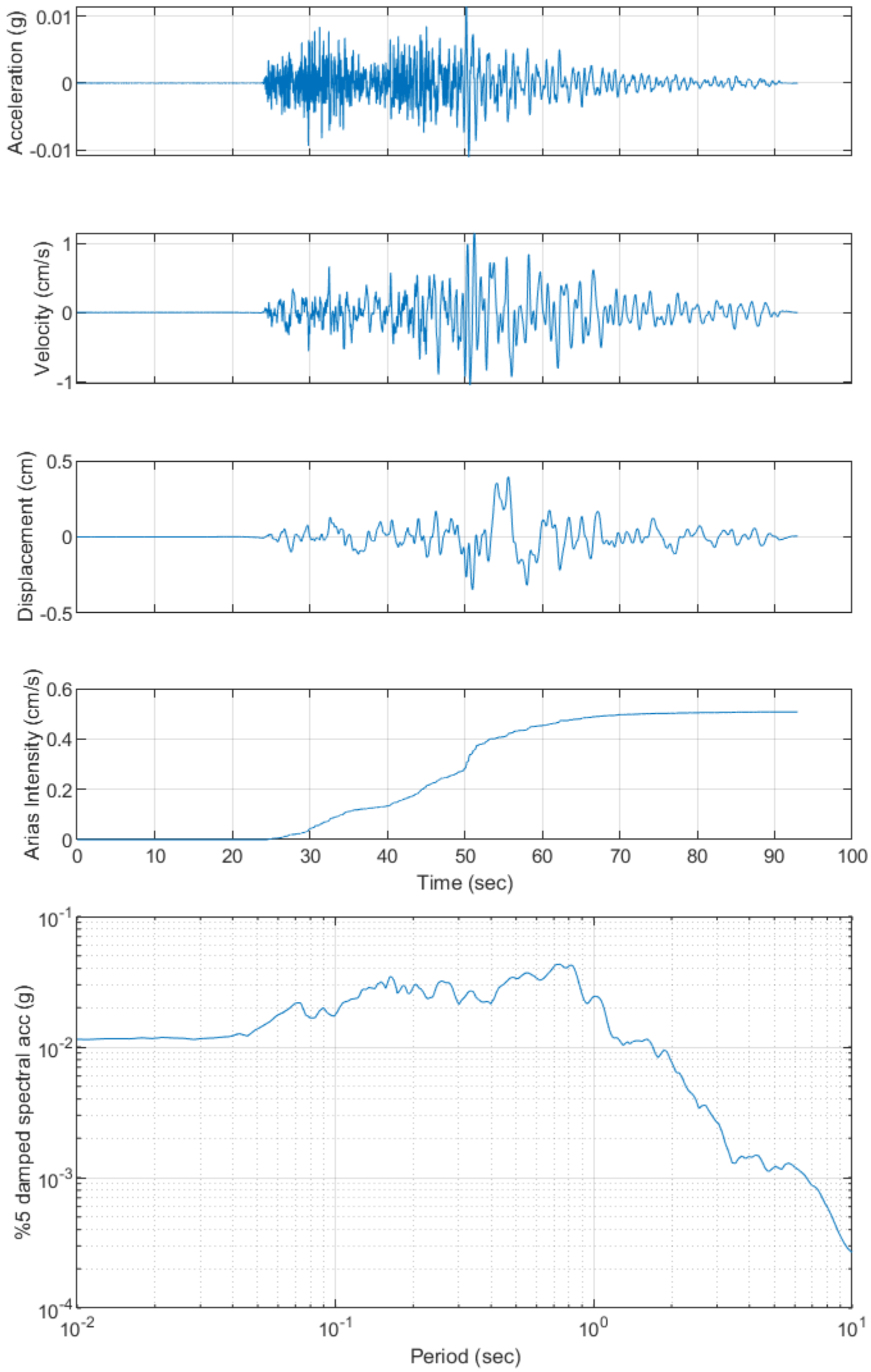

Appendix B:
Laboratory Index Test Results

Summary of Samples

Sample Name	Depth	Coordinates	Site	Description	W (%)	USCS	AASTHO	Soil Classification	Notes	Date
Boil #1	3 to 9 Inches	38.11204, -117.93291	GEER Monte Cristo	Brownish	13.94	CL-ML	A-4	Clayey Silt	Low Swelling Potential with traces of Halloysite	6/9/2020
Boil #2	19 to 24 Inches	38.11204, -117.93291	GEER Monte Cristo	Medium-Dark Brown	21.97	CL-ML	A-4	Clayey Silt	Low Swelling Potential with traces of Halloysite	6/9/2020
Boil #3	2 to 8 Inches	38.11174, -117.93252	GEER Monte Cristo	Brownish, Pumping Soft Ground	10.4	ML	A-4	Silt	Low Swelling Potential with traces of Halloysite	6/9/2020
GSS1 #1	Surface	38.1116, -117.9349	GEER Monte Cristo	Light Brown	8.41	SM	A-4	Silty Sand	No Swelling Potential	6/9/2020
GSS1 #2	2.5 feet	38.1116, -117.9349	GEER Monte Cristo	Brownish	16.67	CL-ML	A-4	Silt	Very Low Swelling Potential with traces of Halloysite	6/9/2020
GSS1 #3	3.5 feet	38.1116, -117.9349	GEER Monte Cristo	Brownish	24.18	CL-ML	A-4	Clayey Silt	Low Swelling Potential with traces of Halloysite	6/9/2020
GSS1 #4	5 feet	38.1116, -117.9349	GEER Monte Cristo	Brownish	25	CL-ML	A-4	Clayey Silt	Low Swelling Potential with traces of Halloysite	6/9/2020

University of Nevada, Reno

Boil #1

University of Nevada, Reno

	Sieve #	Particle Size (mm)	Empty Sieve (g)	Sieve+soil (g)	Soil Retained (g)	Percent Retained	Cumulative Percent Retained	Percent Finer	Total Percent Finer
Sieve Analysis Test	4	4.75	503.5	503.5	0	0.00	0.00	100	100
	10	2	462	462	0	0.00	0.00	100	100
	20	0.85	428	428.5	0.5	0.85	0.85	99	100
	40	0.425	380.5	382.5	2	3.39	4.24	96	99
	60	0.25	317.5	322.5	5	8.47	12.71	87	98
	100	0.15	520.5	532	11.5	19.49	32.20	68	94
	200	0.075	341	380.5	39.5	66.95	99.15	1	81
Hydrometer Test		0.035						94	76
		0.0252						90	73
		0.0162						88	71
		0.01						79	64
		0.0072						74	60
		0.0061						70	57
		0.0053						68	55
		0.0012						47	38
		0.0005							27
		0.0001							10
		5E-05							5

Water Content %	13.934

Mass (g)	Coarse	59	0.19187
	Fine	248.5	0.80813
	Total	307.5	

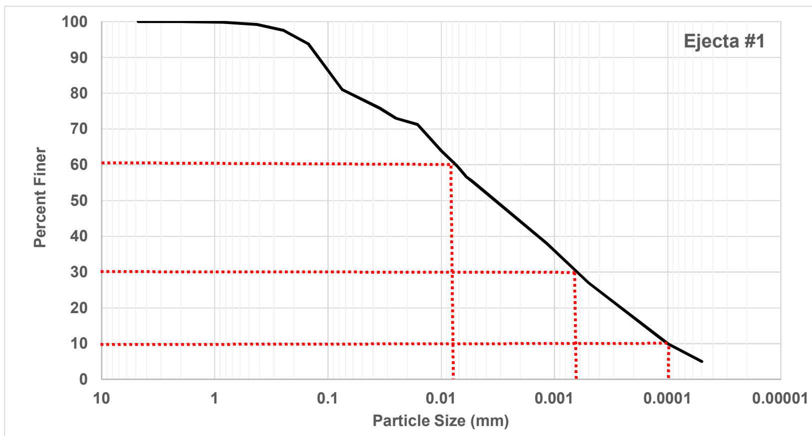

	mm
D_{10}	0.00009
D_{30}	0.0005
D_{60}	0.008
C_c	0.347
C_u	88.89

Gap Graded

LL %	24.53
PL %	20
PI	4.528
Adjusted PI	4.483
LI	-1.3472
A	0.0560

	USCS	AASHTO
Soil Type	CL-ML	A-4

Clayey Silt

Low Swelling Potential

Probably some traces of Halloysite

Boil #2

University of Nevada, Reno

	Sieve #	Particle Size (mm)	Empty Sieve (g)	Sieve+soil (g)	Soil Retained (g)	Percent Retained	Cumulative Percent Retained	Percent Finer	Total Percent Finer
Sieve Analysis Test	4	4.75	503.5	503.5	0	0.00	0.00	100	100
	10	2	462	462	0	0.00	0.00	100	100
	20	0.85	428	429	1	2.20	2.20	98	100
	40	0.425	380.5	383.5	3	6.59	8.79	91	98
	60	0.25	317.5	323.5	6	13.19	21.98	78	96
	100	0.15	520.5	531.5	11	24.18	46.15	54	91
	200	0.075	341	365	24	52.75	98.90	1	80
Hydrometer Test		0.0361						94	75
		0.0262						80	64
		0.0168						78	62
		0.01						72	57
		0.0073						67	53
		0.006						63	50
		0.0053						61	49
		0.0012						37	29
		0.0005							20
		0.0001							8
		5E-05							5

Water Content %	21.97

Mass (g)			
	Coarse	45.5	0.20313
	Fine	178.5	0.79688
	Total	224	

	mm
D_{10}	0.00013
D_{30}	0.0014
D_{60}	0.013
C_c	1.160
C_u	100.00

Well Graded

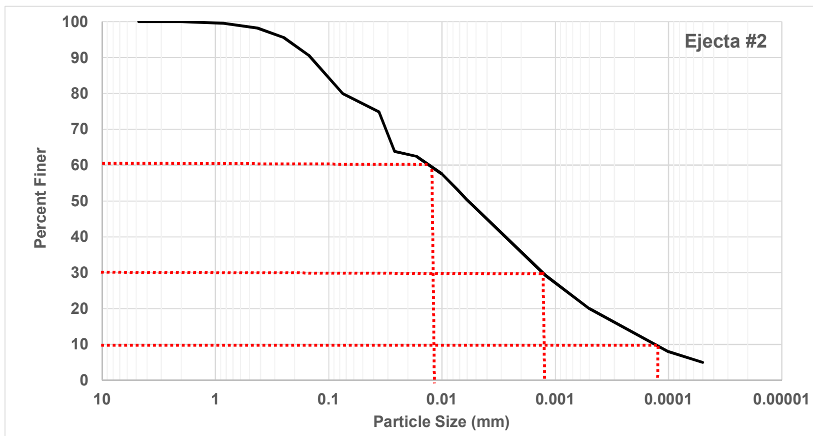

LL %	27.87
PL %	21
PI	6.869
Adjusted PI	6.731
LI	-0.0051
A	0.0942

	USCS	AASHTO
Soil Type	CL-ML	A-4

Clayey Silt

Low Swelling Potential

Probably some traces of Halloysite

Boil #3

	Sieve #	Particle Size (mm)	Empty Sieve (g)	Sieve+soil (g)	Soil Retained (g)	Percent Retained	Cumulative Percent Retained	Percent Finer	Total Percent Finer
Sieve Analysis Test	4	4.75	503.5	503.5	0	0.00	0.00	100	100
	10	2	462	462	0	0.00	0.00	100	100
	20	0.85	428	430	2	2.44	2.44	98	99
	40	0.425	380.5	386	5.5	6.71	9.15	91	97
	60	0.25	317.5	326	8.5	10.37	19.51	80	94
	100	0.15	520.5	538	17.5	21.34	40.85	59	88
	200	0.075	341	389.5	48.5	59.15	100.00	0	71
Hydrometer Test		0.0342						93	66
		0.025						88	62
		0.016						85	61
		0.0095						81	58
		0.0069						78	55
		0.0057						76	54
		0.005						73	52
		0.0012						47	33
		0.0005							22
		0.0001							8
		5E-05							4

Water Content %	10.40

Mass (g)	Coarse	82	0.29078
	Total Fine	200	0.70922
	Total	282	

	mm
D_{10}	0.00016
D_{30}	0.001
D_{60}	0.018
C_c	0.347
C_u	112.50

Gap Graded

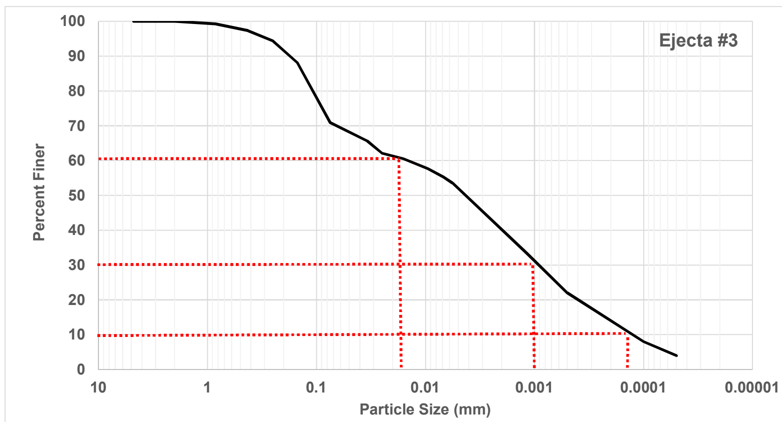

LL %	30.00
PL %	24
PI	6.000
Adjusted PI	5.820
LI	-1.3472
A	0.0820

	USCS	AASHTO
Soil Type	ML	A-4

Silt

Low Swelling Potential

Probably some traces of Halloysite (Clay)

GSS1 # 1

	Sieve #	Particle Size (mm)	Empty Sieve (g)	Sieve+soil (g)	Soil Retained (g)	Percent Retained	Cumulative Percent Retained	Percent Finer	Total Percent Finer
Sieve Analysis Test	4	4.75	503.5	503.5	0	0.00	0.00	100	100
	10	2	462	462	0	0.00	0.00	100	100
	20	0.85	428	428	0	0.00	0.00	100	100
	40	0.425	380.5	384.5	4	4.02	4.02	96	98
	60	0.25	317.5	334	16.5	16.58	20.60	79	89
	100	0.15	520.5	551	30.5	30.65	51.26	49	72
	200	0.075	341	389.5	48.5	48.74	100.00	0	46
Hydrometer Test		0.0378						75.25423729	35
		0.0278						66.77966102	31
		0.018						61.69491525	28
		0.0106						56.61016949	26
		0.0076						54.91525424	25
		0.0063						49.91525424	23
		0.0055						48.22033898	22
		0.0012						34.74576271	16
		0.0005							12
		0.0001							10
		5E-05							10

University of Nevada, Reno

Water Content %	8.41

Mass (g)	Coarse	99.5	0.5393
	Total Fine	85	0.4607
	Total	184.5	

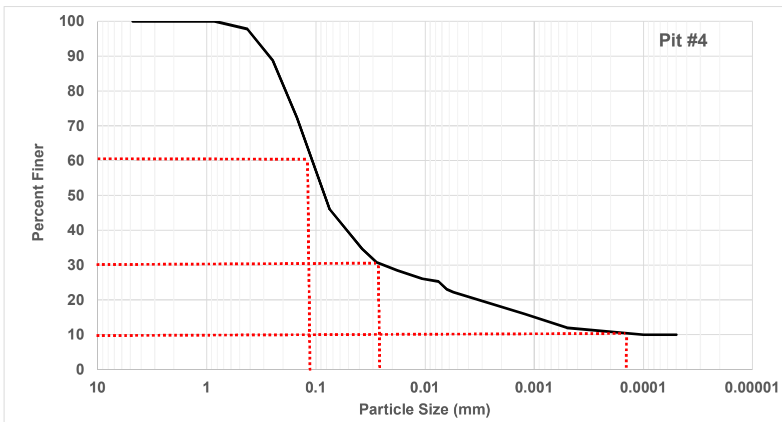

	mm
D_{10}	0.00017
D_{30}	0.028
D_{60}	0.11
C_c	41.925
C_u	647.06

Gap Graded

LL %	Does Not Apply
PL %	
PI	
Adjusted PI	
LI	
A	

	USCS	AASHTO
Soil Type	SM	A-4

Silty Sand

No Swelling Potential

GSS1 # 2

	Sieve #	Particle Size (mm)	Empty Sieve (g)	Sieve+soil (g)	Soil Retained (g)	Percent Retained	Cumulative Percent Retained	Percent Finer	Total Percent Finer
Sieve Analysis Test	4	4.75	503.5	503.5	0	0.00	0.00	100	100
	10	2	462	462	0	0.00	0.00	100	100
	20	0.85	428	430.5	2.5	3.50	3.50	97	99
	40	0.425	380.5	393.5	13	18.18	21.68	78	93
	60	0.25	317.5	335.5	18	25.17	46.85	53	84
	100	0.15	520.5	536.5	16	22.38	69.23	31	76
	200	0.075	341	363	22	30.77	100.00	0	66
Hydrometer Test		0.0358						90	59
		0.026						84.64285714	56
		0.0167						80.17857143	53
		0.0099						76.60714286	50
		0.0072						71.07142857	47
		0.0059						68.66071429	45
		0.0052						66.875	44
		0.0012						43.75	29
		0.0005							20
		0.0001							8
		5E-05							3

University of Nevada, Reno

Water Content %	16.67

Mass (g)	Coarse	71.5	0.34293
	Total Fine	137	0.65707
	Total	208.5	

	mm
D_{10}	0.00015
D_{30}	0.00016
D_{60}	0.025
C_c	0.007
C_u	166.67

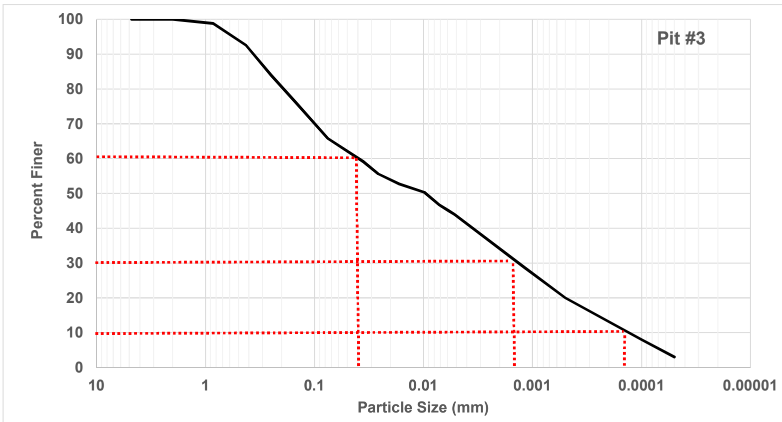

Gap Graded

LL %	26.21
PL %	24
PI	2.214
Adjusted PI	2.059
LI	-3.5622
A	0.0135

	USCS	AASHTO
Soil Type	ML	A-4

Silt

Very Low Swelling Potential

GSS1 # 3

	Sieve #	Particle Size (mm)	Empty Sieve (g)	Sieve+soil (g)	Soil Retained (g)	Percent Retained	Cumulative Percent Retained	Percent Finer	Total Percent Finer
Sieve Analysis Test	4	4.75	503.5	503.5	0	0.00	0.00	100	100
	10	2	462	462	0	0.00	0.00	100	100
	20	0.85	428	429	1	3.77	3.77	96	99
	40	0.425	380.5	382	1.5	5.66	9.43	91	98
	60	0.25	317.5	320	2.5	9.43	18.87	81	97
	100	0.15	520.5	525	4.5	16.98	35.85	64	94
	200	0.075	341	358	17	64.15	100.00	0	83
Hydrometer Test		0.0366						91	76
		0.0263						88	73
		0.0168						86	72
		0.0101						78	65
		0.0072						76	64
		0.0059						73	61
		0.0052						71	59
		0.0012						46	39
		0.0005							27
		0.0001							10
		5E-05							4

University of Nevada, Reno

Water Content %	24.18

Mass (g)			
	Coarse	26.5	0.16511
	Fine	134	0.83489
	Total	160.5	

	mm
D_{10}	0.0001
D_{30}	0.00055
D_{60}	0.006
C_c	0.504
C_u	60.00

Gap Graded

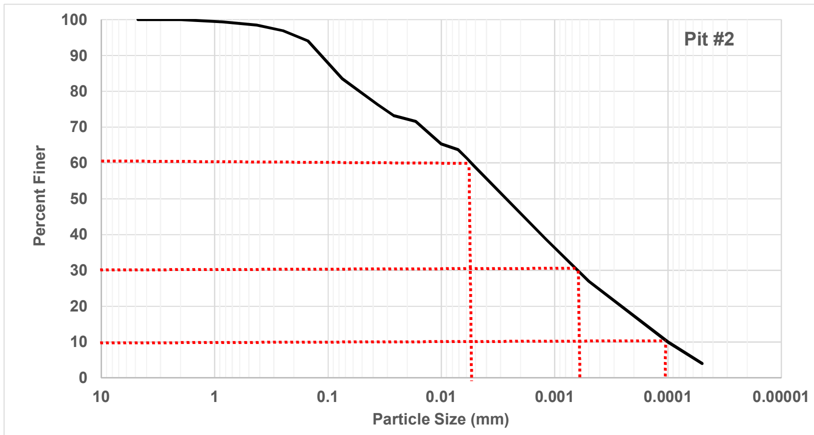

LL %	27.84
PL %	23.8
PI	4.035
Adjusted PI	3.954
LI	0.09504
A	0.0330

	USCS	AASHTO
Soil Type	CL-ML	A-4

Clayey Silt

Low Swelling Potential

Probably some traces of Halloysite (Clay)

GSS1 # 4

University of Nevada, Reno

	Sieve #	Particle Size (mm)	Empty Sieve (g)	Sieve+soil (g)	Soil Retained (g)	Percent Retained	Cumulative Percent Retained	Percent Finer	Total Percent Finer
Sieve Analysis Test	4	4.75	503.5	503.5	0	0.00	0.00	100	100
	10	2	462	462	0	0.00	0.00	100	100
	20	0.85	428	429	1	3.13	3.13	97	99
	40	0.425	380.5	382.5	2	6.25	9.38	91	98
	60	0.25	317.5	320.5	3	9.38	18.75	81	96
	100	0.15	520.5	526.5	6	18.75	37.50	63	92
	200	0.075	341	361	20	62.50	100.00	0	79
Hydrometer Test		0.0366						87	69
		0.0262						85	68
		0.0168						82	65
		0.01						75	60
		0.0072						72	57
		0.006						68	54
		0.0052						66	52
		0.0012						42	34
		0.0005							22
		0.0001							8
		5E-05							4

Water Content %	25.00

Mass (g)	Coarse	32	0.20645
	Total Fine	123	0.79355
	Total	155	

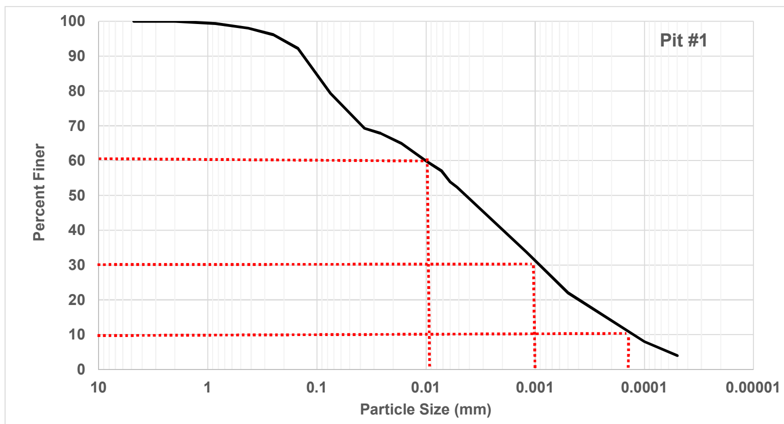

	mm
D_{10}	0.00016
D_{30}	0.001
D_{60}	0.01
C_c	0.625
C_u	62.50

Gap Graded

LL %	28.21
PL %	19.38
PI	8.825
Adjusted PI	8.649
LI	0.64981
A	0.0686

	USCS	AASHTO
Soil Type	CL-ML	A-4

Clayey Silt

Low Swelling Potential

Probably some traces of Halloysite (Clay)